

Aus dem Deutschen Krebsforschungszentrum Heidelberg
(Vorstand: Prof. Dr. Michael Baumann, Prof. Dr. Josef Puchta)
Abteilung X-Ray Imaging and CT
(Abteilungsleiter: Prof. Dr. Marc Kachelrieß)

Context–Sensitive Imaging for Single, Dual and Multi Energy Computed Tomography

Inauguraldissertation
zur Erlangung des Doctor scientiarum humanarum (Dr. sc. hum.)
an der
Medizinischen Fakultät Heidelberg
der
Ruprechts–Karls–Universität

vorgelegt von

Sabrina Dorn

aus Nürnberg

2019

Dekan: Prof. Dr. med. Andreas Draguhn
Doktorvater: Prof. Dr. Marc Kachelrieß

*The possibilities are
limited only by our imagination
and determination, and
not by the physics.*
Dr. Michael Duke

Contents

List of Figures	ix
List of Tables	xi
List of Acronyms	xii
1 Introduction	1
2 Fundamentals	7
2.1 Basics of X-Ray Physics	7
2.1.1 X-Ray Interactions with Matter	7
2.1.2 Lambert-Beer Law of Attenuation	11
2.2 CT Image Reconstruction	13
2.3 Basic Principles of Dual Energy CT	18
2.3.1 Material Decomposition	19
2.3.2 Material Mixtures: Volume and Mass Conservation	20
2.4 Clinical Dual Energy CT and its Applications	21
2.4.1 Sequential Dual Energy	23
2.4.2 Split Filter Dual Energy	23
2.4.3 Fast kV Switching Dual Energy	24
2.4.4 Dual Layer Detector Dual Energy	25
2.4.5 Dual Source Dual Energy	26
2.4.6 Photon-Counting Detector Dual and Multi Energy	28
3 Materials and Methods	31
3.1 Anatomical Prior Information	31
3.2 Context-Sensitive CT Image Formation	33
3.2.1 Tissue-Related Weights	33
3.2.2 Context-Sensitive Resolution	34
3.2.3 Context-Sensitive Image Display	35
3.3 Context-Sensitive Dual Energy	38
3.3.1 Liver Virtual Non-Contrast (LiverVNC)	38
3.3.2 Organ-Specific DE Evaluation and Analysis	42
3.3.3 Patient-Specific Parameter Calibration	42
3.4 Quantitative Pseudo Multi Material Decomposition	45

3.4.1	Material Decomposition in Image Domain	45
3.4.2	Prior Image-based Multi Material Decomposition	46
3.4.3	Organ-Adaptive Multi Material Decomposition	48
4	Results	51
4.1	Context-Sensitive CT Image Formation	51
4.1.1	Context-Sensitive Resolution	52
4.1.2	Context-Sensitive Image Display	61
4.2	Context-Sensitive Dual Energy	67
4.2.1	Organ-Specific DE Evaluation and Analysis	67
4.2.2	Iodine Quantification Accuracy Study	69
4.2.3	Patient-Specific RelCM Calibration	74
4.3	Quantitative Pseudo Multi Material Decomposition	77
4.3.1	Simulation-Based and Patient-Specific Basis Material Calibration	78
4.3.2	Material Decomposition Results	82
4.3.3	Pie Charts and Material Scores	85
5	Discussion	87
5.1	Anatomical Prior Information	88
5.2	Context-Sensitive CT Image Formation	89
5.3	Context-Sensitive Dual Energy	90
5.4	Quantitative Pseudo Multi Material Decomposition	91
5.5	Outlook	93
6	Summary	95
7	Zusammenfassung	97
	Bibliography	99
A	Additional Results	113
B	Publications	115
C	Curriculum Vitae	119
D	Acknowledgements	121

List of Figures

2.1	Mass attenuation coefficient	8
2.2	Linear attenuation coefficient	9
2.3	Linear attenuation coefficient of iodine	9
2.4	Linear attenuation coefficient of water	10
2.5	HU scale	13
2.6	Parallel beam geometry	14
2.7	Kernel apodization	16
2.8	System setup and geometry of a clinical CT	16
2.9	DECT technologies	22
2.10	Basic principles of Siemens DE applications	27
2.11	CounT acquisition modes	28
3.1	Sliding thin slab (STS) mean intensity projection	37
3.2	Syngo.CT dual energy applications	39
3.3	Coordinate transform of the Liver VNC application	39
3.4	Screenshot of the organ-specific initialization in the <i>LiverVNC</i> applications	40
3.5	Two, three or multi material decomposition in image domain	47
3.6	Overlapping Triangles	50
4.1	Tissue-related weights	52
4.2	Context-sensitive resolution	53
4.3	Comparison of basis images and corresponding context-sensitive image . .	54
4.4	Overview of the influence of different transition widths (Patient I)	55
4.5	Number of Kernels	56
4.6	Transition zone width (thorax Patient 7)	58
4.7	Transition Zone width (abdomen Patient 7)	59
4.8	Transition Zone Profile	59
4.9	Organ-adaptive selection of the transition widths	60
4.10	Context-sensitive window	62
4.11	Benefit of the context-sensitive windowing	64
4.12	Influence of the blending width	65
4.13	Organ-adaptive sliding thin slab (STS)	66
4.14	Comparison of a conventional CT image and a context-sensitive CT image	66
4.15	Liver iodine quantification	67
4.16	Context-sensitive DECT evaluation	68

4.17	Anthropomorphic phantoms	69
4.18	Phantom extension rings	69
4.19	Arrangement of seven vials containing different iodine concentrations . . .	70
4.20	Iodine quantification accuracy – Liver phantom 80/140 kV+Sn	71
4.21	Iodine quantification accuracy – Thorax phantom 80/140 kV+Sn	72
4.22	Qualitative comparison of iodine overlays	74
4.23	ROIs for iodine quantification	74
4.25	Basis material calibration for the decomposition of the thorax phantom .	79
4.26	Evaluation of simulation-based or patient-specific calibrations I	80
4.27	Evaluation of simulation-based or patient-specific calibrations II	83
4.28	Volume fraction material images of patient data	83
4.29	Quantitative and qualitative evaluation of PMMD	84
4.30	Comparison of bone fraction using different basis material triplets	85
4.31	Pie chart option I	86
4.32	Pie chart option II	86
A.1	Iodine quantification accuracy – Liver phantom 100/140 kV+Sn	113
A.2	Iodine quantification accuracy – Thorax phantom 100/140 kV+Sn	114

List of Tables

3.1	Typical window level settings for different anatomical regions	36
3.2	Calibration parameters for different organs (<i>LiverVNC</i> application) . . .	41
3.3	Default RelCM for different scanners and tube voltage combinations. . . .	44
3.4	Triplet material library of the pseudo multi material decomposition	49
4.1	Exemplary context-sensitive window level setting configurations	63
4.2	Patient-specific calibrations of the relative iodine contrast ratio	73
4.3	Iodine quantification accuracy using patient-specific calibrations	73
4.4	Evaluation of the mean iodine concentration	76
4.5	Statistical evaluation of the patient-specific calibration on patient data . .	76
4.6	Volume fractions/relative error within three ROIs containing one material	80
4.7	Volume fractions/relative error within six ROIs containing material mixtures	81
4.8	Volume fraction accuracy for water and iodine fraction	82

List of Acronyms

1D	one-dimensional
2D	two-dimensional
3D	three-dimensional
CT	computed tomography
SECT	single energy computed tomography
DECT	dual energy computed tomography
MECT	multi energy computed tomography
DE	dual energy
HU	Hounsfield Unit
C	center
W	width
FBP	filtered backprojection
FOM	field of measurement
ROI	region of interest
ROIs	regions of interest
VNC	virtual non-contrast
VUE	virtual unenhanced
CS	context-sensitive
CSR	context-sensitive resolution
CSD	context-sensitive display
CSDE	context-sensitive dual energy evaluation
STS	sliding thin slab
MeanIP	mean intensity projection
MinIP	minimum intensity projection
MIP	maximum intensity projection
MPR	multi planar reformation
CNN	convolutional neural network
2MD	two material decomposition
3MD	three material decomposition
MMD	multi material decomposition

CM	contrast media
CaHA	calcium hydroxyapatite

CHAPTER 1

Introduction

Since the advent of computed tomography (Hounsfield, 1973, 1976, 1980; Cormack, 1963, 1964), CT has revolutionized the field of medical imaging and has become one of the most important diagnostic tools. It is therefore irreplaceable in clinical practice. The non-invasive imaging modality uses x-ray projections that are acquired from multiple viewing angles to compute cross-sectional images of the spatial distribution of the attenuation coefficient of the examined patient (Cierniak, 2011). In 1971, with the invention of the first CT scanner, true “pictures” of the internal organs could be acquired for the first time in a relatively short amount of time. With the introduction of water-soluble iodinated contrast agents in 1976 (Davis et al., 1976), more variations in tissue contrast could be achieved. The advance of CT was so extraordinary that the Nobel Prize in Physiology or Medicine 1979 was awarded jointly to Allan M. Cormack and Godfrey N. Hounsfield “for the development of computer assisted tomography”.

Nowadays, CT devices are installed in almost every hospital and provide a fast and reliable modality for a multitude of diagnostic questions. Many therapeutic decisions are based on CT diagnoses in multiple medical disciplines. There are a multitude of varying indications for a CT scan including examinations, for instance, both in gastrointestinal and trauma imaging or oncology. The Federal Office in Radiation Protection reported a decrease of the average radiation dose of CT examinations by 16% in recent years (Scheegerer et al., 2017). Although examinations associated with a higher radiation dose are carried out more frequently, the average radiation dose per examination could nevertheless be reduced from 7 to 5.9 mSv. In particular, this could be achieved through the use of modern CT techniques (Scheegerer et al., 2017), for instance shorter scan times, tube voltage modulation and iterative image reconstruction.

The gray scales in the CT images represent attenuation values in relation to the one of water and are expressed as so-called Hounsfield units (HU). Water is assigned a CT value of 0 HU and air a CT value of -1000 HU across all energies. The CT values of any composition of different materials are then scaled relative to the CT value of water and air. CT is a quantitative imaging modality opposed to other imaging modalities, e.g. magnetic resonance imaging (MRI) (Kachelrieß, 2006). Since the range

of possible CT values is only restricted by the image quantization and typically ranges between -1000 HU and 3000 HU using 12 bit memory, CT images can be manipulated by changing the range of viewable CT values via windowing to emphasize certain contrast differences in order to improve the diagnostic value.

However, depending on the mass density, materials with different elemental compositions can be represented by identical pixel values in a CT image, rendering the differentiation of materials challenging (McCollough et al., 2015). Hounsfield (1973) and Alvarez and Macovski (1976) discovered that an additional spectral measurement of the attenuation coefficient might enable the discrimination of two materials. There are two main physical mechanisms dominating the attenuation of biological materials in the clinically relevant energy range for 20 to 150 keV: the photoelectric effect, which is dominated by the atomic number, and the Compton scatter, which depends on the irradiated beam energy. Both effects will be described in more detail later on in Section 2.1. Hence, dual energy CT (DECT) allows the discrimination between two materials with high atomic numbers, e.g. iodine, calcium or gadolinium, or in clinical practice two basis materials, e.g. bone and water, if no K-edge is present in the relevant energy range.

Due to the technical limitations of first-generation CT scanners, it had not been possible to acquire DECT data in sufficiently short scan times and with accurate spatial and temporal coherence. In 1987, the first commercial medical CT system with the ability to acquire DECT data was introduced (Krauss et al., 2015). During acquisition, the tube voltage settings were switched between the lowest and the highest possible tube voltage to measure interleaved projections during one rotation (Vetter et al., 1986). The CT system has been used to evaluate the vertebral bone mineral density using a two material decomposition (Kalender et al., 1987). Due to the availability of competitive technologies like DE x-ray absorptiometry and the high radiation dose penalty of first days' DECT, the technique was discontinued. Nevertheless, the remarkable success of the technical realizations of a dual source CT scanner in 2005 has enabled the possibility of commercially available DECT (Flohr et al., 2006; Achenbach et al., 2006).

In recent years, dual energy has become of high interest in CT. So far, there are dual layer detectors, fast kilovoltage (kV) switching or photon-counting detectors that are able to acquire DECT data. An overview of these technologies will be given in Section 2.4. By exploiting the energy dependency of the linear attenuation coefficient of biological tissue, one can now make a multitude of statements about the tissue type and material composition. By means of DECT, it is possible to visualize the spatial distribution of iodinated contrast agent, visualize and quantify the local iodine uptake in the human body or artificially remove the iodine content from the image in order to provide virtual unenhanced images. A virtual unenhanced image intends to mimic a native scan which would have been acquired without the injection of any contrast medium. Furthermore, kidney stones can be detected and characterized into uric acid or calcium-oxalate stones. Iodinated tissue can be separated from bone or any perfusion defect in the lung or the myocardium can be visualized. Further applications are mentioned in Section 2.4.

Thus, attenuation-dependent or material-specific contrasts as well as functional parameters can be routinely measured within short scan times of a few seconds with a sub-millimeter spatial resolution and high temporal resolution. A CT volume typically

consists of a large number of slices, is distortion free, highly accurate regarding spatial and temporal resolution and reproducible at any time. In general, for CT image reconstruction, display and analysis there are a multitude of parameters for one acquired CT raw data set. The CT image quality is determined by the used reconstruction algorithm and corresponding parameters. For instance, the choice of an analytic or iterative reconstruction method, the associated kernel selection in the analytic reconstruction or the strength of the iterative reconstruction impacts the image characteristics. In particular, a smooth reconstruction kernel results in an image with low noise, poor spatial resolution but high soft tissue contrast. On the contrary, a sharp kernel reconstruction achieves a high spatial resolution but also leads to a high noise level.

Moreover, varying organ-dependent display settings are usually applied during CT image reading. The images are often reformatted either in axial, coronal, sagittal, oblique, curved or arbitrary planes. For the presentation of different anatomical structures, there are organ-specific window level settings, where each one favors the presentation of different anatomical regions. Therefore, every CT examination needs to be carefully reviewed in at least three distinct windows that are optimized for soft tissue, lung and bone because some injuries or pathologies may only be apparent in a specific window setting (Mandell et al., 2018). In particular, it is recommended to reconstruct the lung with a sharp kernel and view the organ in a wide window centered around -600 HU. While there are contrast differences between air and lung tissue of up to 700 HU within the lung, variations of 100 HU due to noise are negligible. The lung window is therefore superior for the diagnosis of lung diseases compared to a narrower soft tissue gray level window (Harris et al., 1993; Pomerantz et al., 2000). Furthermore, a sliding thin slab (STS) maximum intensity projection (MIP) is frequently applied to the lung visualization in order to detect lung nodules. Since the soft tissue contrast is limited to about 100 HU, a narrow window centered around the mean value of soft tissue is optimal for diagnosis. Moreover, reading liver images requires a low noise level. In order to minimize the remaining noise level in soft tissue, the images are usually displayed using thicker slabs (Napel et al., 1993; Ertl-Wagner et al., 2006), although thin slices would be preferable.

The mentioned DECT applications, e.g. decomposition into iodine maps and VNC images, kidney stone classifications, gout visualization etc., process the entire DECT data set and perform the DECT evaluation in an organ- or indication-specific manner. Therefore, the dual energy information only inside the considered organ can be evaluated to make a diagnosis. Outside the specific organ of interest, the DECT information is worthless. In clinical routine, the radiologists need to manually call each application in order to actuate a specific DE evaluation. Various applications have to be invoked sequentially, if the user wants to evaluate different body regions. Moreover, each DECT application only works for specific organs and only with a patient-specific calibration. Since the attenuation depends on the patient size due to beam hardening and scatter of the polychromatic x-ray beam, most applications suffer from ambiguities in the material decomposition resulting from erroneous calibrations of the algorithms. To find a diagnosis based on DECT data involves therefore several user interactions and requires the user to interpret multiple DECT evaluations.

Hence, a case-adapted CT examination is usually conducted for each medical question enabling a comprehensive diagnosis for the patient. In case of various diagnostic questions, many different CT volumes need to be read and interpreted. Therefore, the sensitivity for incidental findings is limited by the variety of possibilities during image formation and display as they are prone to being missed. As a consequence, reading CT images as well as preparing them for interdisciplinary case discussions and tumor boards are a tedious and time-consuming task. Having briefly outlined the state-of-the-art research as well as current drawbacks and limitations of nowadays conventional CT imaging during diagnosis, the objectives of this thesis shall now be defined. The main objective of this thesis is to examine the potential benefit of the incorporation of patient-specific anatomical priors, which are gained from an automatic multi-organ segmentation, to provide novel possibilities in the field of single, dual or even multi energy CT image formation, display and analysis and to implement a more sophisticated imaging paradigm for diagnosis. Therefore, an end-to-end pipeline starting from reconstruction to display and analysis of CT data will be presented to provide a proof of concept of an innovative CT image presentation.

First, the physical fundamentals, in particular the interaction of x-rays with matter, underlying single, dual or multi energy CT imaging are described. Moreover, Chapter 2 presents conventional image formation using analytic reconstruction and highlights the influence of the reconstruction kernel on the resulting image quality. In a next step, the chapter summarizes the principle of DECT and provides an overview of different technological strategies to acquire spectral CT data. The term spectral CT includes dual and multi energy CT. Following a short review of current automatic multi-organ segmentation approaches, the organ-adapted image formation providing the context-sensitive CT imaging is presented in Chapter 3.

As a starting point, the novel imaging concept combines the advantages of commonly used reconstructions and display methods. The display of one context-sensitive CT volume is favored by this novel paradigm. In order to improve the image impression, it is possible to interactively adjust varying organ-specific parameters in real time. Moreover for comparison purposes, it also enables the smooth transition back to conventional CT imaging. Furthermore, numerous DECT applications, e.g. iodine quantification, kidney stone classifications etc., are combined into one single analysis tool. The type of DECT evaluation as well as the parameters for these DECT applications are selected fully automatically based on the anatomical priors. The iodine quantification accuracy is examined regarding a default or patient-specific calibration that results from the prior anatomical knowledge in order to improve the decomposition accuracy. In addition to clinically relevant DECT applications, the DECT data are decomposed into their constituent material components using the proposed pseudo multi material decomposition consisting of multiple organ-adapted three material decompositions. By means of anatomical priors, the basis materials are selected automatically and adjusted to the organ of interest. The resulting volume fractions are converted to material scores and presented to the radiologists using alternative visualizations, i.e. pie charts, in order to support radiologists during diagnosis and treatment planning.

Chapter 4 shows the results for the proposed methods followed by a short discussion. The benefit of the segmentation–assisted CT image formation, display and analysis as well as the potential to significantly improve clinical routine is further discussed in Chapter 5. Finally, Chapter 6 concludes with a summary of the contributions of this thesis and shows how the discussed methods open up for interesting and challenging new research topics.

CHAPTER 2

Fundamentals

2.1 Basics of X-Ray Physics

A computed tomography (CT) system captures the attenuation of x-rays passing through an object for a variety of x-ray beams (Röntgen, 1895) and generates cross-sectional images of the body. The following chapter will provide the fundamental background of x-ray-based CT underlying this work.

2.1.1 X-Ray Interactions with Matter

The attenuation of monochromatic x-ray beams passing through an object is described by the Lambert–Beer law of attenuation. If N_0 depicts the total number of photons at a specific energy E_0 that hit an absorber with a specific attenuation coefficient μ and thickness d , overall N photons are transmitted through the absorber

$$N = N_0 \cdot e^{-\mu \cdot d}. \quad (2.1)$$

By measuring the number of photons N behind the absorber, the line integral $\mu \cdot d$ can be calculated, if the total number of photons N_0 is known from a reference measurement. The remaining $N - N_0$ photons are either absorbed or scattered in different directions. The exponential reduction in photon number relies on the fact that each photon is removed individually from the incident beam by a photon–matter interaction (Buzug, 2008). Within the clinically relevant energy range between 20 keV and 150 keV, mainly three physical effects are responsible for the interactions: photoelectric effect, Compton scattering and Rayleigh scattering (Krieger, 2009). Thus, the total linear attenuation coefficient can be expressed as an additive combination of the contributions of the photoelectric effect $\mu_{\text{Photo}}(E)$, Compton scattering $\mu_{\text{Compton}}(E)$ and Rayleigh scattering $\mu_{\text{Rayleigh}}(E)$

$$\mu_{\text{Total}}(E) = \mu_{\text{Photo}}(E) + \mu_{\text{Compton}}(E) + \mu_{\text{Rayleigh}}(E), \quad (2.2)$$

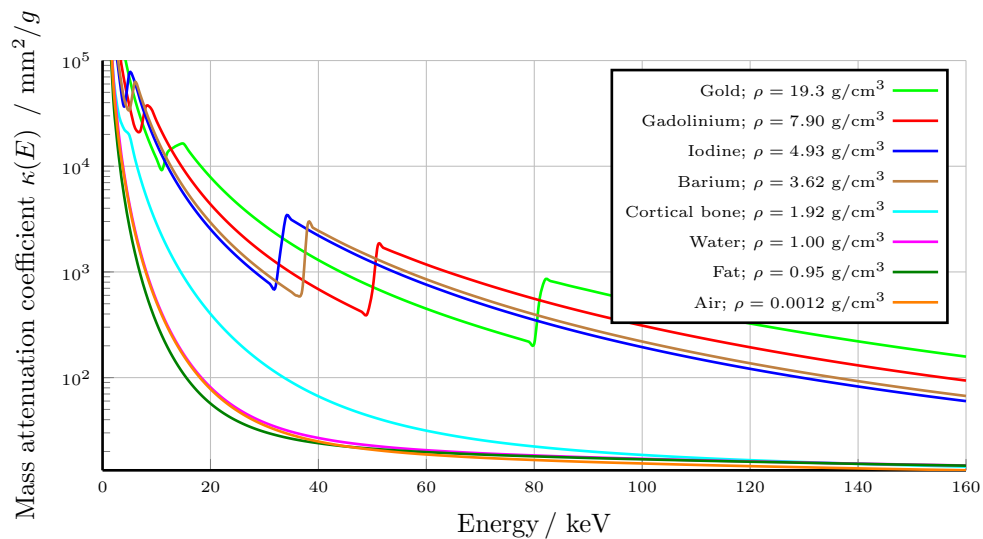


Figure 2.1: Mass attenuation coefficient $\kappa(E)$ for different materials. Gold, gadolinium, barium and iodine can be used as contrast media and show K-edges in the clinically relevant energy range. The latter four materials represent the major tissues in the human body. Since the mass attenuation coefficient largely differs between the shown materials, the mass attenuation coefficient is shown in a logarithmic scale. In addition, the mass density of the different materials are also listed in the legend.

which is measured in units of inverse millimeters [mm^{-1}]. It describes the attenuation behavior and depends on the energy E of the incident photon and on the atomic number Z of the absorber material (Evans and Evans, 1955). The contributing physical effects will be briefly described in the following paragraphs. By introducing the absorber density ρ , the mass attenuation coefficient is defined as $\kappa = \frac{\mu}{\rho}$ (Buzug, 2008). The linear and mass attenuation coefficient will be discussed in more detail in the following section. The energy-dependent mass attenuation coefficient of different materials is depicted in Figure 2.1. The corresponding linear attenuation coefficients are also illustrated in Figure 2.2.

Photoelectric Absorption

The photoelectric effect is the most important photon-matter interaction for low energy photons (Attix, 1987). The incident photon is completely absorbed and a photo-electron is released from one of the inner shells of the absorber's atoms. The photoelectric effect takes place preferably at K or L shells of the atoms. The absorption coefficient is approximately proportional to

$$\mu_{\text{Photo}}(E) \propto \rho \frac{Z^n}{AE^m}, \quad (2.3)$$

with A being the atomic mass, Z being the atomic number of the absorber material and E being the energy of the incident photon. The exponent n increases and m decreases with the amount of energy and is e.g. $n \approx 4$ and $m \approx 3$ at 100 keV (Knoll, 2010; Attix, 1987). The heavily energy-dependent interaction dominates for relatively low photon energies

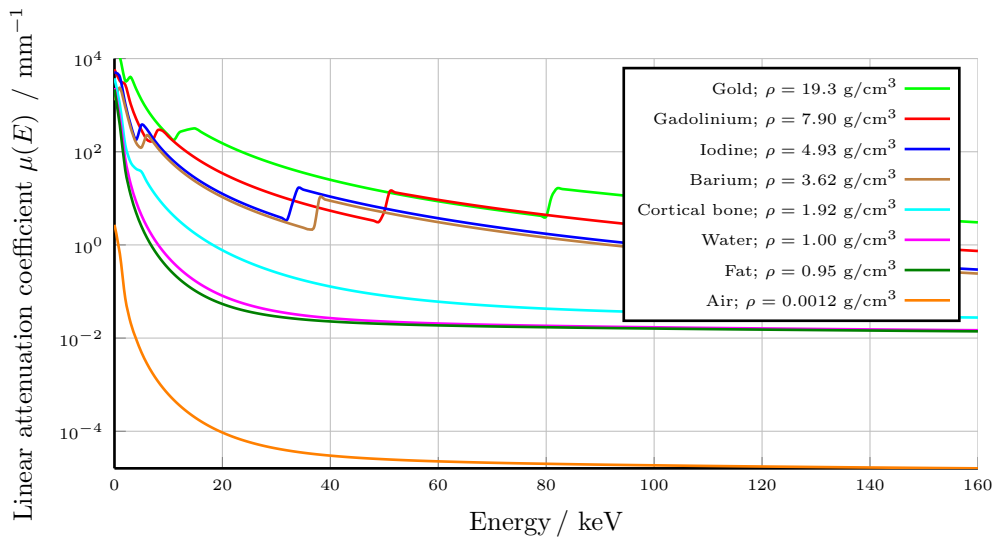


Figure 2.2: Linear attenuation coefficient $\mu(E)$, which is independent of the mass density ρ , for different materials. Gold, gadolinium, barium and iodine can be used as contrast media and show K-edges in the clinically relevant energy range. The latter four materials represent the major tissues in the human body. Since the mass attenuation coefficient largely differs between the shown materials, the mass attenuation coefficient is shown in a logarithmic scale. In addition, the mass density of the different materials are also listed in the legend.

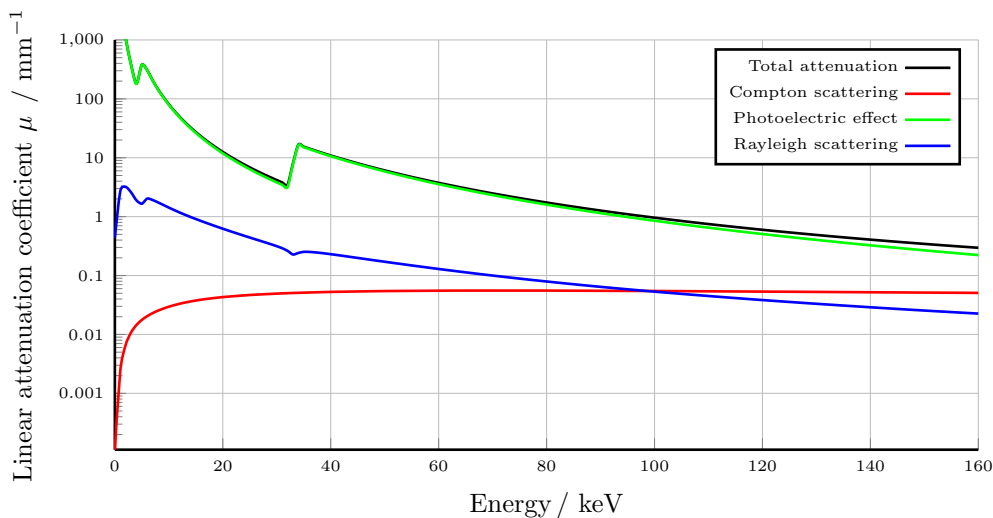


Figure 2.3: Linear attenuation coefficient $\mu(E)$ of iodine within the clinically relevant energy range between 20 and 150 keV. The total attenuation coefficient corresponds to the summation of the contributing physical effects. The photoelectric effects provides the dominating contribution.

and strongly depends on the atomic number of the absorber material. The contributions of the linear attenuation coefficient as well as the total attenuation coefficient of iodine is illustrated in Figure 2.3. In comparison to the linear attenuation coefficient of water (see Figure 2.4), iodine shows a significantly higher attenuation value. Towards high Z -numbers, the photoelectric effect becomes the dominating physical effect. Since the

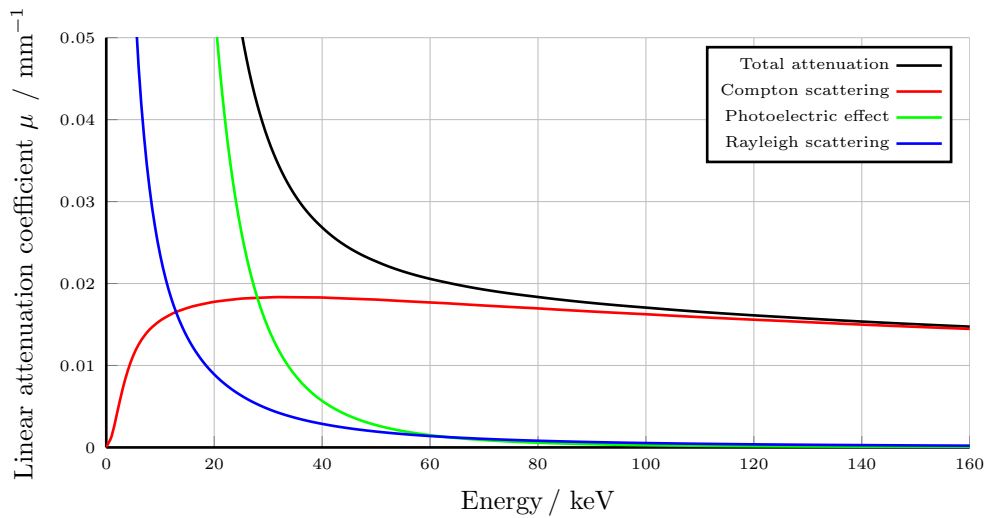


Figure 2.4: Linear attenuation coefficient $\mu(E)$ of water within the clinically relevant energy range between 20 and 150 keV. For small photon energies below 30 keV the photoelectric effect dominates the attenuation behavior while above 30 keV Compton scattering is predominant. The contribution of Rayleigh scattering is of minor importance.

photons are nearly immediately absorbed and deposit their total amount of energy in the patient, the photoelectric effect mainly contributes to the patients' dose.

Compton Scatter

In contrast to the photoelectric effect, an x-ray photon of energy E inelastically interacts with a quasi-free electron of the outermost shells of an atom of the absorbing material (Buzug, 2008). It transfers a fraction of its energy to the electron and creates a recoil electron and a scattered photon, which is deflected from its original flight direction. The energy loss is nearly immediately absorbed in the patient and contributes to patient dose. Compton scattering is an incoherent scattering process, where even backward scattering is possible. The highest probability of backward scattering occurs at low photon energies. The energy dependency of the different contributions of the attenuation coefficient of water is shown in Figure 2.4. By comparing the shape of the single contribution fractions, Compton scattering dominates for energies above 30 keV. In particular, within the clinically relevant energy range, the Compton effect is the dominant interaction process in water and water-equivalent soft tissue of the human body, i.e. in materials with low atomic numbers. The attenuation coefficient resulting from Compton scattering is approximately given by

$$\mu_{\text{Compton}}(E) \propto \rho \frac{Z}{AE^m}, \quad (2.4)$$

with $0 < m < 1$ (Krieger, 2009). Since the relationship between Z and A is almost constant for all materials, the material dependency is mostly related to the density of the material. As shown for both materials iodine and water in Figure 2.3 and Figure 2.4, the Compton scattering is insensitive to the photon energy. However, the resulting scattered photons carry a lower energy and can be further absorbed by the photoelectric effect.

Rayleigh Scattering

Additionally to Compton scattering, there is also another scattering event that may occur. The photon is elastically scattered by all bound electrons of the absorber atom. However, it retains its original energy and only the trajectory of the photon is slightly changed. Since the energy of the photon is conserved, there is no contribution to the actual patient dose. Above an energy of 10 keV, the attenuation coefficient decreases quadratically with the photon energy E and increases with the density of the absorber. The attenuation coefficient of the Rayleigh scattering is approximately proportional to

$$\mu_{\text{Rayleigh}}(E) \propto \rho \frac{Z^{1.5}}{E^2}. \quad (2.5)$$

The contribution of Rayleigh scattering is only relevant for materials with low atomic numbers, e.g. human tissue or water, below 20 keV and has therefore only a minor contribution to the overall attenuation coefficient μ . The maximum of the Rayleigh scattering migrates with higher atomic numbers towards higher photon energies (Krieger, 2009).

2.1.2 Lambert–Beer Law of Attenuation

After having described the photon–matter interactions, the definition of the Lambert–Beer law of attenuation in Equation (2.1) needs some further considerations. As illustrated in Figure 2.1 and 2.2 the attenuation coefficients of different tissues in the human body differ due to varying material constituents. As a consequence, the spatial distribution of the attenuation coefficient enables the modality of CT to be of diagnostic interest. It can be concluded that Equation (2.1) holds only true for ideal homogeneous objects at a monochromatic spectrum. If the irradiated object consists of more than one material, the attenuation coefficient follows a location–dependent distribution in space $\mu = \mu(\mathbf{r}, E)$, with $\mathbf{r} = (x, y, z)$ being the position. The product $\mu \cdot d$ is now described by the line integral $\int dl \mu(\mathbf{r}, E)$. The generalized Lambert–Beer law for a polychromatic incident photon spectrum $N_0(E)$ that is transmitted and attenuated when passing through a heterogeneous object is therefore given by

$$N(E) = N_0(E) \cdot e^{-\int dl \mu(\mathbf{r}, E)}. \quad (2.6)$$

The integration over all energies E yields the total number of transmitted photons

$$N = \int dE N_0(E) \cdot e^{-\int dl \mu(\mathbf{r}, E)}. \quad (2.7)$$

Instead of considering the photon spectrum $N_0(E)$ as being incident on the detector, one needs to account for the spectral efficiency and for the conversion factor introduced by the detector. The detector efficiency is given by $\eta(E) = 1 - e^{-\mu_{\text{Det}}(E) \cdot d_{\text{Det}}}$, where $\mu_{\text{Det}}(E)$ denotes the attenuation coefficient of the detector material and d_{Det} being the detector thickness. The conversion factor differs depending on the detector type and is denoted as detector sensitivity. For ideal energy integrating detectors $w(E) \propto EI(E)$ is the energy weighted intensity. For photon counting detectors $w(E) \propto I(E)$ corresponds

to the x-ray intensity. Overall, a realistic model of a scintillation detector is given by

$$w(E) \propto EI(E)\eta(E) \quad \text{subject to} \quad \int dE w(E) = 1, \quad (2.8)$$

where $w(E)$ is the detected spectrum. The detected signal in terms of intensity values, which indicates the attenuation process, yields

$$I = \int dE I_0(E) \cdot e^{-\int dl \mu(\mathbf{r}, E)}, \quad (2.9)$$

where $I_0(E) = EI(E)\eta(E)$ covers the detector efficiency and sensitivity. In CT, it is of specific interest to obtain the spatial distribution of the energy-dependent attenuation coefficient, i.e. the inversion of the integral operation, and therefore a log-transform is introduced. The raw data, known as projection values, are given by

$$q = -\ln \frac{I}{I_0}, \quad (2.10)$$

with $I_0 = \int dE I_0(E)$. The polychromatic projection values of the object $\mu(\mathbf{r}, E)$ are as follows

$$q = -\ln \int dE w(E) e^{-\int dl \mu(\mathbf{r}, E)}. \quad (2.11)$$

If $w(E)$ describes a monochromatic spectrum, i.e. $w(E) = \delta(E - E_0)$ the ideal measurement

$$p = \int dl \mu(\mathbf{r}, E_0) \quad (2.12)$$

is obtained.

In CT, attenuation profiles of an object are measured by acquiring x-ray projections from different viewing directions. For this purpose, the x-ray source and detector are rotated around the patient with high velocity. A polychromatic x-ray spectrum is targeted at the patient, where the maximum energy is determined by the tube voltage in kV. The distribution of $\mu(\mathbf{r})$ is then reconstructed from the set of measured attenuation profiles, the so-called raw data, to cross-sectional images. The basic principle of CT reconstruction will be discussed in Section 2.2.

In clinical CT, each voxel in the image is assigned a gray scale value, i.e. a CT value. Since the patient is mainly composed of water-equivalent materials, it has proven its worth to scale the reconstructed attenuation coefficient relative to the attenuation coefficient of water using the Hounsfield scale in units of HU for the CT value (Hounsfield, 1973; Brooks, 1977). The HU scale is shown in Figure 2.5. Considering the attenuation coefficient of a material μ and the attenuation coefficient of water $\mu_{\text{H}_2\text{O}}$, the CT value of that material is defined as

$$\text{CT value} = \frac{\mu - \mu_{\text{H}_2\text{O}}}{\mu_{\text{H}_2\text{O}}} \cdot 1000 \text{ HU} \quad (2.13)$$

By definition, water has a CT value of 0HU and air a CT value of -1000 HU. The CT values represent a quantitative measure of the densities of different materials and therefore CT is considered to be a quantitative imaging modality. However, it should

be noted that the attenuation coefficient of water depends on the energy of the x-ray spectrum on the one hand and on the calibration of the system on the other hand. Furthermore, different materials with similar densities may have overlapping CT values at certain energies and therefore cannot be distinguished in a single energy acquisition.

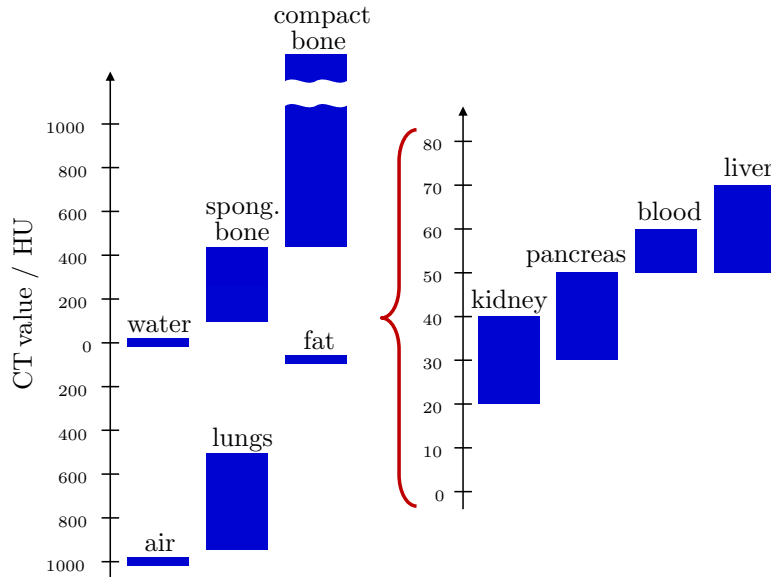


Figure 2.5: CT values are displayed in Hounsfield units. The values of the HU scale can be assigned to specific tissue classes and they provide a quantitative measure of the x-ray attenuation in human tissue.

2.2 CT Image Reconstruction

The projection value of an x-ray beam along the line L intersecting with an object f yields

$$q(L) = \int d\lambda f(\mathbf{s} + \lambda\Theta), \quad (2.14)$$

with the vector \mathbf{s} being the focus point of the x-ray source and Θ being the direction of the x-ray beam towards the detector element. According to Radon (1917), the distribution of a material within an image section can be reconstructed, if the set of line integrals along each ray passing through the same plane are known. The integration along the set of all possible lines in two dimensions (2D) is given by the Radon transform with the corresponding operator R . The integration along the set of all possible lines in three dimensions (3D) is called the x-ray transform. An operator X is introduced for the x-ray transform in 3D and is used in the following. It should be noted that the x-ray transform in 2D is equivalent to the Radon transform. Equation (2.14) can be reformulated to

$$q(L) = Xf(\mathbf{r}), \quad (2.15)$$

where $\mathbf{r} = (x, y, z)$ corresponds to an arbitrary point along the line L . The inversion of the above equation to $f(\mathbf{r}) = X^{-1}q(L)$ results in the reconstruction of the object

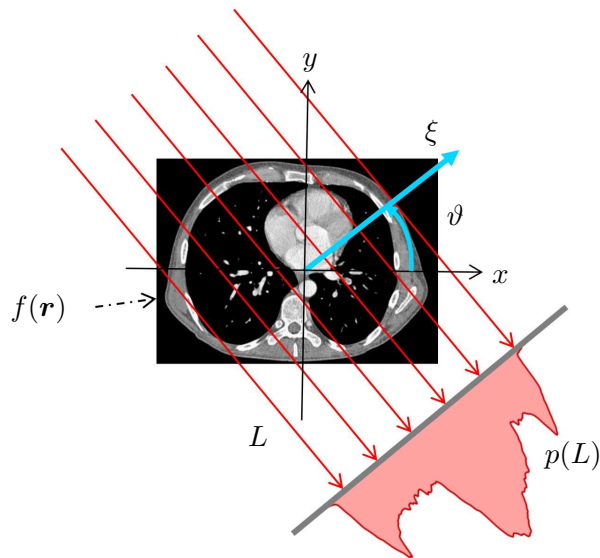


Figure 2.6: Acquisition geometry of the parallel beam measurement setup. The source is translated along ξ . For each translation, the line integral along line L through the patient $f(\mathbf{r})$ is measured in order to acquire the attenuation profile $p(L)$. Once the profile is sampled, the source and detector are rotated around ϑ .

function f that covers the spatial distribution of the attenuation. The exact solution of the inversion of \mathbf{X} is obtained using analytic reconstruction. These methods make some implicit assumptions about the x-ray beam (infinite thin rays, monochromatic x-ray spectrum) and the system geometry. In particular, the parameterization of the lines strongly depend on the selection of the CT system, since it covers the geometry of the system. Shepp and Logan (1974) proposed a two-dimensional (2D) filtered backprojection (FBP) in parallel beam geometry to reconstruct the object function. The parallel beam geometry is illustrated in Figure 2.6. The line traversing the object is parameterized by the angle ϑ and by the distance ξ to the iso-center that coincides with the origin of the coordinate system. An x-ray beam is therefore mathematically expressed by the line equation $x \cos \vartheta + y \sin \vartheta = \xi$. In 2D parallel beam geometry, the x-ray transform \mathbf{X} (2.14) is reformulated to

$$q(\vartheta, \xi) = \int dx dy f(x, y) \delta(x \cos \vartheta + y \sin \vartheta - \xi), \quad (2.16)$$

with $\delta(\cdot)$ being the Dirac delta function. The inversion of \mathbf{X} is obtained by the calculation of the Fourier transformation with respect to the detector index ξ . The Fourier slice theorem states that the 1D Fourier transform of the projections with respect to ξ is equal to the 2D Fourier transform of the object function f in polar coordinates. Since the CT data are measured in spatial domain, a coordinate transform from polar to cartesian coordinates is required and performed by transforming the integration variables. The substitution of the integration variables results in an additional multiplicative term in frequency domain that is known as ramp kernel $K(u) = |u|$. The filtered backprojection

is then

$$f(x, y) = \int d\vartheta q(\vartheta, \xi) * k(\xi) \Big|_{\xi=x \cos \vartheta + y \sin \vartheta}, \quad (2.17)$$

where $*$ is the convolution operator. Prior to reconstruction, the projection values must be convolved with the reconstruction kernel $k(\xi)$ for each ϑ . In a second step, the filtered projections are integrated along the sinusoidal curve $\xi(\vartheta) = x \cos \vartheta + y \sin \vartheta$ with an angular coverage of 180° in order to obtain the exact solution.

However, due to the detector hardware, projection values are only available at discrete points and the filtered backprojection algorithm needs to be implemented in a discrete version. In order to perform the discrete convolution, the ramp kernel needs to be discretized. If $\Delta\xi$ is the sampling distance, the Nyquist sampling theorem results in a band limitation of $b = \frac{1}{2}\Delta\xi$. Therefore, cutting off the kernel at this frequency does not remove spectral components

$$K_b(u) = |u| \Pi\left(\frac{u}{2b}\right) \quad \text{with} \quad \Pi(x) = \begin{cases} 1 & \text{for } |x| < \frac{1}{2} \\ \frac{1}{2} & \text{for } |x| = \frac{1}{2} \\ 0 & \text{else.} \end{cases} \quad (2.18)$$

The discrete version of the ramp kernel is known as RamLak kernel referring to Ramachandran and Lakshminarayanan (1971). Although the RamLak kernel has been directly derived from the requirements of the filtered backprojection, it is necessarily not optimal regarding image quality. A modification of the kernel in Fourier domain is often used to improve the image quality regarding noise, spatial resolution and image contrast. The modification is formulated as multiplication of the RamLak kernel with an apodization function $W_b(u) = W\left(\frac{b}{u}\right)$ with $W(0) = 1$ and $W(x) = W(-x)$ in Fourier domain. Typical apodization functions are one for small frequencies and slowly decrease to zero for higher frequencies. In this notation, the RamLak kernel uses no additional apodization $W^{\text{RL}}(x) = 1$. High frequencies are not suppressed leading to high image noise in the reconstructed images. The Shepp Logan kernel (Shepp and Logan, 1974) compensates this disadvantage and attenuates high frequencies to reduce image noise by weighting the RamLak kernel with $W^{\text{SL}}(x) = \text{sinc}\left(\frac{x}{2}\right)$, where high frequencies are slightly suppressed. The apodization function is shown in Figure 2.7a. Alternatively, a smooth kernel is obtained by weighting the RamLak kernel with e.g. the Hanning apodization $W^{\text{HA}}(x) = \cos^2\left(\pi \cdot \frac{x}{2}\right)$. The filter suppresses large parts of the high frequency components resulting in images with low noise level but also poor spatial resolution (see Figure 2.7a). An alternative definition is given by the generalized Hamming apodization $W^{\text{GH}} = a + (1 - a)\cos(\pi \cdot x)$ with $\frac{1}{2} \leq a \leq 1$ being a weighting parameter. Different selections of the parameter a result in different kernel apodizations, e.g. for $a = \frac{27}{50}$ it reduces to the original Hamming kernel which is drawn in Figure 2.7a. For $a = \frac{1}{2}$ the Hanning apodization is obtained and for $a = 0$ the RamLak kernel. Further kernel definitions and their apodization functions are described in Huesman et al. (1977).

It may be pointed out that there is always the trade-off between image noise and spatial resolution. If most of the high frequencies are removed from the image, the spatial resolution in the reconstructed images is diminished, too. The choice of the reconstruction kernel therefore influences the characteristics of the reconstructed image.

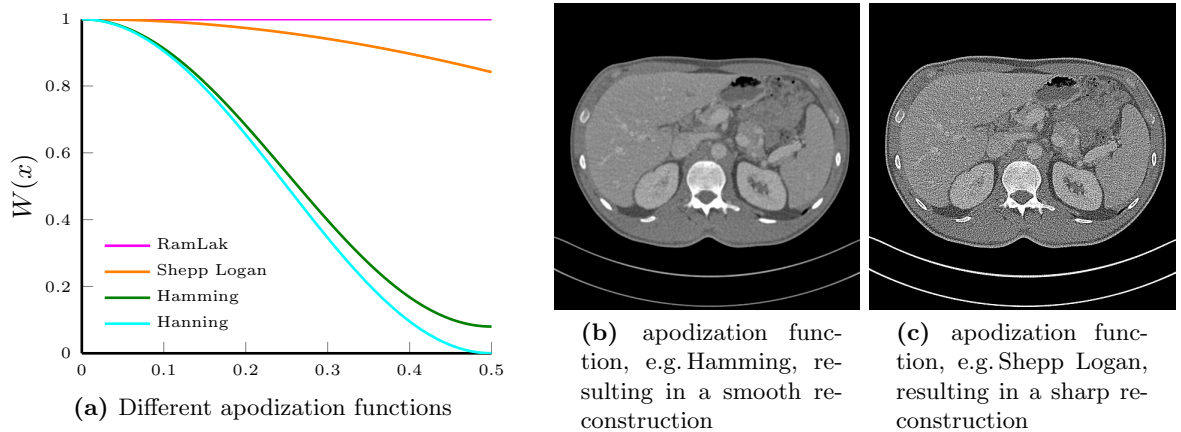


Figure 2.7: There is always the trade-off between high spatial resolution and low noise.

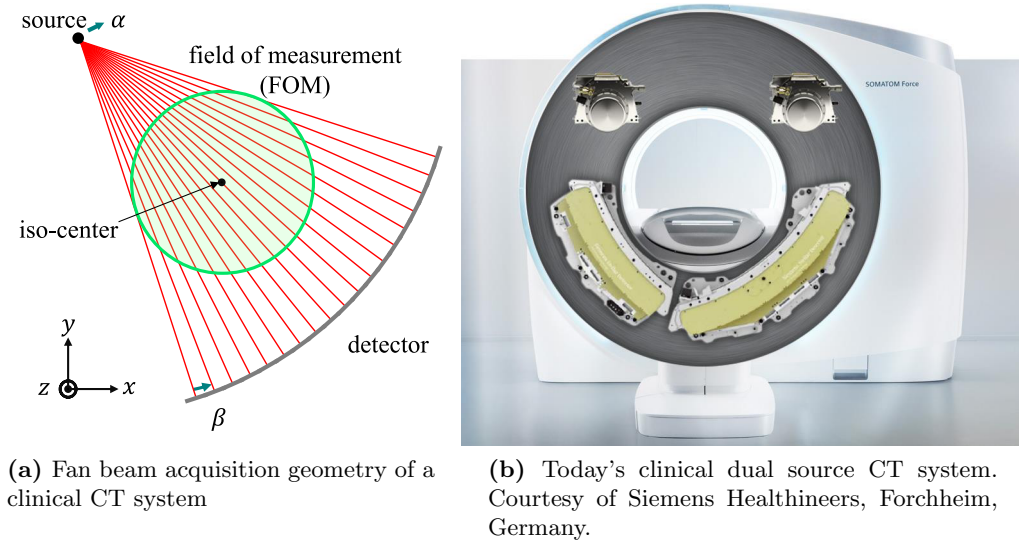


Figure 2.8: Geometry (a) and system (b) setup of a clinical CT. On the left hand side, a sketch of the planar fan beam acquisition geometry neglecting the z -dimension is illustrated. On the right hand side, a dual source CT system consisting of two source-detector pairs is shown.

A smooth high pass filter reduces the spatial resolution but also the noise in the image. On the contrary, a sharp high pass filter has the opposing impact on the image quality. Figure 2.7b and Figure 2.7c illustrates the differences between a sharp kernel reconstruction and a smooth kernel reconstruction. In modern clinical devices, specific reconstruction filters can be selected that are optimized for specific applications regarding desired image properties, such as high spatial resolution, strong edge enhancement, noise reduction or high soft tissue contrast. However, the functional form and their implementation remains proprietary.

Clinical CT System and Geometry

Although nowadays no CT system operates in parallel beam geometry, the data typically acquired in fan beam or cone-beam geometry can often be rebinned such that a 2D parallel reconstruction can be used. The first application of the filtered backprojection algorithm for three-dimensional (3D) image reconstruction from projections acquired in circular scan mode in cone-beam geometry was proposed by Feldkamp et al. (1984). It is an approximate algorithm and fulfills the property that the integral of the reconstructed image along any axial line orthogonal to the plane of the orbit is exact, if the cone-beam projections are not truncated (Rodet et al., 2004). An extension of the Feldkamp algorithm was published by Kachelrieß et al. (2004). The extended parallel backprojection (EPBP) algorithm reconstructs clinical spiral CT data with curved detectors with 100 % dose efficiency. However, each of these approximate algorithms perform a rebinning to parallel beam geometry neglecting the nature of the 3D cone-beam acquisition geometry during the convolution step and this may result in cone-beam artifacts. Katsevich (2003) presented an analytic exact 3D cone-beam reconstruction consisting of convolutions and backprojections without any approximations. However, the dose usage is significantly lower than 100 %.

Alternatively to a cone-beam reconstruction, the data acquired in cone-beam geometry are converted to planar data. The data are rebinned to fit onto so-called reconstruction planes that are aligned with the focus trajectory and reconstructed by means of a 2D filtered backprojection. This approach is preferably applied in clinical spiral CT (Kachelrieß et al., 2000) and first commercially implemented by Schaller et al. (2001). The algorithm was then modified by Stierstorfer et al. (2002) to handle data segments less than 180° . For instance, Siemens implemented a weighted filtered backprojection for multi-slice spiral CT with an efficient dose usage that is applicable for arbitrary pitches (Stierstorfer et al., 2004).

Today's clinical CT systems operate in a fan beam acquisition geometry, where the gantry is continuously rotating around the patient. The system geometry of a dual source CT system is shown in Figure 2.8a. The system setup allows a simultaneous acquisition of the complete field of measurement (FOM) per rotation. The fan beam geometry is described by the fan angle β , which describes the angle of the ray within the fan, and the rotation angle α of the gantry, i.e. the position of the x-ray source. Moreover, all clinical detectors are built with multiple detector rows in z -dimension to enable the simultaneous acquisition of adjacent slices. The acquisition of a 3D volume requires therefore the simultaneous rotation of the x-ray source and the detector and the movement of the patient's table. This system setup is also known as clinical multislice-CT and the technique allows for spiral acquisition trajectories resulting in shorter scan times and a better dose usage. Therefore, the CT acquisition geometry is actually rather a cone-beam geometry as a fan beam geometry. The cone-beam geometry is able to achieve a wide coverage in z -dimension. Nevertheless, in clinical practice the term cone-beam CT (CBCT) is related to a source-detector system which is equipped with a flat detector with low aspect ratio. In this setup, a single circular movement of the source and the detector is sufficient to acquire a 3D volume. However, there is a smooth transition between different notations in the field of clinical CT.

A modern dual source CT system (SOMATOM Definition Force, Siemens Healthineers, Forchheim, Germany), where two source–detector pairs are mounted orthogonal to each other, is shown in Figure 2.8b. The dual source CT system enables shorter scan times, less dose and an improved temporal resolution reducing motion artifacts, e.g. while imaging the heart (Flohr et al., 2006). Moreover, both tubes of the dual source system can be operated with different tube voltage settings. This enables the acquisition of data at two different energies simultaneously (Primak et al., 2010). The principle of dual energy will be discussed in the following.

2.3 Basic Principles of Dual Energy CT

In the early 1970s, the concept of dual energy computed tomography (DECT) was initially formulated by Hounsfield (1973). Since the x–ray attenuation coefficient is energy–dependent, spectral CT exploits the difference in the mass attenuation coefficient of different materials as a function of energy (Maaß et al., 2011b). In case of dual energy, the spatial distribution of the attenuation coefficient is sampled at two different energies, namely at the effective energy of the low and at the effective energy of the high energy spectrum (Faby et al., 2015). Within the clinically relevant energy range between 20 and 150 keV, the photoelectric and the Compton effect dominate the attenuation of organic materials and therefore the spectral data can be decomposed into its two underlying physical effects. Any additional spectral measurement would result in linearly dependent equations and therefore no gain of information would be obtained except if there are K–edges in the clinically relevant energy range. However, in the clinical routine it is more common to make a different basis material selection, e.g. bone and water, instead of the decomposition into photoelectric and Compton cross sections. In general, the linear attenuation coefficient $\mu(\mathbf{r}, E)$ that is independent of the density ρ of the materials can be expressed as a linear combination of an arbitrary material pair that represents a material basis.

$$\mu(\mathbf{r}, E) = f_1(\mathbf{r})\psi_1(E) + f_2(\mathbf{r})\psi_2(E), \quad (2.19)$$

where $f_{1,2}(\mathbf{r})$ denotes the compound basis materials and $\psi_{1,2}(E)$ denotes the known energy dependency. The linear attenuation coefficient can be modeled in different ways

$$\mu(\mathbf{r}, E) = \rho(\mathbf{r}) \left(\frac{\mu}{\rho} \right) (E) \quad (2.20)$$

or

$$\mu(\mathbf{r}, E) = \mu(\mathbf{r}, E_0) \frac{\mu(E)}{\mu(E_0)}, \quad (2.21)$$

where the first term reflects the fact that the attenuation coefficient is proportional to the object density. Secondly, the attenuation map can also be reconstructed at some given display energy E_0 . By using the model of Equation (2.20), the linear attenuation coefficient (2.19) can be decomposed into density maps of specific materials

$$\mu(\mathbf{r}, E) = \rho_1(\mathbf{r}) \left(\frac{\mu}{\rho} \right)_1 (E) + \rho_2(\mathbf{r}) \left(\frac{\mu}{\rho} \right)_2 (E), \quad (2.22)$$

where $\left(\frac{\mu}{\rho}\right)_i(E)$ correspond to the mass attenuation coefficient of material i .

2.3.1 Material Decomposition

In order to perform a material decomposition in its compound basis materials, a scatter-free CT polychromatic measurement is assumed to consist of two materials. The polychromatic projections q_j according to Equation (2.11) are acquired at two different energies $j = 1, 2$ (dual energy)

$$q_j = -\ln \int dE w_j(E) e^{-f_1\psi_1(E) - f_2\psi_2(E)}. \quad (2.23)$$

For simplification purposes, a monochromatic spectrum $w(E) = \delta(E - E_0)$ at the effective energy E_0 is assumed to result in an ideal measurement p

$$p = q(E_0) = f_1(\mathbf{r})\psi_1(E_0) + f_2(\mathbf{r})\psi_2(E_0), \quad (2.24)$$

where $f_i(\mathbf{r})$ are the compound basis materials and $\psi_i(E) > 0$ is the a priori known energy dependency. Since the x-ray transform is linear, the decomposition into its compound basis materials $i = 1, 2$ can be performed either in image domain or in projection domain

$$g = \mathbf{X}^{-1}p = \mathbf{X}^{-1}q(E_0) = \mathbf{X}^{-1}(f_1\psi_1(E_0) + f_2\psi_2(E_0)) \quad (2.25)$$

$$= \mathbf{X}^{-1}f_1\psi_1(E_0) + \mathbf{X}^{-1}f_2\psi_2(E_0) \quad (2.26)$$

The decomposition operator D in the image domain is given by

$$f_i = D_i(g_L, g_H) = D_i(\mathbf{X}^{-1}q_L, \mathbf{X}^{-1}q_H), \quad (2.27)$$

where q are the measured polychromatic projections. A water-precorrection algorithm (Kachelrieß et al., 2006) needs to be applied to q in advance. The decomposition operator in the projection domain is given by

$$f_i = \mathbf{X}^{-1}p_i = \mathbf{X}^{-1}D_i(q_L, q_H). \quad (2.28)$$

The direct decomposition of the polychromatic projections q_L and q_H is usually preferred, since it is able to inherently avoid beam hardening artifacts in the material images (Alvarez and Macovski, 1976). However, the decomposition in projection domain implicitly presumes consistent ray sampling (Maaß et al., 2011a), whose technical realization is rather difficult. Therefore, the decomposition in image domain remains often the method of choice in clinical practice (Brooks, 1977; Coleman and Sinclair, 1985; Maaß et al., 2009). In order to decompose into more than two basis materials, additional assumptions about the material mixing behavior needs to be made. The following section discusses two possible assumptions on volume and mass conservation and the relationship between both assumptions.

2.3.2 Material Mixtures: Volume and Mass Conservation

Given are two materials $i = 1, 2$ that are characterized by their mass attenuation coefficient $\kappa_i(E) = \left(\frac{\mu}{\rho}\right)_i(E) = \frac{\mu_i(E)}{\rho_i}$, where $\mu_i(E)$ is the linear attenuation coefficient and ρ_i is the mass density of the corresponding material i . These two materials with volumes V_1 and V_2 are mixed such that the volume of the mixture is equivalent to the sum of the volumes of the mixing constituent materials $V = V_1 + V_2$ (volume conservation). The mass of the mixtures is therefore given by

$$m = \rho_1 V_1 + \rho_2 V_2 \quad (2.29)$$

and the mixture density results in

$$\rho = \frac{\rho_1 V_1 + \rho_2 V_2}{V_1 + V_2} \quad (2.30)$$

In volumetric mixtures the linear attenuation coefficient mixes linearly with the volumetric fractions

$$\mu(E) = \mu_1(E) \frac{V_1}{V_1 + V_2} + \mu_2(E) \frac{V_2}{V_1 + V_2} = \mu_1(E) \phi_1 + \mu_2(E) \phi_2. \quad (2.31)$$

A volumetric fraction ϕ_i of material i is defined by the ratio between the volume of the mixing constituent V_i and the total volume of the mixture V . The mass attenuation coefficient mixes according to the mass fractions of its constituents

$$\kappa(E) = \kappa_1(E) \frac{\rho_1 V_1}{\rho_1 V_1 + \rho_2 V_2} + \kappa_2(E) \frac{\rho_2 V_2}{\rho_1 V_1 + \rho_2 V_2} = \kappa_1(E) \omega_1 + \kappa_2(E) \omega_2. \quad (2.32)$$

A mass fraction ω_i is determined by the ratio between the mass of the mixing constituent m_i and the total mass of the mixture m . The extension of Equation (2.31) and Equation (2.32) to M material constituents yields

$$\mu(E) = \sum_{i=1}^M \mu_i(E) \cdot \phi_i \quad \text{with } \phi_i = \frac{V_i}{V} \quad (2.33)$$

$$\kappa(E) = \sum_{i=1}^M \kappa_i(E) \cdot \omega_i \quad \text{with } \omega_i = \frac{m_i}{m} \quad (2.34)$$

for the linear attenuation coefficient $\mu(E)$ and the mass attenuation coefficient $\kappa(E)$ of a mixture. The total volume of the mixture is given by $V = \sum_{i=1}^M V_i$ and the total mass of the mixture is given by $m = \sum_{i=1}^M m_i$, respectively. In principle, dual energy provides only two independent measurements and therefore it is implicitly restricted to decompose the data only into two independent material components. However, in order to decompose the dual energy data into more than two materials, e.g. three basis material components, an additional assumption on the mixing behavior needs to be made. Often, it is assumed that the sum of the volumes of each constituent material is equivalent to the volume of the mixture (Yu et al., 2009). This assumption is not true for every mixture (Liu et al., 2009). The authors state that the volume of a salt–water solution is

not equal to the sum of the individual volumes of salt and water.

Based on the assumption of volume conservation a relationship between mass fractions ω and volume fractions ϕ was established by Mendonça et al. (2014). The linear attenuation coefficient and the mass attenuation coefficient are related by their density ρ . The derivation of a relationship between the linear attenuation coefficient and the mass attenuation coefficient yields

$$\mu(E) = \rho \cdot \kappa(E) = \rho \sum_{i=1}^M \kappa_i(E) \cdot \omega_i \quad (2.35)$$

$$= \frac{m}{V} \sum_{i=1}^M \frac{m_i}{m} \frac{\mu_i(E)}{\rho_i} = \frac{1}{V} \sum_{i=1}^M \frac{m_i}{\rho_i} \mu_i(E) \quad (2.36)$$

$$= \sum_{i=1}^M \frac{V_i}{V} \mu_i(E) = \sum_{i=1}^M \mu_i(E) \cdot \phi_i. \quad (2.37)$$

Therefore, a model for the density of the mixture ρ requires both mass and volume conservation. They observed an implicit dependency of the assumption of volume and mass conservation for the decomposition into more than two materials. They pointed out that each reasonable decomposition into more than two basis materials that rely on the assumption of volume conservation implicitly makes an assumption on mass conservation. The problem of saline solutions and the assumption of volume conservation might be relaxed by applying the assumption to a solution of water and already diluted salt instead of a solution of salt and water (Mendonça et al., 2014). Therefore, the assumption results in a realistic approximation of the mixing behavior in the human body and yields accurate results.

2.4 Clinical Dual Energy CT and its Applications

In clinical dual energy computed tomography (DECT) applications, the dual energy information is often used to differentiate between two materials, e.g. the classification of kidney stones, or to decompose the DE data into material-specific images in order to quantify, for instance, the contrast media content in the liver. Furthermore, the dual energy information can also be exploited to perform a contrast enhancement via blending of both energies in order to optimize the contrast-to-noise ratio (CNR) and therefore to reduce the noise level or to remove metal artifacts in the combined image. The most common application of a two material differentiation is the detection and analysis of different renal stones consisting either of calcium oxalate or uric acid (Graser et al., 2008; Stolzmann et al., 2010; Boll et al., 2009; Hidas et al., 2010) or the detection of monosodium urate crystals (gout) in the joints (Manger et al., 2012; Choi et al., 2009; Nicolaou et al., 2010). Both types of renal stones have a different chemical composition and therefore may show a different energy-dependent behavior. In single energy CT scans, it is impossible to separate these materials from each other, since they show similar CT values resulting in ambiguities during diagnosis. Since iodine and calcium also show differences in the attenuation behavior at two different energies, iodine and calcium can be clearly separated from each other. Therefore, this principle is often applied

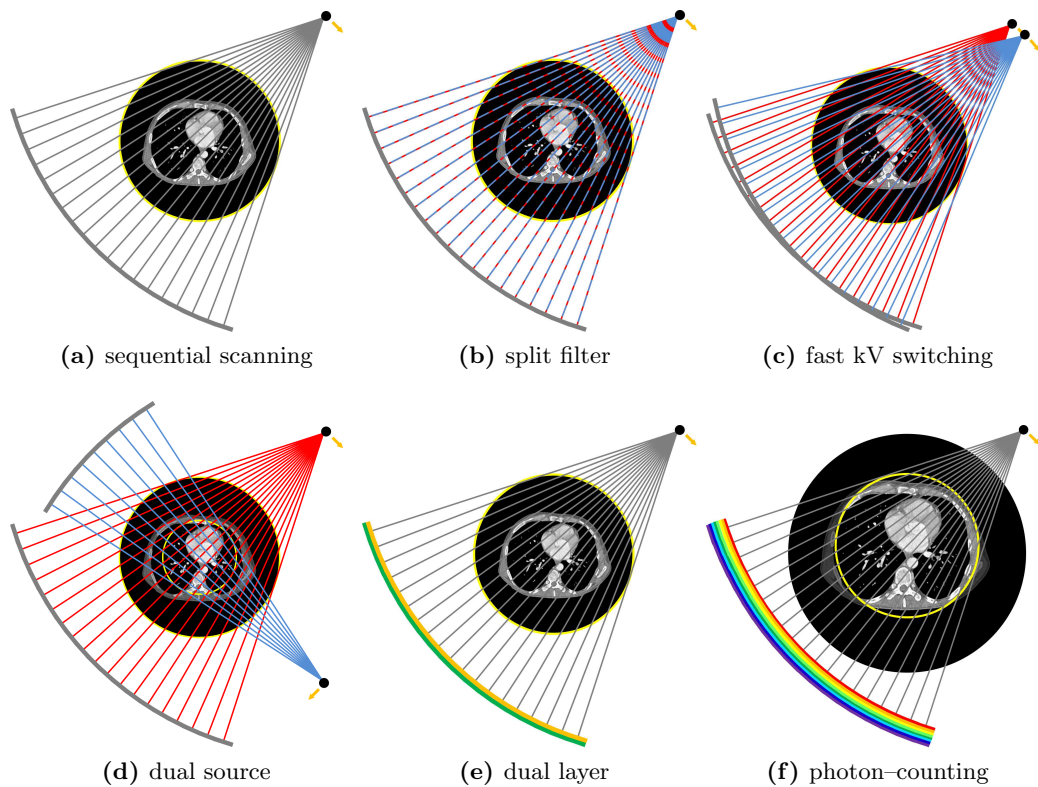


Figure 2.9: The technical realizations can be categorized into either single source DECT, e.g. (a) sequential scanning (b) split filter or (c) fast kV switching, dual source DECT (d), or detector-based DECT, i.e. (e) dual layer or (f) photon-counting detectors. The yellow circle highlights typical field of measurements (FOM), where data relating to two different energy spectra is available. The figure is modified according to Faby et al. (2015).

to artificially remove Ca^{2+} in plaque and bone from the iodinated vessels to highlight the vascular system, e.g. in a 3D rendering. In general, dual energy data are used to decompose the CT data into material-specific images. The most common application is the decomposition into a water and an iodine image to quantify and display the iodine concentration usually in a color-coded fashion in different anatomical structures, e.g. the lung (Thieme et al., 2009), liver, brain or in the heart. Moreover, a virtual removal of the contrast media distribution is possible. The virtual non-contrast (VNC) image or virtual unenhanced (VUE) image is mimicking a native scan and could potentially replace the additional scan prior to contrast media injection reducing patient dose. This principle can also be applied to artificially remove the calcium content from the bones to display any CT value increase due to an infiltration or bone bruising (Pache et al., 2010). As a prerequisite described in Section 2.3, the spatial distribution of the attenuation coefficient needs to be sampled at two different energies in order to perform dual energy material decompositions. Most of the clinical applications are based on a two material decomposition as shown in Section 2.3.1. Depending on the acquisition strategy, the material decomposition can be carried out in image or projection domain. The technical realizations to acquire dual energy data can be categorized into single source dual energy techniques, e.g. sequential scanning (Fig. 2.9a), split filter (Fig. 2.9b) or fast kV switching (Fig. 2.9c), dual source dual energy (Fig. 2.9d) and detector-based

dual energy techniques, e.g. dual layer detectors (Fig. 2.9e) or photon-counting detectors (Fig. 2.9f). The most common classification of dual energy acquisition systems that are clinically available nowadays mainly differentiates between single source and dual source. Therefore, this notation will be used in the following discussion. Photon-counting detectors are able to distinguish more than two energies and thus dual energy CT is only a special case. However, photon-counting detector-based dual energy CT is not yet commercially available and currently not intended for patient examinations. The comparison of commercially available DECT technologies reveals that single source dual energy usually results in a poor spectral separability and decreased dose efficiency. In particular, some approaches suffer from a poorer temporal coherence (Euler et al., 2016) compared to others. The technical realizations, the advantages as well as disadvantages of the systems that are used in clinical practice are described in more detail in the following sections. Moreover, a brief overview of implemented clinical dual energy evaluation schemes will be given. Vendor-specific terminologies are highlighted in *italic* throughout the following sections.

2.4.1 Sequential Dual Energy

The most naive way to generate dual energy data is to perform two consecutive spiral scans at two different tube voltages to generate measurements at two different spectra (Millner et al., 1979). The tube voltage is varied between each rotation resulting in temporally incoherent projection data of the low and high energy data. The selection of potential tube voltages to maximize the spectral separability of both spectra is often not restricted to a predefined range. Additional prefilter to shape the x-ray beam might be inserted without high technical effort. However, the sequential acquisition technique suffers from the absence of temporal coherence between both scans and the data may be degraded by artifacts caused by patient motion during the acquisition (Johnson et al., 2007). In case of contrast media injection, the temporal bolus distribution of the contrast agent may differ significantly between both scans. The decomposition of dual energy data acquired in this setup is only possible using image-based processing. Sequential scanning is realized by all of the large vendors.

2.4.2 Split Filter Dual Energy

Another choice to acquire dual energy data is to place a spectral filter, consisting of two different materials, e.g. gold (Au) and tin (Sn), in front of the x-ray source. Along the longitudinal direction, each of these filter materials covers half of the detector rows (Lifeng et al., 2016). An x-ray spectrum is then prefiltered before entering the patient by these two materials and split into two spectra (Almeida et al., 2017). The spectrum passing through Sn is hardened resulting in a high energy spectrum and the spectrum passing through Au is softened because of the K-edge at 80.7 keV resulting in a low energy spectrum (Euler et al., 2016). Dual energy data can simultaneously be acquired for the same slice during spiral scanning with low pitch. The spectral separation of the x-ray source spectrum allows for the reconstruction of a low and a high energy image, where only the associated half of the detector is utilized. Moreover, it is possible to provide a conventional image, which is reconstructed from the raw data acquired with

the whole detector. This image should imitate the image characteristics of a conventional CT image at a dedicated tube voltage setting. The technology is named *TwinBeam Dual Energy* and commercially available at the Siemens *SOMATOM Definition Edge* and *SOMATOM Definition AS+* since 2015 (Euler et al., 2016). Typically, a tube voltage setting of 120 kV is used resulting in a mean photon energy of 68 keV for the low energy and a mean photon energy of 86 keV for the high energy spectrum. The dual energy technology is dose neutral, since it does not require an additional acquisition. Most recent developments presented by Yu et al. (2016, 2018) propose the placement of a third prefilter material or to add split filters in front of both tubes of a dual source CT system, which will be discussed later on, to acquire multi energy data.

2.4.3 Fast kV Switching Dual Energy

Instead of using a prefilter to split the spectra into two parts, the spectrum can be alternated by rapidly switching the tube voltage of the x-ray source between 80 kV and 140 kV at sub-millisecond speed. Dual energy projection data are acquired twice for every projection, where the tube voltage follows a pulsed curve. However, the slope of the rise and fall of the modulation curve needs to be as abrupt as possible to maximize the energy separation and angular view sampling (McCullough et al., 2015). Since the radiation output of the low kV is significantly reduced in comparison to the high kV output, the tube current should be modulated inversely to the tube voltage to balance the dose output of the low and high energy data (Grasruck et al., 2009). The number of photons is therefore kept constant in order to obtain a similar noise level in both images (Chandra and Langan, 2011). In the 1980s, the first scanner *SOMATOM DRH* (Siemens Healthineers, Forchheim, Germany) was commercially introduced that allows the modulation of the x-ray tube voltage between low and high to acquire interleaved projections in one rotation (McCullough et al., 2015). However, since there were competing applications with less radiation burden, e.g. x-ray absorptiometry for the analysis of vertebral bone mineral density, the dual energy kV switching technique was discontinued (Krauss et al., 2015).

The technology was then revived by GE Healthcare on the *DiscoveryTM CT7750 HD* in 2010 and the dual energy scan mode is called *Gemstone Spectral Imaging (GSI)* (Zhang et al., 2011). The newest generation of ultra-fast kV switching is implemented in the *Revolution CT GSI Xtream* (Slavic et al., 2017). However, since the afterglow performance and the primary decay of the detector are critical to avoid spectral blurring between different views (Li, 2013), an isotropic ceramic scintillator with a highly uniform and translucent cubic structure is used as detector material (Slavic et al., 2017). The detector provides a full field of measurement of 50 cm enabling also the scanning of larger patients. The acquired projections are nearly perfectly registered in terms of temporal and spatial coherence such that a projection-based material decomposition into basis material images is preferred in most of the use cases. The routine to perform dual energy evaluations can be described as follows. The acquired interleaved projection data are split into the low and high kV projections parts that are aligned in projection domain. In order to perform a quality check, the high kV projections are reconstructed. A fully physics-based projection space material decomposition is applied to decompose

the low and high kV data into material-specific projections. Using known curves of the basis materials' attenuation coefficients, i.e. water and iodine, calcium and uric acid, the algorithm decomposes the low and high kV data into material density projections that are reconstructed to generate material-specific images (Slavic et al., 2017). Virtual monochromatic images from 40 to 140 keV are synthesized by a linear combination of basis material images. Moreover, material density images are reconstructed, e.g. iodine, calcium, hydroxyapatite (HAP), fat or uric acid images that enable the quantification and classification of different materials in the human body. By means of an image-based multi material decomposition, virtual unenhanced images are generated by replacing the volume fraction of iodine from the images (Slavic et al., 2017; Mendonça et al., 2014). Moreover, *GSI* provides a metal artifact reduction based on the linear combination of material-specific projection prior to reconstruction.

2.4.4 Dual Layer Detector Dual Energy

The acquisition of dual energy data using a dual layer detector system falls into two categories simultaneously. It can be either considered as single source dual energy or as detector-based dual energy technology. A detector consisting of two layers of scintillators on top of each other is exposed by an x-ray tube (Fahmi et al., 2016). The top layer is a yttrium-based garnet scintillator whereas the upper layer is a gadolinium oxysulfide (GOS) scintillator. The readout is carried out by side-locked photodiodes, which also act as anti scatter grid. The upper layer further serves as prefilter for the lower layer resulting in a hard high energy spectrum. In order to acquire the DECT data, a single CT scan is performed at high tube voltage, e.g. 120 kV or 140 kV, where the energy separation of 140 kV is higher than that at 120 kV. The upper layer absorbs most of the low energy spectrum while the remaining high energy photons are absorbed by the lower layer. Compared to the above mentioned dual energy techniques, it is not necessary to redundantly expose the patient with two different energy spectra (Vlassenbroek et al., 2018). The spectral separation is intrinsically given by the detector design rather than sequentially generated by the x-ray source (Vlassenbroek, 2011).

Dual layer detector dual energy scans deliver fully spatial and temporal registered projection in the same full field of view for both energies simultaneously, which enable material decomposition directly in projection domain. A conventional full spectrum image can easily be generated by a weighted summation of both projections. Furthermore, projections corresponding to each detector layer can separately be reconstructed. In other words, using dual layer technology, a conventional image as well as the spectral information is always intrinsically available without any further effort. Since the spectral separation between both spectra for small tube voltages below 120 kV is not sufficient, scans with a tube voltage smaller than 120 kV are solely intended for the reconstruction of conventional CT images using both projections. Philips Healthcare integrated the dual layer detector technology into its *IQon Spectral CT*. In order to provide spectral evaluations with the *IQon Spectral CT*, the low and the high energy projections are decomposed into its contributing physical effects and reconstructed to spectral basis images (SBI). These SBIs are then used to compute virtual monoenergetic images (*MonoE*), material-specific material density images, e.g. iodine density image or ρ/Z images.

These images are further processed to perform a calcium suppression or the calculation of a VNC image and iodine concentration map.

2.4.5 Dual Source Dual Energy

Two x-ray sources, each equipped with their own high voltage generator, and two fully-equipped data acquisition systems are mounted on the same gantry orthogonally to each other. Both independent imaging chains acquire two spiral scans simultaneously by running each x-ray source at a different tube voltage (Flohr et al., 2006; Johnson et al., 2007). The first dual source CT scanner *SOMATOM Definition* was introduced by Siemens Healthineers in 2005 (Flohr et al., 2006; Achenbach et al., 2006). In this first *SOMATOM Definition*, one of the sources operated at 80 kV and the other source operated at 140 kV. In order to achieve a sufficient spectral separation for DE acquisitions of obese patients, the tube corresponding to the low energy acquisition chain was able to run at 100 kV. In 2008, a second-generation dual source scanner *SOMATOM Definition Flash* was introduced (Krauss et al., 2011). The scanner is equipped with an additional 0.4 mm tin filter to perform an additional prefiltration of the high kV beam. The prefiltration removes low energy photons from the incident beam in order to maximize the spectral separation (Primak et al., 2009, 2010). This spectral shaping of the high kV beam results in a substantial improvement in material classification (Primak et al., 2009; Stolzmann et al., 2010; Kelcz et al., 1979) and significant dose reduction to levels of single source CT, since the removed photons would have otherwise been absorbed in the patient (Henzler et al., 2012). Using the tin prefilter, the scanner achieves a similar spectral separation with the tube voltage combination of 100/140 kV+Sn compared to the previous *SOMATOM Definition* 80/140 kV while reserving a higher x-ray tube power at the low kV improving the DE imaging capability for obese patients (Primak et al., 2010; Krauss et al., 2015). With the advent of the third-generation dual source scanner *SOMATOM Definition Force* tube voltage settings in the range of 70 kV to 150 kV with a step size of 10 kV for both x-ray tubes and 0.6 mm tin prefiltration of the high kV spectrum are available (Krauss et al., 2015). Dual source dual energy CT acquires perfectly registered data by inconsistent rays of two independent systems. In this setup, therefore, image-based material decompositions are mostly preferred. The applications, which are commercially available, are solely implemented in image-domain. However, it should be noted that the decomposition in projection-domain is certainly more challenging but also possible with the “MDIR” algorithm proposed by Maaß et al. (2011a).

The material-specific dual energy applications that are implemented in the *Siemens Syngo.CT Dual Energy* software rely either on a material decomposition as depicted in Figure 2.10a or a material classification as depicted in Figure 2.10b. Each of these approaches operates in image domain, i.e. based on the CT value distribution of the low and the high energy image. The low (L) and the high (H) energy image span a plane that is usually known as dual energy diagram. The dual energy measurement of a voxel can therefore be interpreted as a point in the DE space, where the CT value of the low energy image is plotted against the CT value of the high energy image. In general, the dual energy diagram implicitly serves as a starting point for material decomposition in

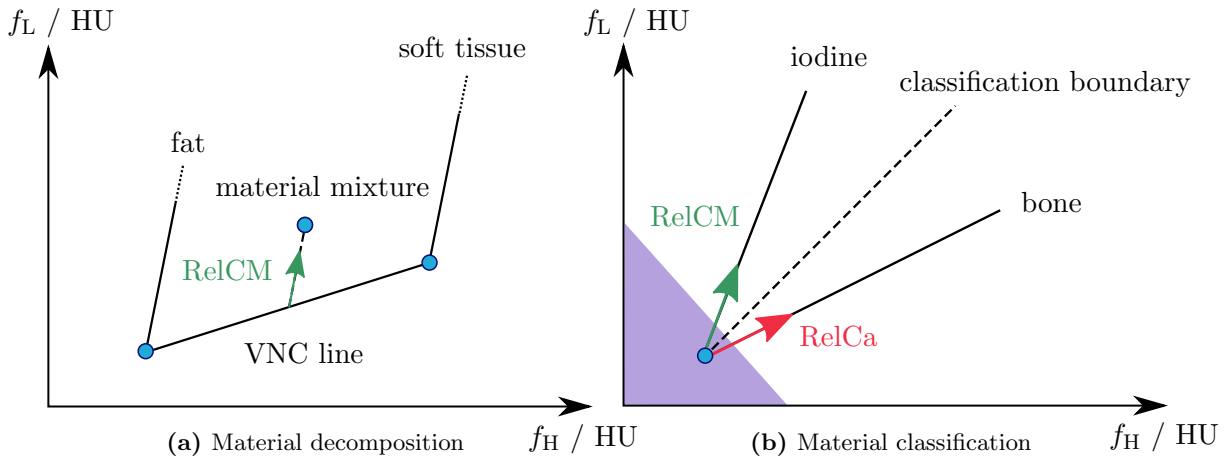


Figure 2.10: Basic principle of Siemens DE applications in image domain. (a) The three material decomposition with one point at infinity. The removal of the iodine enhancement corresponds to a parallel projection onto the virtual non-contrast (VNC) basis line. The length of the parallel projection is similar to the iodine concentration in the image. The iodine contrast ratio RelCM points towards pure iodine. (b) Material classification that is used to differentiate between two materials with known relative contrast ratios. The differentiation is given by the signed distance to the classification boundary. Usually there is an additional threshold which ensures that values below a certain CT value are not considered in the classification (violet shading).

image domain.

The material decomposition is utilized for all kinds of material quantification, e.g. calculation of iodine overlays. On the contrary, the material classification is applied to discriminate and highlight two materials from each other, e.g. the classification of the composition of kidney stones. The material decomposition method decomposes the DECT data into two basis material images. The material classification, on the other hand, differentiates two possible materials with respect to a certain decision boundary (Krauss et al., 2011; McCollough et al., 2015). The material decomposition, e.g. the quantification of iodine, corresponds to a parallel projection onto the virtual non-contrast (VNC) line. Two reference points in the DE space determine the slope of this base line. A relative contrast ratio RelCM points toward pure iodine and corresponds to the relative iodine contrast in the image (Krauss et al., 2015; Dorn et al., 2018b). The iodine concentration of the voxel to be decomposed is proportional to the length of the parallel projection. The material classification is based on the differentiation between two materials with known relative contrast ratio in the image. The classification is then given by the sign of the distance to the decision boundary.

Typical material decomposition applications available at the *Siemens Syngo.CT DE* are, for instance, the imaging of the perfused blood volume in the lung (*Lung PBV*) or in the heart (*Heart PBV*) to reveal any perfusion defects. The decomposition into VNC and iodine maps in the body (*Virtual Unenhanced*), the liver (*Liver VNC*), or the brain (*Brain Hemorrhage*). The visualization of the iodine uptake assists in the characterization of lesions or detection of bleedings. The *Bone Marrow* application

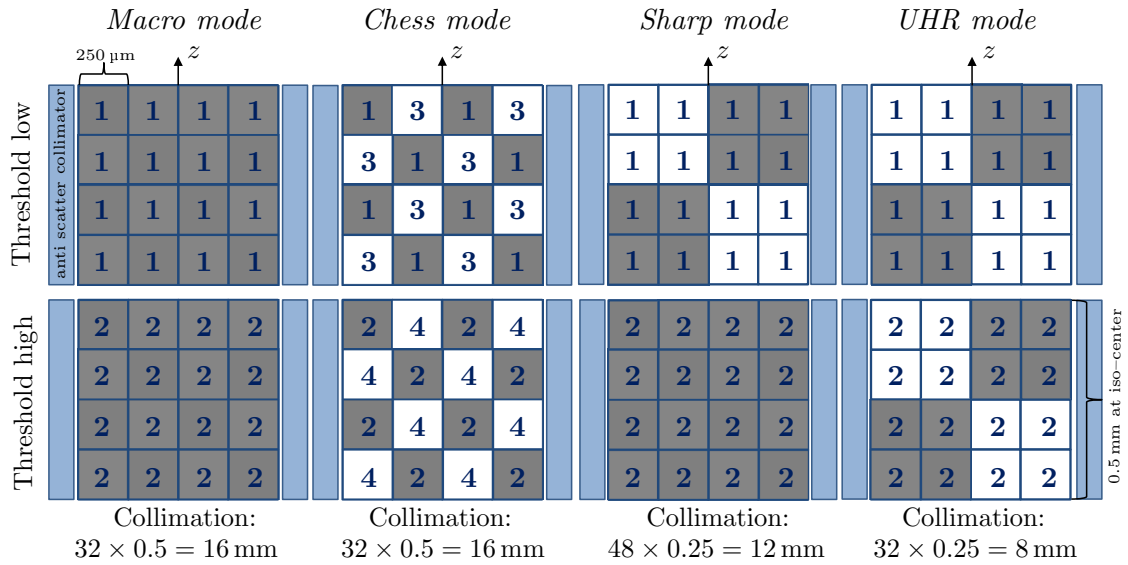


Figure 2.11: CountT detector read out scheme for the low (upper row) and the high (lower row) energy threshold for four acquisition modes. The macro mode is the standard read out mode. The chess mode enables the acquisition of four energy bins. The sharp and UHR mode are high spatial resolution modes. The figure is modified according to Leng et al. (2017).

allows for the decomposition into bone marrow and calcium and helps to identify any bone bruising after an infiltration of diffuse tumors or trauma. Material classification applications that are implemented in the *Siemens Syngo.CT DE* are the classification of kidney stones (*Calculi Characterization*), the detection of gout (*Gout*), the removal of bone (*Bone Removal*) and the advanced isolation and highlighting of even complex vasculature (*Direct Angio*). Moreover, the *Hardplaque Display* application enables the identification and automatic removal of calcifications from the vessels in order to identify the true vessel lumen without interfering with hard plaque.

2.4.6 Photon-Counting Detector Dual and Multi Energy

Major vendors recently presented novel CT prototypes, which are equipped with photon-counting detectors. This innovative detector technology consists of semi conductive materials as direct x-ray converters. A typical detector material is cadmium telloride (CdTe), where the incident photon creates an electron-hole pair. The number of pairs is directly proportional to the x-ray energy. An external electric field causes a fast drift of charges. The electrons induce short charge pulses when approaching the pixelated anode pads. By comparing each pulse in a pixel with suitable energy thresholds, the contributions of different photon energies can be sorted in corresponding energy bins. The detected signal correspond to an energy-selective counter signal. Depending on the number of energy thresholds per pixel, the technology allows for dual or even multi energy CT. Siemens developed a hybrid prototype *SOMATOM Definition CounT*, which is based on a second-generation dual source CT scanner as described previously.

One of the energy-integrating detectors is replaced by a CdTe photon-counting detector, which consist of 30 modules with 128×64 quadratic detector sub pixels with a pitch of 225μ m yielding a field of measurement (FOM) of 27.5 cm at the iso-center (Kap-

pler et al., 2014). The detector material is 1.6 mm thick to provide an x-ray stopping power comparable to common energy-integrating CT scanners (Polster et al., 2016). The technical implementation of the system is described in more detail by Kappler et al. (2010, 2012, 2013, 2014). However, the scanner only operates in single source mode. The second source-detector pair is often used for data completion in order to remove truncation artifacts due to the small FOM in the photon-counting scan and for comparison purposes with a conventional energy-integrating detector. The smallest readout unit of the photon-counting detector is denoted as macro pixel with a pixel size of 0.5 mm at the iso-center similar to a conventional CT detector pixel. A macro pixel is obtained by binning 4×4 sub pixels and therefore the size of the sub pixels is the only limiting factor of the detector's spatial resolution. Moreover, each of the sub pixels features two individually adjustable energy thresholds, yielding two energy bins for each of the acquisition modes. The lower threshold is restricted to the energy range of 20 to 50 keV and the upper threshold is restricted to the energy range of 50 to 90 keV.

There are four different acquisition modes, i.e. detector read out schemes, which are illustrated in Figure 2.11. The standard scanning mode is denoted as macro mode, where 4×4 sub pixels are grouped together resulting in a pixel size of 0.9×0.9 mm corresponding to 0.5×0.5 mm at the iso-center. This configuration is equivalent to the geometry of the anti-scatter collimator that is placed on top of the direct converter (Kappler et al., 2014). The maximum z-coverage is 32×0.5 mm = 16 mm. Moreover, the sub pixel thresholds of the macro pixel can be configured in chess patterns allowing for a virtual extension to four energy bins (Kappler et al., 2012). This is done by interleaving the 4×4 sub pixels into two alternating pixel groups of eight sub pixels. The thresholds of the first group are adjusted to energies E_1 and E_2 and the thresholds of the second group are adjusted to energies E_3 and E_4 . Each adjacent pixel has therefore a different threshold energy compared to its neighbor. The missing energy information in the macro pixel is binned 4×4 resulting also in 16 cm z-coverage. This acquisition mode is referred to as chess mode enabling novel spectral imaging techniques such as multi energy imaging or K-edge imaging (Kappler et al., 2012).

To take advantage of the smaller native detector pixel size, there are two imaging modes with ultra-high spatial resolution in which 450×450 μ m detector pixels are used corresponding to a effective pixel size of 0.25×0.25 mm at the iso-center (Leng et al., 2017). However, the read out scheme between both ultra-high spatial resolution modes differ significantly. The first scan mode is referred to as sharp mode, whereas the low energy acquisition uses the 2×2 binning and the high energy acquisition maintains the pixel size of the macro mode. The used z-collimation of 48×0.25 mm results in a longitudinal detector coverage of 12 mm. The second ultra-high spatial resolution mode is denoted as UHR mode, where both the low and the high energy acquisition use 2×2 binning. In this UHR mode, less detector rows are usable and therefore the collimation is limited to 32×0.25 mm yielding a decreased longitudinal coverage of 8 mm of the detector.

The photon-counting system intrinsically provides higher spatial resolution with a higher contrast-to-noise ratio as well as strongly reduced crosstalk. Therefore, the introduction of photon-counting CT promises potential dose reduction compared to con-

ventional CT systems and implicit dual energy capability without the need of scanning the patient at different kV settings (Kappler et al., 2010). The spectral information is available making a retrospective dual energy evaluation possible in any case. The low energy threshold image correspond to a conventional CT image since each photon with an energy larger than threshold E_1 contributes to the image. Bin images are obtained by subtracting neighboring threshold images. In case of two thresholds, the second bin image is similar to the high energy threshold image. CT images reconstructed from threshold data show different properties than those reconstructed from bin data, even though the data representation includes the same amount of information (Kappler et al., 2013).

CHAPTER 3

Materials and Methods

In this chapter, a context-sensitive imaging for single, dual or multi energy CT is introduced. With the use of prior anatomical information (see Section 3.1), conventional CT imaging strategies are extended to provide an innovative novel CT imaging concept. The following chapter is organized as follows. Section 3.2 presents a context-sensitive image formation that combines the advantages of various reconstruction and display techniques. In Section 3.3 numerous common dual energy applications (Liver VNC and iodine overlays, gout, kidney stones classification, lung perfusion, etc.) are combined into one single analysis tool exploiting anatomical prior information. The parameters for clinically approved dual energy applications can be selected fully automatically in order to improve the clinical workflow. Parts of the context-sensitive image formation and context-sensitive dual energy evaluation are developed within the scope of a cooperation project supported by the German Research Foundation and have been published in Dorn et al. (2018a,b,c). Moreover, a novel method improving the iodine quantification accuracy using patient-specific calibrations will be presented. The principle of incorporating anatomical priors is extended in Section 3.4 to provide a quantitative pseudo multi material decomposition consisting of multiple three material decompositions in image domain.

3.1 Anatomical Prior Information

In this work, it is assumed that an ideal multi-organ segmentation is given. The focus of this work is to demonstrate how CT imaging can benefit from incorporating anatomical prior information and to provide a more sophisticated anatomy-adapted imaging but not to develop an automatic multi-organ segmentation. Therefore, the following section will be limited to providing a short review of commonly used automatic segmentation approaches and to briefly recap the automatic segmentation approach, which is used to generate the organ and tissue labeling. However, it should be pointed out that the automatic segmentation is no part of the main contributions of this work and should be considered as black box in the following sections.

Most promising automatic segmentation approaches are either based on probabilistic atlas-based methods (Chen et al., 2017; Lavdas et al., 2017; Okada et al., 2008; Wolz et al., 2013; Park et al., 2004) or deep learning-based segmentation approaches (Ronneberger et al., 2015; Roth et al., 2017; Tong et al., 2018; Gibson et al., 2018; Chen et al., 2018a,b,c). Atlases are widely used in the field of medical imaging to provide anatomical prior knowledge and reference data or to examine the variability of different anatomies. An atlas is registered onto newly acquired image data in order to transfer additional information from the atlas to the image and to display both data sets in a common reference coordinate system. Using probabilistic atlases to provide a multi-organ segmentation was first proposed by Park et al. (2004). A probabilistic atlas is generated by multiple registrations between a training set and different individual reference sets. It does not simply detect the average boundary of an organ but the complete spatial distribution of the probability that a voxel belongs to one certain organ. By aligning the atlas onto one target volume, i.e. current patient, the anatomical structures are automatically segmented and classified.

In this work, the automatic segmentation to generate the anatomical prior knowledge is obtained using a cascaded fully convolutional neural network (Chen et al., 2018c) based on the U-net proposed by Ronneberger et al. (2015). The U-net is a fully connected convolutional neural network (CNN) (Long et al., 2015) that consists of a contracting path and a symmetric expanding path (Ronneberger et al., 2015; Çiçek et al., 2016). It was initially developed for biomedical image segmentation. Since the initial U-net was implemented for 2D images neglecting the inter-slice anatomical context, the CNN was further extended to 3D volumetric data by Çiçek et al. (2016). The task of automatic multi-organ segmentation is often partitioned into two minor tasks instead of using an end-to-end approach in order to improve the overall segmentation performance. The detection followed by a segmentation showed promising results as stated by Roth et al. (2017) and Tang et al. (2018).

Chen et al. (2018a) pursued the idea of splitting the segmentation task into a localization and detection task for the segmentation of DECT data. They proposed a network architecture which consists of two cascaded U-nets where each of the U-nets is trained separately. The first U-net was trained and applied to detect the abdominal cavity in order to reduce the search space for the final multi-organ segmentation. The second U-net is fine-tuned from the first-stage fully connected network in a hierarchical manner in order to detect the final organ boundaries. The output of the second stage is a prediction map wherein each value indicates the probability of the voxel belonging to a certain organ. The final segmentation result is consequently defined by the maximum intensity of these class probability maps. The cascaded 3D fully connected CNN segments SECT and DECT data into different organs, i.e. right and left lung, right and left kidney, spleen and liver. In case of SECT data, the volume to be segmented is directly fed into the network. In case of DECT data, the dual energy information is linearly combined beforehand.

In the current version, Chen et al. (2018b,c) introduce an end-to-end network that recombines the localization and detection task and analyze different strategies to fuse the dual energy information. The dual energy information can either be fused by integrating

a merge layer with one trainable parameter as first layer in the U-net to calculate a linear combination or by treating the two dual energy volumes as a two-channel input. The two input channels can then be either fused after the first convolution layer or handled separately by two branches and fused at the bottom layer of the fully CNN. It turned out that the fusion of the information is the key part in the multi-organ segmentation using CNNs and that the bottom layer fusion extracts high-level features to combine important image information. The influence of noise is not propagated and therefore the overall segmentation accuracy is superior compared to the two other strategies.

3.2 Context-Sensitive CT Image Formation

3.2.1 Tissue-Related Weights

As discussed in the previous section, the automatic segmentation labels the CT data into different organs and tissues. Each voxel $\mathbf{r} = (x, y, z)$ in the target CT data set is assigned one tissue label l of a total of L tissue labels and the data set is uniquely characterized. Given the tissue labels, the volume can be subdivided into a set of disjoint binary masks $M = \{m_1(\mathbf{r}), m_2(\mathbf{r}), \dots, m_L(\mathbf{r})\}$. Furthermore, the tissue labels allow for an organ-specific parameter adaptation during image formation, display or analysis. The initial organ or tissue classification is non-overlapping forming completely disjoint sets where each voxel is exactly assigned to one label. In the transition zones between two adjacent subsets, the behavior in the transition between adjacent masks is not well-defined. Therefore, smooth tissue-related weighting coefficients $w_l(\mathbf{r})$ for each label l need to be determined from the binary segmented masks. Within the emerging transition zone of adjacent organs, the voxel is no longer exactly assigned to one specific anatomical structure but rather belonging to every adjacent organ. They can be interpreted as anatomical hybrid voxels similar to a prior probability of a voxel belonging to a certain anatomical region. The weight $w_l(\mathbf{r})$ of one specific tissue label l at voxel position \mathbf{r} is defined as

$$w_l(\mathbf{r}) \in \begin{cases} \{1\} & \text{if } \mathbf{r} \text{ belongs to a specific tissue class } l, \\ (0, 1) & \text{if } \mathbf{r} \text{ belongs to the transition area,} \\ \{0\} & \text{elsewhere.} \end{cases} \quad (3.1)$$

An artificial transition zone width d is introduced which determines the width of the smooth transition zone between neighboring regions. The width of the transition zone can depend on the initial segmentation accuracy, the organ type or the similarity between adjacent tissue classes and can therefore be selected organ-dependently. The tissue-related weights are derived from the Euclidean distance transform D (Felzenszwalb and Huttenlocher, 2012) of the binary labeled organ or tissue masks $m_l(\mathbf{r})$. The transformation $D(\mathbf{r}, l)$ associates the distance to the nearest point in the mask $m_l(\mathbf{r})$ to each voxel \mathbf{r} in the volume. The calculated distance field is then truncated as follows

$$D_{\text{trunc}}(\mathbf{r}, l) = \begin{cases} d & \text{if } D(\mathbf{r}, l) > d, \\ D(\mathbf{r}, l) & \text{otherwise.} \end{cases} \quad (3.2)$$

The transformed values are cropped and set to d if the Euclidean distance is higher than the transition zone width. By performing an inverse scaling followed by a normalization ensures $\sum_{l=1}^L w_l(\mathbf{r}) = 1$, yielding a convex combination of the set of the tissue-related weights. The final tissue-related weight for each voxel \mathbf{r} and label l yields

$$w_l(\mathbf{r}) = \frac{(d - D_{\text{trunc}}(\mathbf{r}, l))}{\sum_{l=1}^L (d - D_{\text{trunc}}(\mathbf{r}, l))}. \quad (3.3)$$

Since each voxel \mathbf{r} is initially assigned to exactly one label, the sum $\sum_{l=1}^L (d - D_{\text{trunc}}(\mathbf{r}, l))/d$ is greater than zero for each voxel position.

3.2.2 Context-Sensitive Resolution

As discussed in the last paragraph of Section 2.2, in analytic reconstruction there is always a trade-off between competing image properties, like image noise and spatial resolution. In order to provide an image that combines certain image properties one can focus on iterative reconstruction methods. However, these reconstructions are computational complex and therefore in clinical practice radiologists often rely on fast analytical reconstructions based on the filtered backprojection. A method that is able to combine initially mutually exclusive CT image properties into a context-sensitive (CS) image will be presented in the following. In order to increase the spatial resolution for specific anatomical structures while keeping the global noise level at a minimum, a blending of different organ-dependent basis images is performed. The resulting CS image is able to combine a high spatial resolution in the bone or lung with a low noise level in soft tissue areas. Depending on the voxel labeling, a basis image $f_b(\mathbf{r})$ most suitable for the corresponding anatomical structure or clinical indication is selected from a set of B pre-reconstructed basis images. The set of basis images often represents an image sequence of various resolution levels. The basis images might either be reconstructed with different reconstruction methods, e.g. iteratively or analytically, thereby the latter reconstructions might result from analytic reconstruction with varying kernels. Each of these kernels emphasizes different image properties depending on the applied apodization and the reconstruction results in images with desired competing properties (Hofmann et al., 2014; Lebedev et al., 2017; Dorn et al., 2018c). Moreover, the images might result from a single or a DECT scan as well as from a monoenergetic reconstruction from dual energy data. In general, there are no limitations on the selection of possible basis images. Moreover, it is also conceivable to use a clinical reconstruction implementation, for instance the weighted filtered backprojection (wFBP) (Stierstorfer et al., 2004) that is implemented in the scanner-specific reconstruction pipeline of Siemens.

The context-sensitive (CS) image with organ-adapted resolution levels is given by the linear blending as follows

$$f_{\text{CSR}}(\mathbf{r}) = \sum_{l=1}^L \sum_{b=1}^B w_l(\mathbf{r}) \cdot \delta_{l,b}(\mathbf{r}) \cdot f_b(\mathbf{r}), \quad (3.4)$$

with $w_l(\mathbf{r})$ being the tissue-related weight and $\delta_{l,b}$ being the Kronecker delta function. It describes the assignment of the label l to the basis image $f_b(\mathbf{r})$. The tissue-related

weight also helps to achieve a smooth blending of anatomical structures with varying resolution levels. In principle, the same basis images might be assigned to different tissue labels. For instance, a sharp basis image $f_{\text{sharp}}(\mathbf{r})$ is assigned to the tissue classes lung as well as bone. Thus, the same basis image may be used for the reconstruction of more than one anatomical structure. The basis image $f_b(\mathbf{r})$ contributes if and only if it is assigned to the label l meaning that the weight is greater than 0. A weighted mean of the contributing basis images is calculated within the overlapping transition zones. The result is a compound image altering the spatial resolution and noise level depending on the depicted tissue type or organ.

3.2.3 Context-Sensitive Image Display

The dynamic range of possible gray scale values in a CT image is greater than what can be displayed on an 8-bit or 10-bit clinical workstation (Kimpe and Tuytschaever, 2007). Even in the case of a 12-bit quantization, a CT image renders up to 4096 different gray scale values representing nearly every shade of gray. However, the human visual system is restricted to distinguishes less than 100 shades of gray (Kalender, 2000). In order to optimize the image contrast for the human visual system, the CT images are windowed for display purposes. The “windowing” technique is widespread and used by default in clinical CT and describes a linear mapping of the CT values in order to narrow the dynamic range for displaying purposes. The linear mapping function is truncated and the shape of its characteristic curve is defined by two parameters, the center C and the width W of the applied window. For instance, a gray scale window with center $C = 200$ HU and width $W = 600$ HU maps every CT value between -100 HU and 500 HU linearly from black to white. The CT values below -100 HU are displayed as black and the CT values above 500 HU are displayed as white. This window setting in particular visualizes the relevant gray scale values of one specific anatomical region, in this case the heart, while irrelevant gray values are faded down. The windowing technique enables to emphasis specific anatomical region and is therefore of great importance for the diagnosis of specific anatomical regions. In clinical routine, radiologists need to preassign different windowing settings for typical anatomical regions by manually changing the window level settings, since most of the pathologies may only be evident in a specific window setting. In clinical practice, a CT data set must therefore be at least reviewed in three distinct window and level settings that are optimized for soft tissue, lung and bone (Mandell et al., 2018). In particular, the switching between different windows and image reviewing adds a critical time requirement to the diagnosis of urgent trauma cases. However, if the CT image would only be reviewed in one specific window level setting, incidental findings might be missed. In the following, a technique is presented that eliminates the need of the adjustment of the center and width of the window by combining different organ-specific window level settings in a novel context-sensitive manner.

Table 3.1: Window level settings, which are usually applied in clinical routine (Pomerantz et al., 2000; Sutton et al., 2002). These window level settings are therefore assigned to the labeled anatomical structures and used in the organ-adaptive windowing.

Anatomy	Window Settings	
	Center C	Width W
Liver	40 HU	200 HU
Heart	200 HU	600 HU
Abdomen	30 HU	400 HU
Mediastinum	50 HU	350 HU
Angiography	100 HU	900 HU
Body	30 HU	400 HU
Body II	60 HU	400 HU
Bone I	450 HU	1500 HU
Bone II	300 HU	2000 HU
Lung I	-600 HU	1200 HU
Lung II	-600 HU	1600 HU
Lung III	-400 HU	1400 HU

Organ-Adaptive Window Blending

One window level parameter pair (C_l, W_l) is assigned to each anatomical region with label l . This specific parameter selection represents common settings that are used in clinical routine. The values might be preset to commonly used parameter settings, where a selection of typical window level settings for different anatomical regions is listed in Table 3.1. In order to calculate a consistent windowing over the whole patient without any inconsistencies, the discrete center and width values needs to be converted to organ-dependent continuous window parameter pairs. The above mentioned tissue-related weights $w_l(\mathbf{r})$ are reused to integrate a soft blending between neighboring discrete center and widths. The width of the blending diameter is determined by the parameter d in the weight calculation. It establishes artificial areas, where the center and the width slightly merge from one window to another. The organ-adaptive center and width parameters for each organ and each voxel are given by

$$C_{\text{adaptive}}(\mathbf{r}) = \sum_{l=1}^L w_l(\mathbf{r}) \cdot C_l, \quad \forall \mathbf{r} \quad (3.5)$$

$$W_{\text{adaptive}}(\mathbf{r}) = \sum_{l=1}^L w_l(\mathbf{r}) \cdot W_l, \quad \forall \mathbf{r}. \quad (3.6)$$

The assignment of the center C_l and width W_l to a specific organ can be adapted dynamically on demand. Within the overlapping blending areas, a smooth transition between adjacent window level settings emerges to improve the visual image impression.

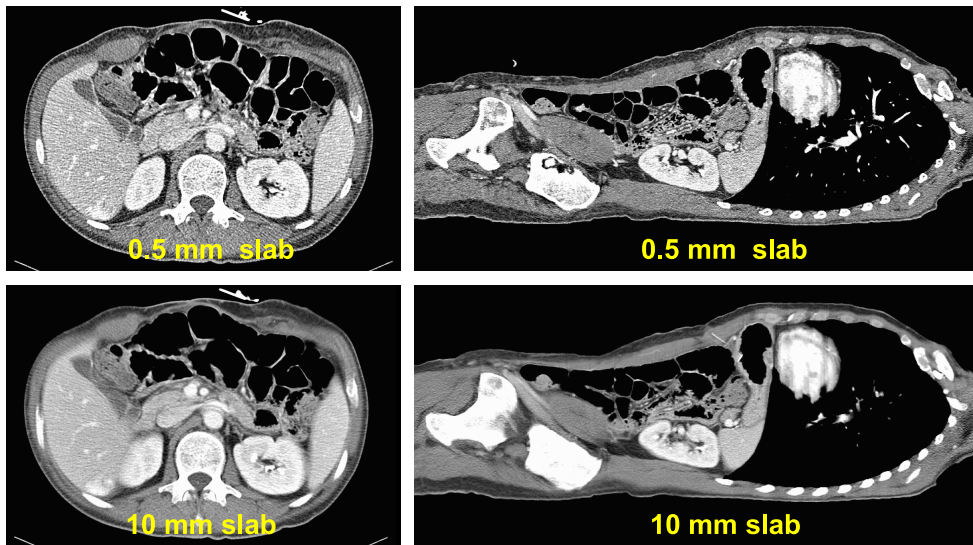


Figure 3.1: Sliding thin slab (STS) display with mean intensity projection (Mean-IP) over 0.5 mm compared to an STS Mean-IP over 10 mm. Viewing the image in thicker slices reduces the noise in the image. It is always preferred to perform the reconstruction with a thin slice thickness and to display the image in thick slices.

Organ-Adaptive Sliding Thin Slab

The context-sensitive image display also applies an adaptive sliding thin slab (STS) display technique. With STS, the CT data are no longer displayed as one entire volume but rather as slabs of sections that move through the volume of the data set (Napel et al., 1993; Ertl-Wagner et al., 2006; von Falck et al., 2010). Whenever possible, the CT volumes are to be reconstructed with the smallest possible slice thickness in order to obtain an isotropic spatial resolution to facilitate a multi planar reformation in arbitrary directions. However, an isotropic spatial resolution results in a high noise level that can be reduced by viewing the CT image in thicker “slabs” (compare Figure 3.1). Multiple subsequent images are combined, i.e. by averaging adjacent parallel slices along different viewing directions \mathbf{d} (Ertl-Wagner et al., 2006). In this case, the image noise is significantly reduced. An STS-mean intensity projection (Mean-IP) along an arbitrary direction \mathbf{d} is defined as

$$f_{\text{STS}}(\mathbf{r}) = \int ds f(\mathbf{r} + s\mathbf{d}) p(s), \quad (3.7)$$

where s is the slab thickness and $p(s)$ is the slab profile. This principle is now extended in a context-sensitive manner by selecting potentially different organ-adapted slab thicknesses s_l for each anatomical region l . The value can be altered depending on the anatomical region, and therefore piecewise organ-specific STS mean intensity projections are calculated depending on the region. The resulting image $f_{\text{STS adaptive}}$ is calculated as follows

$$f_{\text{STS adaptive}}(\mathbf{r}) = \frac{1}{\int ds p(s) w_l(\mathbf{r})} \int ds f(\mathbf{r} + s\mathbf{d}) p(s) w_l(\mathbf{r}), \quad (3.8)$$

where s_l denotes the slab thickness corresponding to the tissue label l . In addition, the parameter $w_l(\mathbf{r})$ represents again a tissue-related weighting coefficient. Furthermore, the mean calculation can be substituted by retaining the maximum value (STS-maximum IP (MIP)) or alternatively the minimum value (STS-MinIP) along the slab direction depending on the organ or clinical indication, e.g. in the lung. For each anatomical region, there are therefore two degrees of freedom: firstly, the choice of a reasonable slab thickness and secondly, the selection of a reasonable STS technique.

3.3 Context-Sensitive Dual Energy

In Section 2.4, common dual energy technologies and their applications have been listed and described in more detail. These applications are supplied as standard with the dual energy system and bear the potential to provide a multitude of statements about the tissue type, material composition or blood flow to the radiologist. Each of these approved applications performs the DECT evaluation organ-specifically (VNC, iodine overlays, gout, liver, kidney stone differentiation, perfused blood flow in the lung or heart, bone marrow, etc.) and only works reliable with an organ-adapted calibration, i.e. the calibration parameters need to be adjusted to the organ-of-interest. A selection of the output of commercially available applications on Siemens CT evaluation workstations is shown in Figure 3.2. Nevertheless, results from the algorithms are generally shown for the entire image, creating in some cases misleading results. Furthermore, the dual energy evaluation is performed and displayed on the entire data set and needs to be invoked by the user since no anatomical prior knowledge is taken into account. The following analysis will exemplarily focus on the applications that are commercially available in the *Siemens Syngo.CT Dual Energy* software. Similar algorithms are implemented and adapted referring to both principles that might also underly the Siemens applications, i.e. material decomposition and material classification.

3.3.1 Liver Virtual Non-Contrast (LiverVNC)

The following section discusses a material decomposition that will be denoted as *LiverVNC* algorithm in the following referring to the Siemens application. It is a three material decomposition that is based on a local coordinate transform from the dual energy space to a target VNC-iodine space as shown in Figure 3.3. The method is used to virtually remove the iodine content from the contrast-enhanced scan in order to imitate a native scan. Virtual non-contrast (VNC) imaging is an image based method that decomposes the dual energy data into a water equivalent VNC image and an iodine overlay. Since the slope towards pure iodine points to infinity in the DE space, the three material decomposition is interpreted as a coordinate transform from the DE space into a VNC-iodine space using a parallel projection of each point onto a base line, the VNC line. The third material is virtually removed from the image. In the sense of a three material decomposition with three known basis materials, the basis material triangle degenerates and the edge fat-iodine and blood-iodine will become almost parallel. The geometric interpretation and an alternative strategy to solve for the three basis material components will be discussed later on in Section 3.4.1. In order to decompose the dual

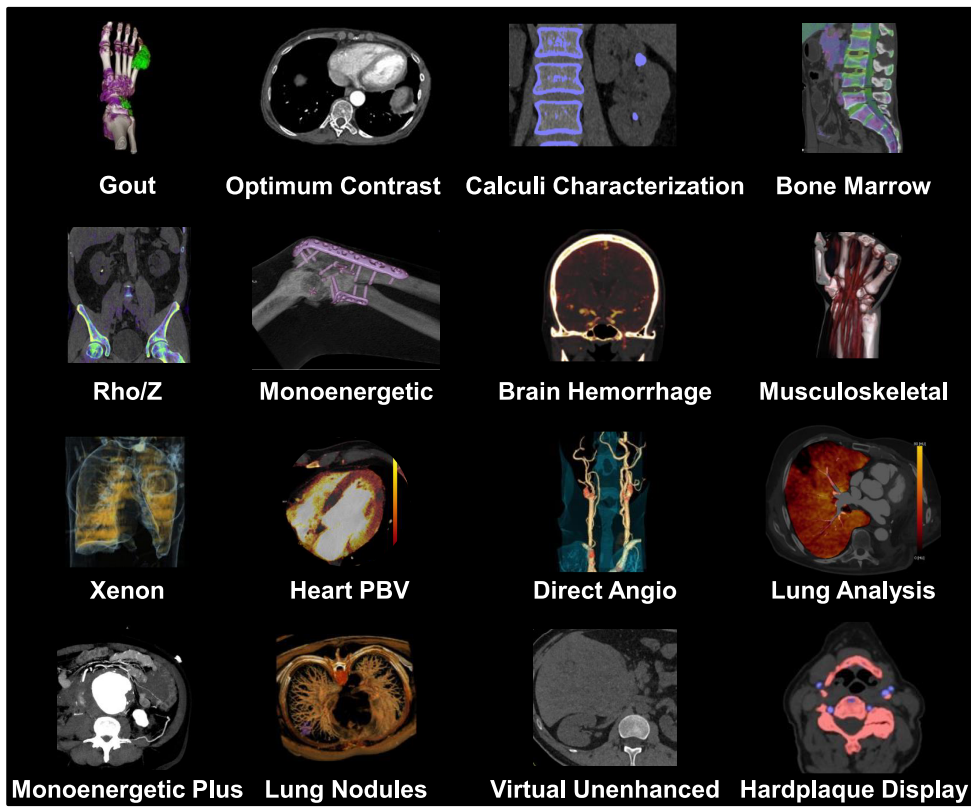


Figure 3.2: Syngo.CT Dual Energy application examples. Virtual unenhanced contains liver VNC, lung analysis contains lung PBV. Courtesy of Siemens Healthineers, Forchheim, Germany.

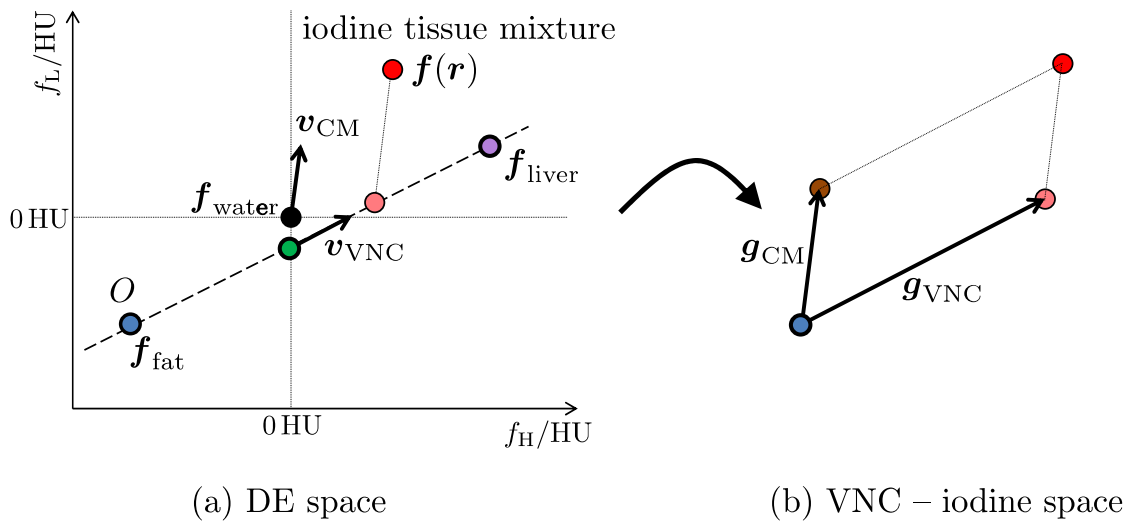


Figure 3.3: Coordinate transform in the dual energy from the DE space (a) to the target VNC-iodine space (b) in the Liver VNC application.

energy data into an iodine map and a VNC image, the following coordinate transformation is applied. The origin of the VNC-iodine space O is located in the fat point

$$O = \mathbf{f}_{\text{fat}} = \begin{pmatrix} f_{\text{H,fat}} \\ f_{\text{L,fat}} \end{pmatrix}. \quad (3.9)$$

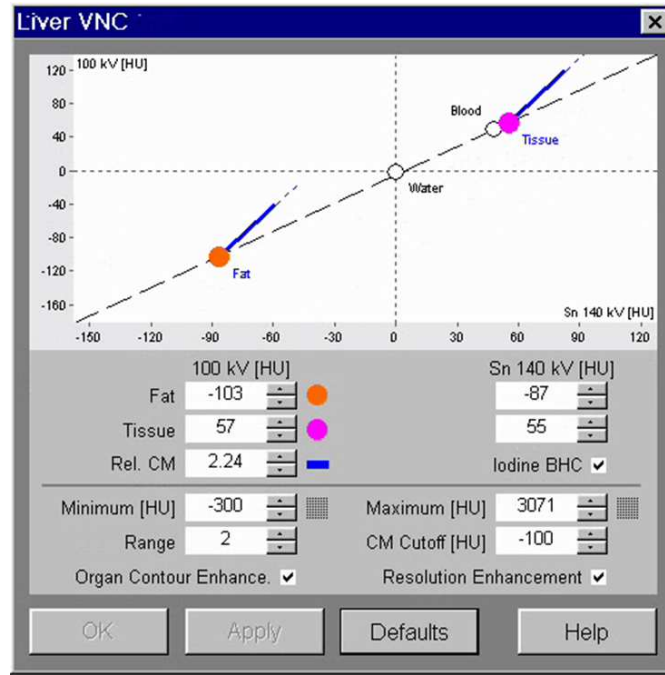


Figure 3.4: Screenshot of the organ-specific initialization in the *LiverVNC* applications.

First, two linearly independent base vectors are defined that span the novel VNC–iodine coordinate system in the dual energy space. The first vector points towards pure iodine

$$\mathbf{v}_{\text{CM}} = \begin{pmatrix} f_{\text{H,iodine}} - f_{\text{H,liver}} \\ f_{\text{L,iodine}} - f_{\text{L,liver}} \end{pmatrix} \propto \begin{pmatrix} 1 \\ R \end{pmatrix} \quad (3.10)$$

and the second vector defines the slope of the base line (connection between fat and liver point)

$$\mathbf{v}_{\text{VNC}} = \begin{pmatrix} f_{\text{H,liver}} - f_{\text{H,fat}} \\ f_{\text{L,liver}} - f_{\text{L,fat}} \end{pmatrix}. \quad (3.11)$$

The entries of the base vectors are calibrated either by the evaluation of regions of interest (ROIs) in corresponding anatomical structures in the low and in the high energy image, in particular in fat and liver tissue, or by preset values in the Siemens software. The quantities depend on the tube voltage combination and one example initialization of the algorithm parameters is illustrated in Figure 3.4. The basis can now be changed and expressed by the polychromatic initial images f_{L} and f_{H} as linear combination

$$\begin{pmatrix} f_{\text{H}}(\mathbf{r}) \\ f_{\text{L}}(\mathbf{r}) \end{pmatrix} = \begin{pmatrix} f_{\text{H, fat}} \\ f_{\text{L, fat}} \end{pmatrix} + f_{\text{VNC}}(\mathbf{r})\mathbf{v}_{\text{VNC}} + f_{\text{CM}}(\mathbf{r})\mathbf{v}_{\text{CM}} \quad (3.12)$$

$$= \begin{pmatrix} f_{\text{H, fat}} \\ f_{\text{L, fat}} \end{pmatrix} + \begin{pmatrix} \mathbf{v}_{\text{VNC}} & \mathbf{v}_{\text{CM}} \end{pmatrix} \cdot \begin{pmatrix} f_{\text{VNC}}(\mathbf{r}) \\ f_{\text{CM}}(\mathbf{r}) \end{pmatrix}. \quad (3.13)$$

3.3. CONTEXT-SENSITIVE DUAL ENERGY

Table 3.2: Organ-adapted calibration of the *LiverVNC* application. By changing the slope of the base line the algorithm can be applied to quantify the iodine content in various anatomical regions.

Anatomy	Slope of the base line determined by	
	basis material I	basis material II
Liver iodine quantification	fat	soft tissue
Soft tissue iodine quantification	air	water
Lung perfused blood volume	air	soft tissue
Heart perfused blood volume	fat	soft tissue
Bone Marrow analysis	yellow marrow (fat)	red marrow (soft tissue)
Brain Hemorrhage	blood	cerebrospinal fluid (CSF)

In order to solve for the distances f_{VNC} and f_{CM} , the linear system of equations is inverted

$$\begin{pmatrix} f_{\text{VNC}}(\mathbf{r}) \\ f_{\text{CM}}(\mathbf{r}) \end{pmatrix} = \frac{1}{v_{\text{VNC}_x} v_{\text{CM}_y} - v_{\text{CM}_x} v_{\text{VNC}_y}} \begin{pmatrix} v_{\text{CM}_y} - v_{\text{CM}_x} \\ -v_{\text{VNC}_y} v_{\text{VNC}_x} \end{pmatrix} \cdot \begin{pmatrix} f_{\text{H}}(\mathbf{r}) - f_{\text{H, fat}} \\ f_{\text{L}}(\mathbf{r}) - f_{\text{L, fat}} \end{pmatrix} \quad (3.14)$$

The VNC is somewhere located on the fat-liver-line. The calculation of the VNC vector and the iodine contrast map vector of each voxel in the novel coordinate system is straightforward

$$\mathbf{g}_{\text{VNC}} = \mathbf{f}_{\text{fat}}(\mathbf{r}) + \mathbf{v}_{\text{VNC}} \cdot f_{\text{VNC}}(\mathbf{r}) \quad (3.15)$$

$$\mathbf{g}_{\text{CM}} = \mathbf{v}_{\text{CM}} \cdot f_{\text{CM}}(\mathbf{r}). \quad (3.16)$$

The final VNC image and the final iodine contrast map that are displayed are given as weighted average of both components as

$$\text{VNC}(\mathbf{r}) = (w \quad 1 - w) \cdot \mathbf{g}_{\text{VNC}} \quad (3.17)$$

$$\text{CM}(\mathbf{r}) = (w \quad 1 - w) \cdot \mathbf{g}_{\text{CM}} \quad (3.18)$$

with w chosen such that the image noise is minimized. By changing the points of the VNC line and therefore adjusting the slope of the base line to different anatomical regions, the algorithm is also applied to quantify the iodine content in the abdomen, lung and heart. Furthermore, the method is not only used to virtually remove the iodine content of the image, it can also be applied to virtually remove the calcium content to provide a bone marrow analysis that indicates bone bruising. As mentioned in the beginning of Section 3.3, the different selection of the basis points is necessary for the application of the algorithm to varying anatomical regions. Typical calibrations are listed in Table 3.2.

The *LiverVNC* application might result in deceptive color codings in surrounding structure of the organ of interest. Since the above used organ-related calibration of the base line is perfectly adapted for the iodine quantification in the liver, the iodine quantification outside might be incorrect. Each voxel that is not exactly a linear combination of fat and soft tissue will potentially be represented either by a negative or by a positive

iodine uptake. In some cases, e.g. for bones or calcifications, the erroneously colored iodine uptake can be significant. Similar limitations are also present with air and water as basis materials. This calibration would work only for the iodine quantification in soft tissue.

3.3.2 Organ-Specific DE Evaluation and Analysis

Each of these above mentioned DE applications suffers from the lack of prior anatomical information, performs the dual energy evaluation on the entire data set and needs to be invoked by the user. By using prior anatomical information, the numerous DECT applications are combined into one single tool. Based on the context-sensitive information by means of the tissue-related weights, the tools can be chosen and applied to the different organs automatically. Instead of having one single manually selected dual energy application, the prior-based dual energy evaluation scheme performs all organ-specific feasible methods at once. This CS analysis allows to simultaneously evaluate multiple organs and to show organ-specific dual energy overlays or tissue classification information wherever appropriate. The method can readily be generalized for other vendors' applications.

3.3.3 Patient-Specific Parameter Calibration

Besides the slope of the base line, which is determined by two calibration points in the DE space (fat point and liver point in Figure 3.3), the slope towards pure iodine needs to be calibrated. In commercial software, these points as well as the slope are calibrated and preset by the vendor. However, due to the non-linearity of beam hardening and scatter, which highly depends on the patients cross-section, the default settings of the slope towards iodine in particular might not be optimal and this may result in an under- or overestimation of the true iodine concentration. A phantom measurement has been performed to show the deviation of the true to measured iodine concentrations. The results will be presented in the corresponding section 4.2.2. In order to obtain a reliable DE analysis, each of the mentioned applications benefits from a patient-specific calibration. The calibration parameters, i.e. the basis material points in the DE space and iodine slope, may be determined by user-defined ROIs. Using the available prior anatomical information, the ROIs that are required for a patient-specific calibration of the algorithms can now be placed automatically into the corresponding anatomical region. In this work, the relative contrast media ratio, which defines the slope in the dual energy (DE) diagram, has to be adjusted individually for each patient by means of a calibration.

Relative Contrast Media Ratio (RelCM)

In clinical CT, iodine itself only appears in a solution and therefore the true CT value of pure iodine cannot be assessed. Simulations point out that the CT value of pure iodine is 127,890 HU \approx 128 kHU, if measured at 70 keV monochromatic. In clinical applications the relative contrast media ratio (RelCM) pointing towards pure iodine is used. It is defined as the ratio between the CT value of iodine in the low energy image and the CT value of iodine in the high energy image (Krauss et al., 2015). In a practical manner, it is determined by the differences of the mean values of two ROIs placed within regions of different iodine concentrations acquired at both energy levels, i.e.

$$R = \frac{CT_1(E_L) - CT_2(E_L)}{CT_1(E_H) - CT_2(E_H)}, \quad (3.19)$$

where $CT_1(E)$ and $CT_2(E)$ are given by the measurement of the mean CT value in the corresponding ROIs 1 and 2 at both energy levels E_L and E_H . In general, the ROI is indexed by i . By incorporating an unknown mixing ratio m_i of water and iodine in a ROI i , the measured CT value within this ROI is given by the linear combination of its pure mixing components

$$CT_i(E) = (1 - m_i)CT_W(E) + m_iCT_I(E). \quad (3.20)$$

Inserting the above Equation (3.20) into Equation (3.19), it turns out that the unknown mixing ratios cancel out

$$R = \frac{CT_I(E_L) - CT_W(E_L)}{CT_I(E_H) - CT_W(E_H)} = \frac{CT_I(E_L)}{CT_I(E_H)} = \frac{\mu_{I,L} - \mu_{W,L}}{\mu_{I,H} - \mu_{W,H}} = \frac{\mu_{I,L} - 1}{\mu_{I,H} - 1}. \quad (3.21)$$

Because the CT value of water is zero by calibration, $CT_W(E)$ disappears from the calculation. The next step includes the conversion of the CT values to attenuation values. By assuming that the values stored in the image are scaled such that $\mu_W = 1$, the relation between the relative contrast media ratio and the measurements in two ROIs is given. This last convention will be used in the following considerations. Apart from $R > 1$, which is true for iodine or other hyper-dense materials, please note that

$$R - 1 = \frac{\mu_{I,L} - \mu_{I,H}}{\mu_{I,H} - 1}, \quad (3.22)$$

$$1 - \frac{1}{R} = \frac{\mu_{I,L} - \mu_{I,H}}{\mu_{I,L} - 1}. \quad (3.23)$$

Krauss et al. (2015) state that the ratio typically ranges between 1.85 and 3.46 for different tube voltage combinations and patient sizes and yields a measure of the spectral separation. The higher the RelCM, the better the spectral separation. In order to provide an impression, typical default values of the parameter for different scanner types and tube voltage combinations are listed in Table 3.3.

In the following paragraph, the role of the relative contrast ratio R in the decomposition of the low energy image f_L and the high energy image f_H into a virtual non-contrast or water image f_W and an iodine overlay f_I is demonstrated. For these considerations,

Table 3.3: Typical default RelCM values for different scanners and tube voltage combinations. The higher the relative iodine ratio, the better the spectral separation.

Scanner	Syngo.Via Dual Energy Settings	
	Tube voltage combination	Relative iodine ratio
SOMATOM Definition Flash	80 kV/140 kV + 0.4 mm Sn	3.01
SOMATOM Definition Flash	100 kV/140 kV + 0.4 mm Sn	2.24
SOMATOM Definition Force	70 kV/150 kV + 0.6 mm Sn	4.13
SOMATOM Definition Force	80 kV/150 kV + 0.6 mm Sn	3.46
SOMATOM Definition Force	90 kV/150 kV + 0.6 mm Sn	3.01
SOMATOM Definition Force	100 kV/150 kV + 0.6 mm Sn	2.64

the initial images are calibrated such that air has a value of 0 and water has a value of 1. To obtain f_W and f_I from two measurements f_L and f_H , the mean values $\mu_{W,L}$ and $\mu_{W,H}$ of a water region of interest (ROI) and the mean values $\mu_{I,L}$ and $\mu_{I,H}$ of an iodine ROI are utilized. Both ROIs are measured in the low and in the high energy images and used to find linear combinations such that

$$1 = c_{W,L}\mu_{W,L} + c_{W,H}\mu_{W,H} \quad (3.24)$$

$$1 = c_{W,L}\mu_{I,L} + c_{W,H}\mu_{I,H} \quad (3.25)$$

for the water image (VNC image) and

$$0 = c_{I,L}\mu_{W,L} + c_{I,H}\mu_{W,H} \quad (3.26)$$

$$\gamma = c_{I,L}\mu_{I,L} + c_{I,H}\mu_{I,H} \quad (3.27)$$

for the iodine image with γ being the value that corresponds to the concentration of iodine. Exploiting the assumption that $\mu_{W,L} = \mu_{W,H} = 1$, it turns out that

$$c_{W,L} = 1 - c_{W,H} = \frac{1 - \mu_{I,H}}{\mu_{I,L} - \mu_{I,H}} = \frac{1}{1 - R} \quad (3.28)$$

$$c_{I,L} = -c_{I,H} = \frac{\gamma}{\mu_{I,L} - \mu_{I,H}}. \quad (3.29)$$

The sum $f_W + f_I$ then yields

$$f_W + f_I = (c_{W,L} + c_{I,L})f_L + (c_{W,L} + c_{I,L})f_H \quad (3.30)$$

$$= \frac{\gamma + 1 - \mu_{I,H}}{\mu_{I,L} - \mu_{I,H}}f_L + \frac{\gamma + 1 - \mu_{I,L}}{\mu_{I,L} - \mu_{I,H}}f_H. \quad (3.31)$$

The choice

$$\gamma = \frac{1}{2}(\mu_{I,L} + \mu_{I,H}) - 1. \quad (3.32)$$

results in the following relationship

$$f_W + f_I = \frac{1}{2}(f_L + f_H). \quad (3.33)$$

This specific choice of scaling the sum of the VNC image and the iodine image results

in the mixed image, i.e. the average of the low and the high energy scan. In general, the mixed image is

$$f_\alpha = (1 - \alpha)f_L + \alpha f_H, \quad (3.34)$$

where α is the mixing weight and usually chosen to maximize the CNR. Then

$$\gamma = \alpha(\mu_{I,H} - \mu_{I,L}) + \mu_{I,L} - 1 \quad (3.35)$$

is the appropriate choice that ensures $f_W + f_I = f_\alpha$, if one desires to fulfill that identity.

3.4 Quantitative Pseudo Multi Material Decomposition

The task of material decomposition is challenging, as organs in the human body might be a composite of numerous materials e.g. blood, fat, water, air, bone and contrast media. Although multi energy CT achieves promising material decompositions into two, three, or more materials, this technology is not yet prevalent in the clinical routine. Therefore, it is of great importance to decompose the dual energy data into more than three material constituents. For instance, the quantification of fat content in the liver requires the decomposition into four basis material components: liver tissue, fat, blood and contrast media (CM) (Mendonça et al., 2014; Hyodo et al., 2017). Another possible application is the analysis and quantification of different material components in tumors for tumor staging or treatment monitoring. Some material components might be indicators for inflammations or healing and could be correlated with the current treatment progression. Moreover, in particular in the field of radiotherapy, it might be interesting to obtain an accurate map of the material distributions besides bone and soft tissue, such as calcium, metal, e.g. implants, gold etc. and contrast agents based on iodine (Long and Fessler, 2014). In the following section, material decomposition methods in image domain will be discussed. Followed by a short review of state-of-the-art multi material decompositions in image domain, the quantitative pseudo multi material decomposition that has been developed in this work will be presented.

3.4.1 Material Decomposition in Image Domain

For each DE image pair $\mathbf{f}(\mathbf{r}) = (f_L(\mathbf{r}), f_H(\mathbf{r}))$, there exist two basis material images $f_1(\mathbf{r})$ and $f_2(\mathbf{r})$. The decomposition of dual energy data in image domain is given by the inversion of the linear system of equations

$$\begin{pmatrix} f_L(\mathbf{r}) \\ f_H(\mathbf{r}) \end{pmatrix} = \begin{pmatrix} \psi_{L,1} & \psi_{L,2} \\ \psi_{H,1} & \psi_{H,2} \end{pmatrix} \cdot \begin{pmatrix} f_1(\mathbf{r}) \\ f_2(\mathbf{r}) \end{pmatrix}, \quad (3.36)$$

with $\boldsymbol{\psi}_i = (\psi_{L,i}, \psi_{H,i})$, $i \in \{1, 2\}$ being the basis material vectors. The corresponding basis material vectors contain typical attenuation values of the pure or compound materials to be decomposed into and need to be calibrated beforehand. The calibration is done either by simulation or from ROIs which are placed in corresponding anatomical structures in the DE patient data itself. A geometric interpretation of the two material decomposition is illustrated in Figure 3.5 (a). The DE data point is decomposed into its

two basis materials CM and blood. The voxel can be interpreted as linear combination of the two basis material vector.

As discussed in Section 2.3.2, an additional constraint on the material mixtures is necessary to enable the decomposition of dual energy data into more than two basis material components. By assuming that the mixture is volume preserving, the material composition fulfills the ideal solution constraint

$$\sum_{i=1}^M f_i(\mathbf{r}) = 1 \quad (3.37)$$

where $f_i(\mathbf{r})$ with $f_i(\mathbf{r}) \geq 0 \forall i$ being the volume fractions of each constituent material $i \in \{1, \dots, M\}$. In order to decompose the DE data into $M = 3$ basis materials, it is assumed that each voxel consists of at most three material constituents and is therefore a compound of three basis materials that are known a priori. Three material decomposition assuming volume preservation is given as follows

$$\begin{pmatrix} f_L(\mathbf{r}) \\ f_H(\mathbf{r}) \\ 1 \end{pmatrix} = \begin{pmatrix} \psi_{L,1} & \psi_{L,2} & \psi_{L,3} \\ \psi_{H,1} & \psi_{H,2} & \psi_{H,3} \\ 1 & 1 & 1 \end{pmatrix} \cdot \begin{pmatrix} f_1(\mathbf{r}) \\ f_2(\mathbf{r}) \\ f_3(\mathbf{r}) \end{pmatrix} \quad (3.38)$$

subject to $f_i \geq 0$, $i = \{1, 2, 3\}$. The positivity constraint $0 \leq f_i \leq 1$ must be fulfilled for all volume fractions to provide physically reasonable results. As shown in Figure 3.5 (b), the three material decomposition can be interpreted as a triangle in the DE diagram. Each point that is located inside that triangle can exactly be decomposed into its basis material fractions. These fractions correspond to the Barycentric coordinates of a point in the triangle, which is spanned by the three basis material fractions.

3.4.2 Prior Image-based Multi Material Decomposition

Goodsitt et al. (1987) first demonstrated the feasibility of decomposing dual energy data into three basis material fractions by assuming that the components of the material mixture follow an ideal solution constraint (volume preservation as shown in Section 2.3.2). The authors decomposed the dual energy data into fat, soft tissue and bone in order to obtain a measure for the composition of trabecular bone. Liu et al. (2009) proved that there is no volume dilation or volume contraction in an ideal solution when the individual basis materials are mixed. Based on this fact, Mendonça et al. (2014) developed a relationship between mass and volume conservation. Under the assumption that iodine or other saline solutions are already diluted, the assumption on volume preservation provides a valid approximation of the mixing behavior in the human body. Therefore, most of the three material decompositions are based on these considerations. As mentioned previously in Section 3.3.1, the LiverVNC application is also an expression of a three material decomposition in image domain in which one basis material, i.e. one vertex of the triangle, is translated to infinity. Nonetheless, two problems arise in three material decompositions: first, the basis materials at the vertices of the triangle might not sufficiently represent the components of the mixture within the organ of interest. For instance, bone can mathematically be represented by fat, blood and iodine, but this

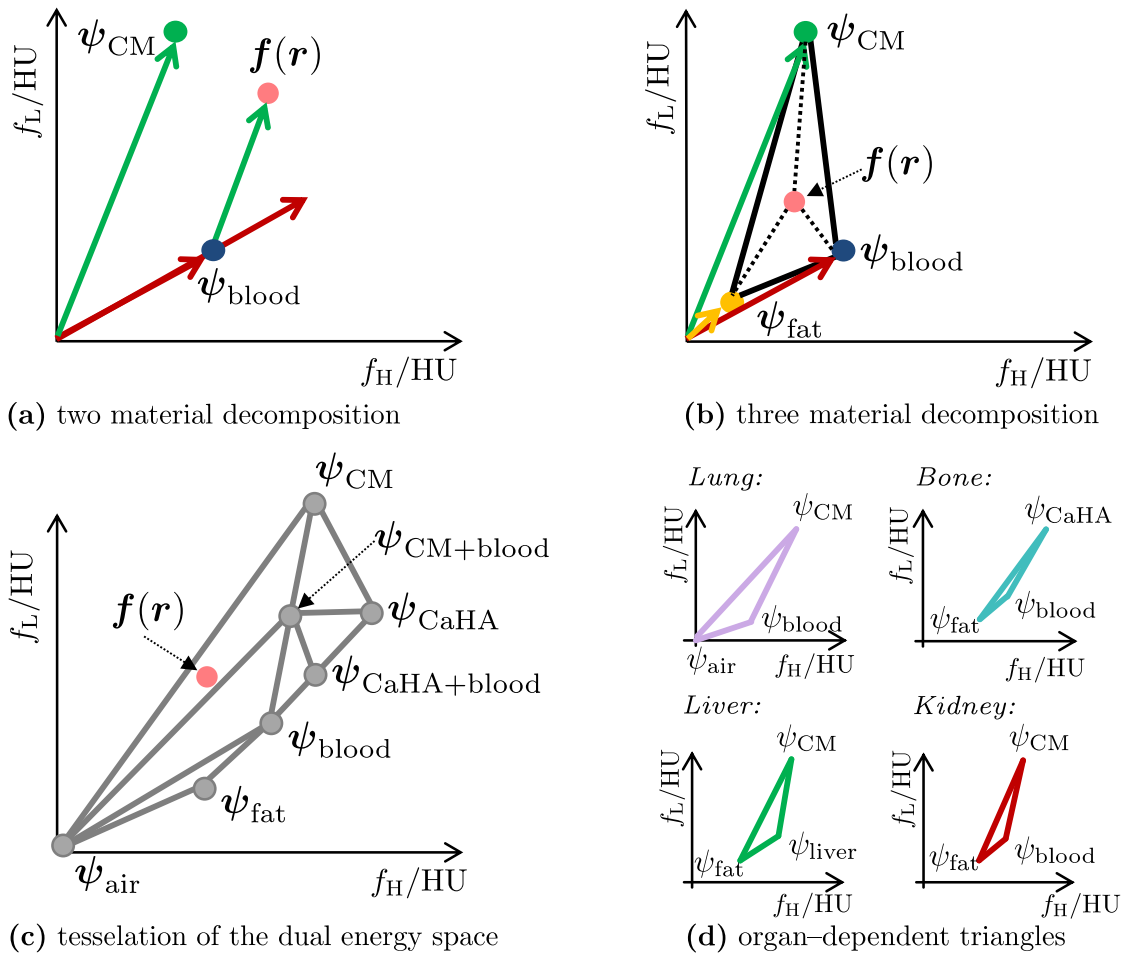


Figure 3.5: Geometric interpretation of the material decomposition in image domain. Each voxel (dual energy data pair) $\mathbf{f}(\mathbf{r}) = (f_H(\mathbf{r}), f_L(\mathbf{r}))$ can be decomposed into its two basis material fractions (a). By making an additional assumption on the mixing behavior, the voxel can also be decomposed into its three basis material fractions. These fractions correspond to the Barycentric coordinates of a triangle which is spanned by the three base materials (b). By using a tessellation of triangles that is constructed by a set of base materials, it is possible to decompose the voxel into more than three basis material fractions (c) according to Mendonça et al. (2014). However, this does not always result in physical appropriate material fractions. An organ-dependent selection of the basis materials results in overlapping triangles. Prior anatomical information is used to resolve the resulting ambiguities in an organ-specific manner (d).

representation may lack an appropriate physical interpretation. Secondly, due to noise, voxels may be located outside of the specific triangle although they would belong to the triangle. At least one of the obtained volume fractions may become negative and does not result in physically reasonable values, if the voxel is outside the triangle.

In order to decompose the DECT data into more than three basis materials, Mendonça et al. (2014) proposed a tessellation of the dual energy space with multiple triangles resulting in a possible decomposition into more than three basis materials. A schematic tessellation of the DE space is demonstrated in Figure 3.5 (c). Within the convex hull of the full tessellation, the three basis materials for the decomposition are exactly determined based on the location of the point in the DE space. However, due to noise

the voxel could fall into neighboring triangles, which does not represent the correct basis material triplets, leading to ambiguities in the decomposition. The erroneous assignment of voxels belonging to one specific triangle to a neighboring triangle with incorrect basis materials may result in mathematically correct volume fractions but material crosstalk of different basis materials in the material images. Long and Fessler (2014) reported material crosstalk between blood and fat especially in the heart region, where blood appears also in the fat image. Moreover, fat also appeared in the cortical bone image. Therefore, even if the resulting volume fractions fulfill the sum-to-one constraint in Equation (3.37) and are non-negative, wrong basis materials could have been used. In this specific case, the decomposition does not result in physiologically appropriate volume fractions. The major drawback of this method is therefore the isolated treatment of each voxel. Neither the information from adjacent voxels nor the location of the voxel within the volume is used.

3.4.3 Organ-Adaptive Multi Material Decomposition

In the work presented in this section, a pseudo multi material decomposition is developed that is based on anatomical prior information. The strategy of using organ priors for the selection and initialization of DECT material decompositions as discussed in Section 3.3.2 is transferred and extended to simultaneously calculate a multi material decomposition. The prior information is exploited to incorporate local neighborhood information and reduce crosstalk in the material images. The pseudo material decomposition consists of multiple organ-specific three material decompositions. The basis materials are adapted organ-specifically depending on the underlying organ labeling of the voxel to be decomposed. Basis material triplets are defined in advance to provide a set of possible three material decompositions. A triplet material library used in this work is listed in Table 3.4. Each of these basis material triplets forms an organ-dependent triangle in the DE space (see Figure 3.5 (d)). Since there is a multitude of three material decompositions to generate the multi material decomposition instead of performing a direct decomposition into multiple materials, the method is denoted as pseudo multi material decomposition.

The base material triplet is selected for the decomposition depending on the organ or tissue assignment. Hence, one base material triplet is exactly assigned to each voxel. The organ-dependent assignment that is also shown in Figure 3.6 (a) allows for potentially overlapping triangles in the DE space (Figure 3.6 (b)). For instance, the triangle that is assigned to soft tissue (highlighted in green) overlaps with the triangle that is assigned to bone (highlighted in orange). For the decomposition of the bone (“orange” triangle), it is assumed that no CM is diluted inside the bone and bone is an exact material composition of fat, blood and calcium hydroxyapatite (CaHA). Voxels that are located within the overlapping area might be decomposed using either of the two triangles. By exploiting the anatomical prior information, the ambiguity with respect to the voxel-organ assignment can be resolved and the voxel is decomposed using the correct basis material triplet. Instead of only considering the measured CT values at two different energies and therefore the location of the DE point in the DE space, the anatomical prior knowledge guides the decomposition process. Even if the voxel is assigned to one

Table 3.4: Triplet material library for the decomposition of dual energy data into its basis materials. The basis material selection is used for the quantitative pseudo multi material decomposition.

organ	Basis material library		
	material 1	material 2	material 3
lung	air	blood	contrast media (CM)
liver	fat	liver tissue	CM
bone	fat	blood	cortical bone
bone	fat	CM	cortical bone
muscles	fat	soft tissue	CM
fatty tissue	fat	blood	CM
vascular system	blood	CM	cortical bone
spleen, kidneys	fat	blood	CM
...

triangle, it may be located outside of the triangle based on local noise distributions in the CT images. If the voxel is located outside, the decomposition would not yield reasonable volume fractions. In order to cope with these voxels, they are projected onto the closest edge of the triangle (O’Donnell et al., 2017) prior to decomposition.

After the decomposition, the results of the multiple three material decompositions are rearranged to material-specific images. However, besides presenting more and more material images to the radiologist, the volume fractions of the material compound can be rescaled to organ-dependent material scores (fat content of liver, iodine content of liver, soft tissue content of liver, absolute or relative) that can be visualized via a reasonable visualization, e.g. pie charts, and later be correlated with different diagnoses.

Moreover, the volume fractions corresponding to the basis material CM can easily be converted to an iodine concentration. The location-dependent mass concentration of any material is given by

$$\gamma(\mathbf{r}) = \frac{m}{V} = f_{\text{basis}}(\mathbf{r}) \cdot \rho_{\text{basis}}. \quad (3.39)$$

The mass concentration of iodine in each voxel is therefore $\gamma_{\text{iodine}} = f_{\text{CM}}(\mathbf{r}) \cdot \rho_{\text{CM}}$ [mg/mL].

Considering the ideal solution constraint, instead of treating the contrast media as if it were pure iodine, its level of dilution prior to patient injection and its full chemical composition must be taken into account. The injection of iodinated contrast agent, e.g. Omnipaque 300, is a tangible example. This contrast medium is a saline solution which contains $\rho_{\text{CM}} = 300$ mg/mL of iohexol ($\text{C}_{19}\text{H}_{26}\text{I}_3\text{N}_3\text{O}_9$) (or 40.47% iohexol concentration). The mass fraction of iodine in iohexol itself is only 46.4% (Mendonça et al., 2014).

By evaluating small ROIs in the material image of CM, a quantitative measure of the average values of absolute iodine concentrations can be obtained. The value of the bone mineral density, i.e. the concentration of pure CaHA cannot be converted as easily, since the real concentration in the human body is not known exactly. The basis materials can be calibrated either by simulation or by patient-specific evaluations of calibration ROIs in the patient data set. In this work, the used basis materials are blood, contrast

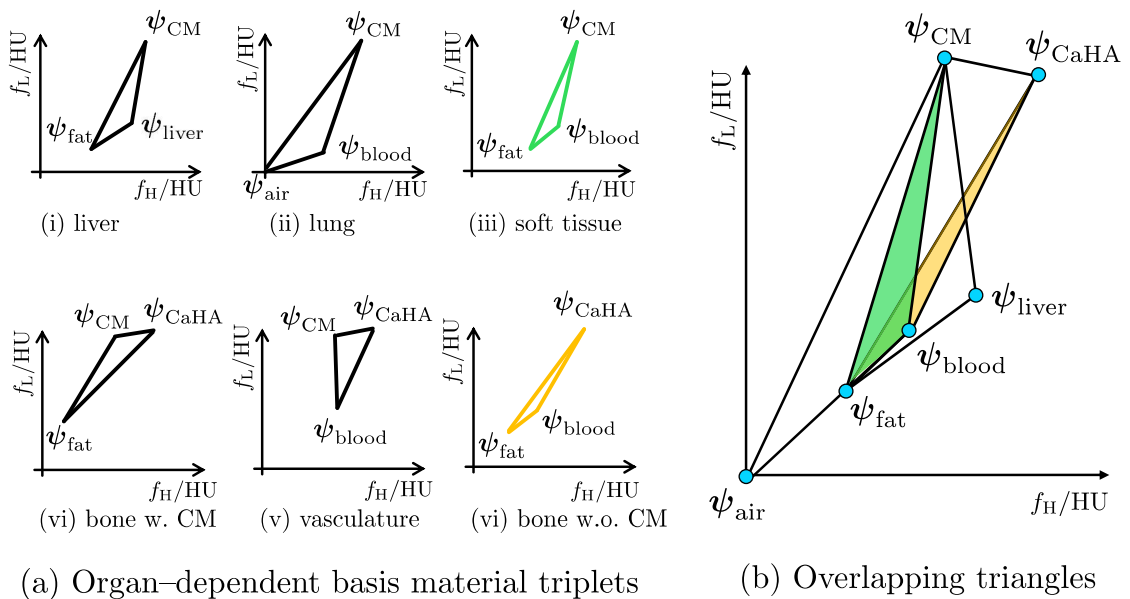


Figure 3.6: Overlapping triangles reduce material crosstalk during the decomposition. Each voxel is exactly assigned one basis material triplet from a basis material library (a). These triplets result in overlapping triangles in the DE space (b). In order to highlight example overlapping triangles, the soft tissue triangle is highlighted in green and the bone triangle is highlighted in orange. Without prior knowledge, the voxel might be assigned to both of the triangles based on the position in the dual energy diagram. The voxel can only be assigned correctly based on prior information.

media (Ultravist 370 - iodine contrast agent containing 370 mg iodine/mL), cortical bone (CaHA with 500 mg/mL), fat, soft tissue, liver tissue and air as tabulated in the literature (Cullen et al., 1990). The basis materials liver tissue, soft tissue and blood differ by their relative density during the simulation using the Evaluated Photon Data Library (EPDL97) (Cullen et al., 1997). Furthermore, mixtures of cortical bone with contrast media and contrast media with fat are also allowed, since in a clinical case the contrast media is also diluted into these anatomical structures. The triplet material library used in the carried out experiments (shown in Table 3.4) consists of seven varying base material combinations. If the basis material initialization is carried out using patient-specific calibrations, i.e. based on evaluations of ROIs in corresponding anatomical structures in a patient data set, the number of possible basis materials is reduced from seven to five. Using ROI evaluations in a contrast-enhanced scan, it is not possible to differentiate between blood, soft tissue and liver tissue. These basis materials are therefore pooled to one “soft tissue”.

CHAPTER 4

Results

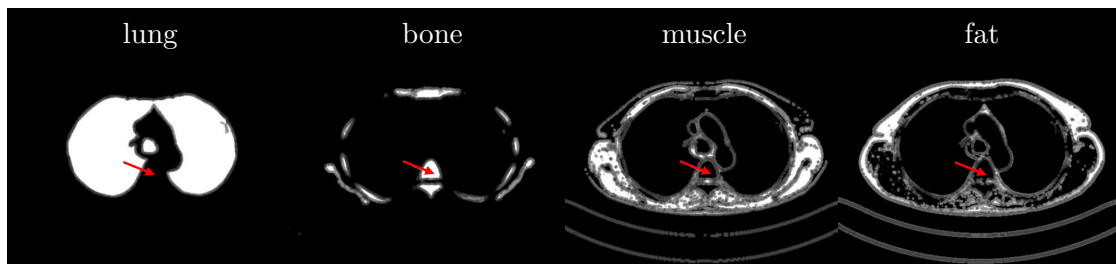
In the following chapter, the results corresponding to the three parts of the prior-based context-sensitive CT imaging, namely the context-sensitive image formation, the context-sensitive DECT evaluation and the quantitative pseudo multi material decomposition, will be presented. Parts of the results and conducted experiments have also been published in Dorn et al. (2018a,b,c).

4.1 Context-Sensitive CT Image Formation

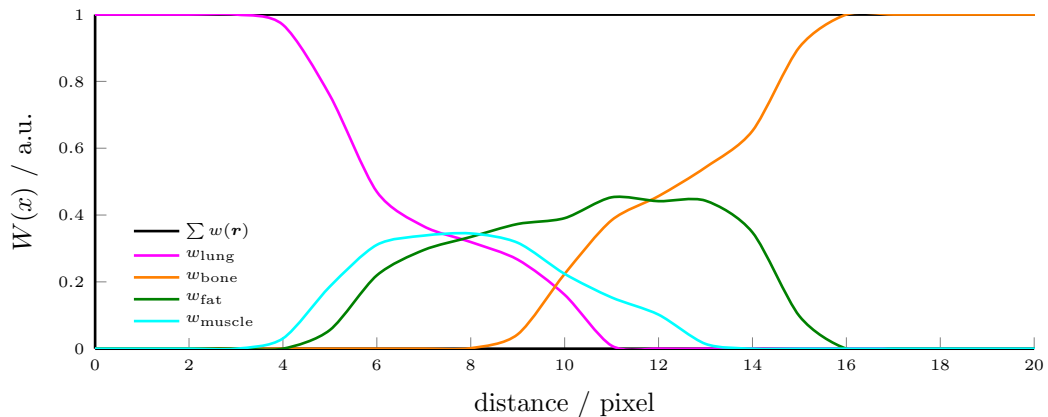
In the following section, the context-sensitive image formation is quantitatively and qualitatively evaluated based on six patient data sets that are acquired using a dual source dual energy CT system (SOMATOM Definition Flash, Siemens Healthineers, Forchheim, Germany) in the arterial and portal venous phase. The retrospective evaluation of acquired patient data was approved by the institutional review board of Heidelberg, Germany (S-316/2013). The study was conducted in accordance with the declaration of Helsinki (World Medical Association 2013).

The system operated in dual energy mode where the x-ray tube voltages were set to 100 and 140 kV+Sn, respectively. The x-ray tube generating the high voltage operated with a 0.4 mm tin filter to improve the spectral separation. Iodinated CM (300 mg iodine/mL, Imeron[®] 300 M, Bracco Imaging Deutschland GmbH, Konstanz, Germany) was administered as contrast agent with body weight-adapted volumes.

In addition to the low and the high energy image, the mixed image according to Equation (3.34) is calculated. The mixing weight $\alpha = 0.5$ is used as preset at the CT system. These images yield the same noise and contrast enhancement properties compared to a dose-equivalent single-energy CT scan at 120 kV (Krauss et al., 2011) and are used as basis images for the image formation of the context-sensitive resolution (Section 3.2.2). The resulting context-sensitive image is then displayed with the proposed organ-adapted image presentation techniques (Section 3.2.3).



(a) Tissue-related weights



(b) Contributions of tissue-related weights along red profile

Figure 4.1: (a) Tissue-related weights that are generated from the automatic segmentation to cope with the boundaries of adjacent anatomical regions. The position of the line profile is highlighted in red. (b) Line profile traversing four tissue types, i.e. lung, muscle, fat and bone to illustrate the contributions of the tissue-related weights to the associated basis images. The tissue-related weights determine the contribution of each basis image in the transition area of adjacent tissue labels.

4.1.1 Context-Sensitive Resolution

The tissue-related weights guide the weighted sum of involved basis images in the context-sensitive image formation. They are derived from the labeled volume and reflect the kernel-to-organ assignment which must be defined in advance. In order to analyze the influence of these tissue-related weights on the resulting context-sensitive image, the contributions of involved tissue-related weights along one arbitrary line profile is analyzed. The position of the line profile is chosen such that it traverses four tissue classes, namely the lung, bone and soft tissue consisting of muscle and fat. Figure 4.1a illustrates the considered tissue-related weight masks with the profile highlighted in red. The evaluated profiles of the corresponding masks are shown in Figure 4.1b. Each of these profiles exhibits the contribution of the corresponding involved tissue-related weight. Therefore, each voxel along the profile is composed of the assigned basis image weighted by their tissue-related coefficient. Since each of these weights is assigned to one basis image, it determines the contribution of that specific basis image in the transition area of adjacent tissue labels. The tissue-related weights are normalized such that all invoked masks sum up to one. The normalization ensures that the CT values of the context-sensitive image, which is composed of quantitative basis images, are not altered or lost in any case.

The context-sensitive images of six patients are shown in coronal and axial views in Figure 4.2. In this first example, the number of basis images is restricted to $B = 2$, where high attenuating structures, i.e. bone and lung, are reconstructed using a sharp basis image and soft tissue is reconstructed with a smooth basis image. The basis images are selected as follows: the sharp basis image f_{sharp} corresponds to a B80f kernel and the smooth basis image f_{smooth} corresponds to a B10f kernel. In order to highlight the advantages of the context-sensitive image, a piecewise magnification is also shown in a typical lung window ($C = -600 \text{ HU}/W = 1200 \text{ HU}$) and a typical body window ($C = 30 \text{ HU}/W = 400 \text{ HU}$). Different settings for typical window level settings are also summarized in Table 3.1. In addition, Figure 4.3 provides a comparison between the conventional reconstructed basis images and the associated context-sensitive image of Patient IV in a larger scale. A magnification taken from a more prominent region of each of the images is displayed in three different window level settings. The basis image selection is similar to that used in Figure 4.2. The compound image yields a significantly higher spatial resolution in high contrast regions, e.g. lung and bone, while maintaining a low noise level and high soft tissue contrast in the soft tissue compared to the basis images.

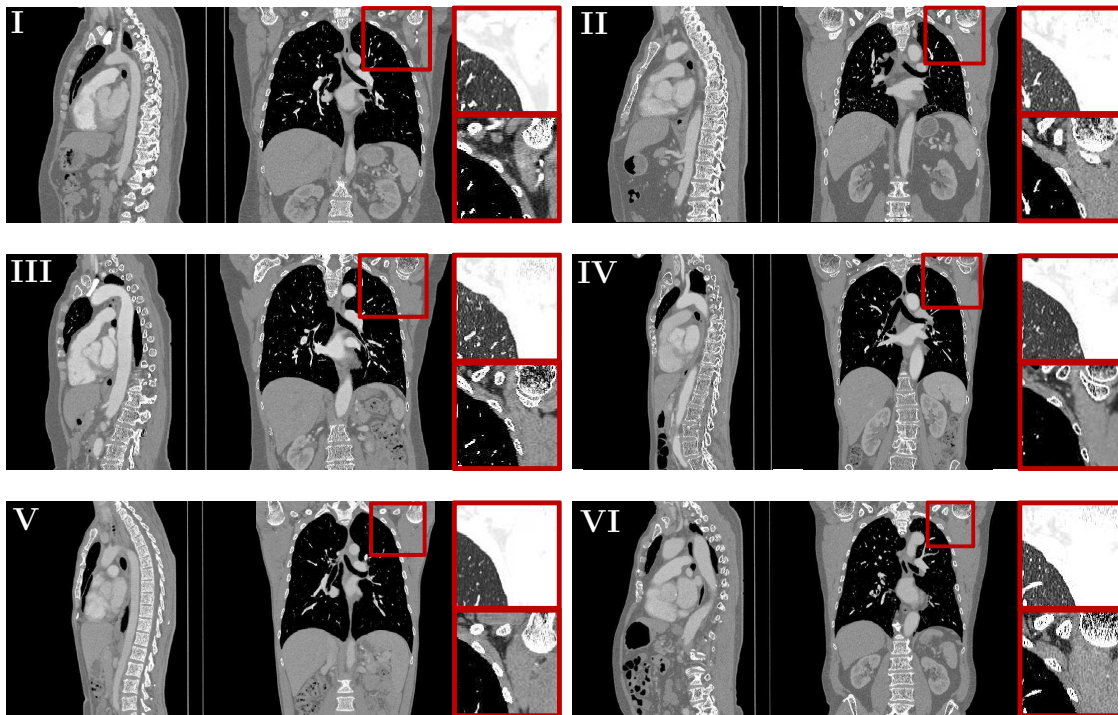


Figure 4.2: Context-sensitive reconstruction ($B = 2$) of six examined patient data sets in axial and coronal view ($C = 0 \text{ HU}/W = 1000 \text{ HU}$). The basis images are selected as follows: a sharp basis image f_{sharp} corresponding to a B80f kernel is selected for the reconstruction of lung and bone and the smooth basis image f_{smooth} corresponding to a B10f kernel is selected for the reconstruction of soft tissue. Additionally, a magnification of an image section is also shown in two typical windows: first in a lung window (upper magnification: $C = -600 \text{ HU}/W = 1200 \text{ HU}$) and secondly in a body window (lower magnification: $C = 30 \text{ HU}/W = 400 \text{ HU}$). The Roman numerals indicate the patient index and are also used in the following.

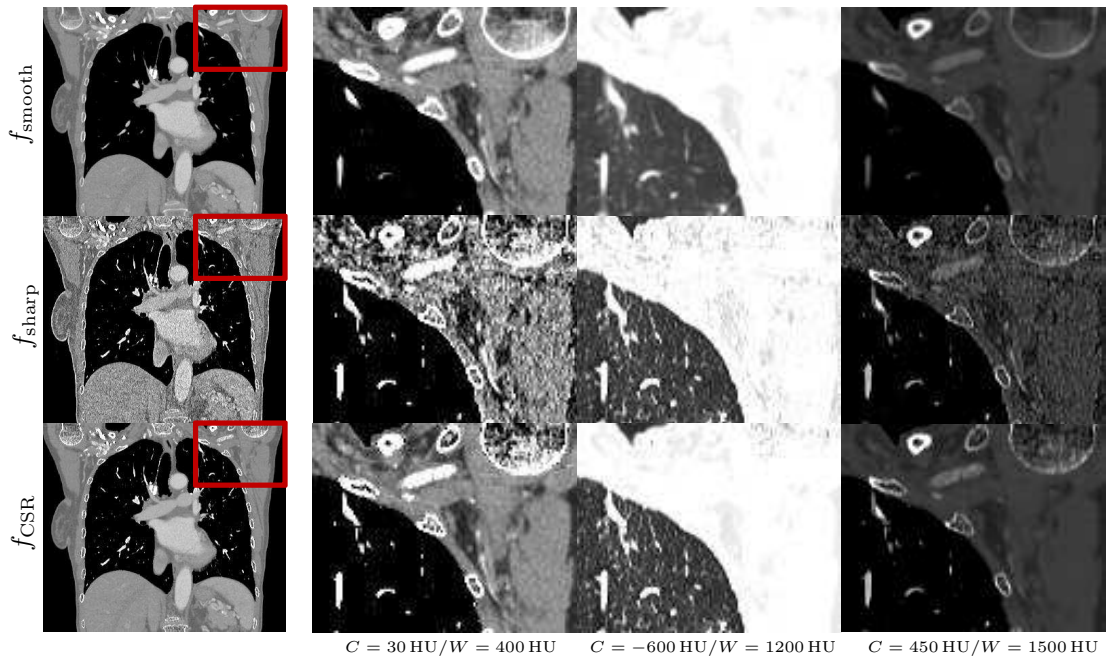


Figure 4.3: Comparison between the basis images and the context-sensitive image of Patient IV ($C = 0 \text{ HU}/W = 1000 \text{ HU}$). Moreover, a magnification is displayed in three different window level settings to draw the attention to different anatomical regions.

The number of basis images assigned to different anatomical regions is restricted to $B = 2$ and the width of the transition zone has not been considered yet. The following sections will provide a study on the influence of different parameter selections, in particular the number and choice of different kernels and the width of the transition zone.

Influence of Number and Choice of Different Kernels

The selection of the kernels is a function of the radiologists' preferences as well as a function of the body region. Depending on the radiologists' choice and the examined body part, a different number of kernels and a different selection of them are required. There is always the trade-off between high spatial resolution and low noise. On the one hand, there are sharp kernels that result in images with a high spatial resolution and there are smooth kernels that result in images with a low noise and high soft tissue contrast on the other hand. Since an incidental finding in soft tissue might always be suspected, most applications emphasize on a high soft tissue contrast with low noise in the abdomen resulting from a smooth kernel reconstruction. The diagnosis of the lung or bone requires a high spatial resolution, i.e. a sharp kernel reconstruction, since a higher noise is negligible in that structures. Therefore, at least a sharp and a smooth kernel are recommended in order to fulfill the discussed requirements. Moreover, specific organs, e.g. liver or heart, or specific applications, e.g. dual energy evaluations, may require more specific organ-adapted kernels as well. Figure 4.5 illustrates context-sensitive images at two different z -positions (abdomen and chest) that are composed of different basis images B ranging from $B = 2$ to $B = 5$:

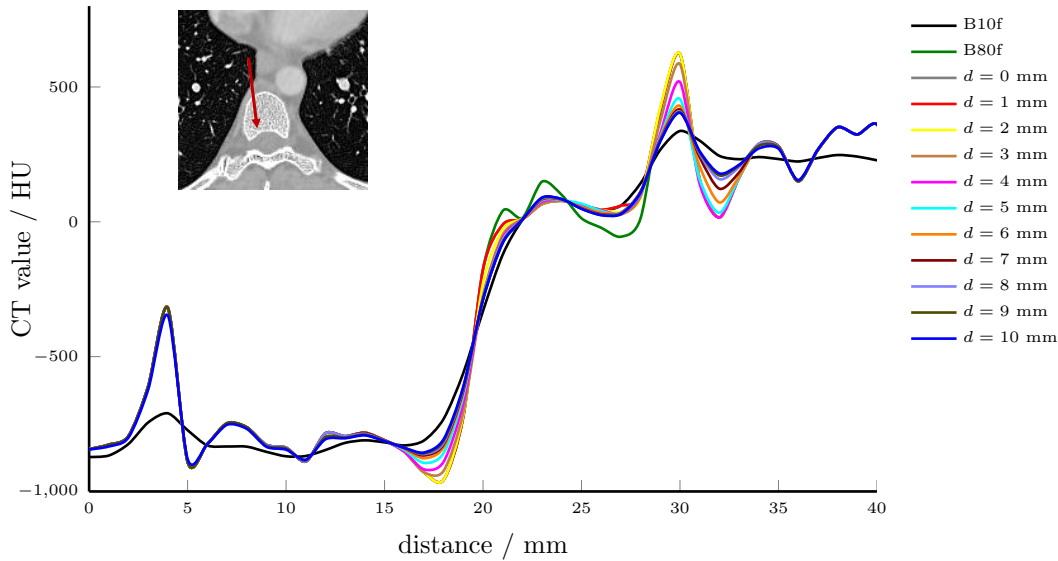
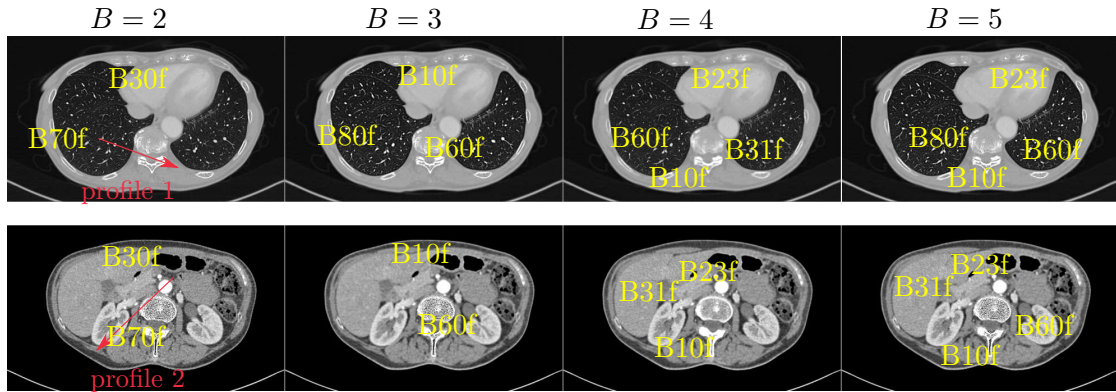
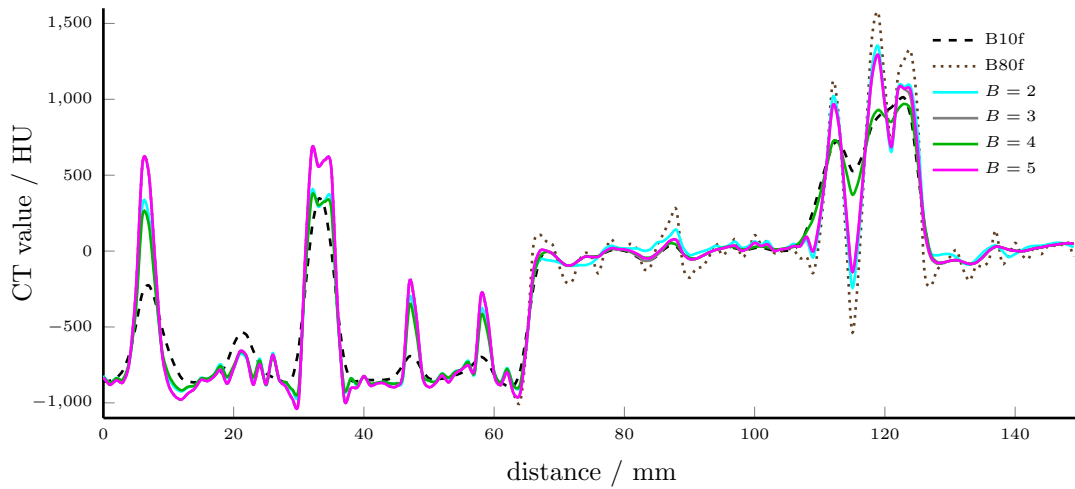


Figure 4.4: Influence of different transition widths in the context-sensitive image formation. The plot illustrates resulting CT value distributions along the profile drawn in red for different transition widths. Outside the transition zone, the profiles of the context-sensitive images are overlapping. Inside the transition zone, the contributions of involved basis images are averaged and reduce the peak CT value. Depending on the desired image sharpness in different anatomical regions, different widths are typically beneficial.

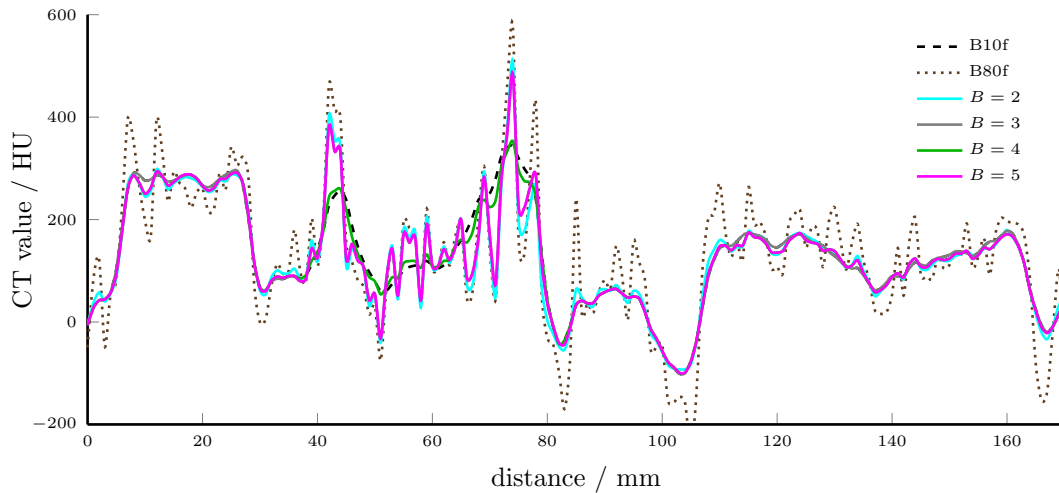
- $B = 2$: As shown before, two basis images are the minimum to combine mutually exclusive image properties. In this case, the context-sensitive image is composed of a sharp kernel (B70f) and a smooth dual energy kernel (D30f). The D30f kernel is optimized for quantitative images and avoids overshoots in the image.
- $B = 3$: In this case, soft tissue including muscles, larger abdominal organs, fat and vasculature is reconstructed with a very smooth kernel (B10f). The lung is reconstructed with a very sharp kernel (B80f) and bone is reconstructed with a medium sharp kernel (B60f). The decision to utilize a medium sharp kernel for the reconstruction of bone is motivated by the reduced noise level compared to the very sharp kernel and by the improved spatial resolution in comparison with conventionally used smooth kernel reconstructions.
- $B = 4$: The focus of the context-sensitive image is set on the improvement of the image quality in the abdomen. The lung is reconstructed using a sharp kernel (B70f) in order to obtain a superior spatial resolution compared to a reconstruction conducted with a smooth kernels. For the reconstruction of the remaining anatomical regions, three different organ-adapted kernels are selected. Soft tissue including muscle and fat are reconstructed with a very smooth kernel (B10f) in order to obtain a low noise level in these regions. The larger abdominal organs and bone are reconstructed with a B31f kernel (finer noise grain) and the vasculature is reconstructed with a B23f kernel, which includes a beam hardening correction for iodine. The latter two kernels are optimized for specific organs and are often recommended for this specific body parts.



(a) Context-sensitive images composed with $B = 2, B = 3, B = 4$ or $B = 5$ basis images.



(b) Profile 1 traversing lung, soft tissue and bone (thorax).



(c) Profile 2 traversing aorta, bone, fat, right kidney (abdomen).

Figure 4.5: (a) Context-sensitive images (Patient IV) composed of varying basis images shown at two different z -positions (thorax: $C = -200$ HU/ $W = 1800$ HU and abdomen: $C = 20$ HU/ $W = 400$ HU). The kernel number B and the kernel-to-organ assignment is changed for each image. Corresponding profiles to evaluate the spatial resolution and noise distribution are evaluated either traversing lung, soft tissue and bone (b) or traversing the aorta, bone, fat and right kidney (c).

- $B = 5$: This case illustrates the adaptation to each anatomical region. The kernel selection of case $B = 3$ for the lung and bone and the kernel selection of the case $B = 4$ for soft tissue are combined such that each anatomical region with available segmentation is reconstructed with the best adapted kernel.

Even if there are no usually recognizable major differences between the four different kernel selections (see Figure 4.5a), image properties like the noise level or spatial resolution differ significantly depending on the kernel-to-organ assignment. In order to highlight the differences between these setups, two line profiles are drawn at two different positions: one profile is located in the thorax and one line profile is located in the abdomen. Each of these profiles traverses several anatomical regions that are composed of various kernels. The thorax profile is shown in Figure 4.5b and the abdomen profile is shown in Figure 4.5c. In addition to the profiles of the context-sensitive image, the profiles of the very smooth and the very sharp kernel are illustrated by the dashed and dotted line, respectively. If the kernel selection matches between various context-sensitive images, the profiles are overlapping. In comparison to the basis images, it can be seen that the noise level in the soft tissue is significantly reduced and the spatial resolution in lung and bone is significantly enhanced in each of the context-sensitive images. It should be noted that the examination of different body regions requires a different selection of the kernels. Regarding the number of kernels, there is also a trade-off between the number of kernels and the associated number of transition zones. Whenever two adjacent anatomical regions are reconstructed with different kernels, an artificial transition zone is induced. Therefore, it can be argued that it is superior to reduce the number of transition zones by reducing the number of kernels, in particular if adjacent organs, e.g. liver and kidney, are very similar. In this case, the benefit of using another kernel in adjacent tissue regions needs to be balanced. Overall, there is no general restriction on the number of basis images and therefore B needs to be defined depending on the clinical need.

Influence of the Transition Zone

The width of the transition zone that is used to calculate the tissue-related weight for the composition of the context-sensitive image has a strong impact on the boundaries of adjacent tissues in the resulting context-sensitive image. Moreover, the diameter d strongly depends on the segmentation accuracy, because it determines the width of the weighted average calculation. Wherever one of the weights is within the open interval of 0 and 1, more than one basis image contribute to the context-sensitive image. The influence of the diameter of the transition zone is depicted in Figure 4.4. The profile traverses two artificial transitions, one between lung and muscle and one between muscle and bone. Outside the transition zone, the profiles of the context-sensitive images are overlapping. The resulting CT value distribution inside the transition zone varies depending on the width d . The width influences the contributions of involved basis images that are averaged resulting in a reduced peak CT value at sharp edges. Depending on the desired image sharpness, different widths are usually beneficial. However, it is difficult to determine one specific width without considering the qualitative image impression.

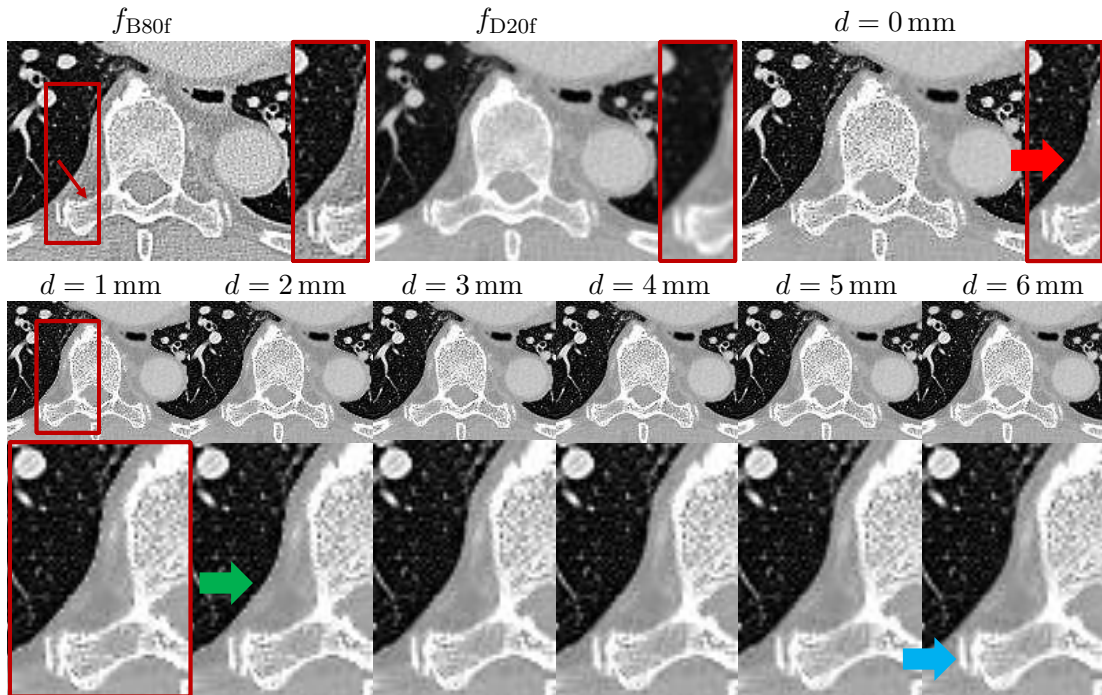


Figure 4.6: Influence of different transition widths in the context-sensitive image formation. From left to right ($C = -200$ HU, $W = 1500$ HU): If there is no transition zone ($d = 0$ mm), the border between lung and soft tissue (muscle and fat) shows a bright overshoot resulting from the sharp kernel reconstruction (red arrow). The adjacent soft tissue results from a sharp basis image because the volume of the binary lung mask is slightly too large and voxels are incorrectly assigned to the lung. On the other hand, a large transition width (e.g. $d = 6$ mm) results in a smoothing of the sharp kernel reconstruction in the bone (blue arrow). A transition width $d = 3$ mm results in a good trade-off between smoothness and sharpness without any artificial streaks (green arrow). The line profile along the thin red arrow is illustrated in Figure 4.8a.

Constant Transition Zone Widths

Figure 4.6 and Figure 4.7 depict the influence of varying transition widths for the context-sensitive image. Furthermore, a comparison with the basis images is provided therein. Both figures illustrate patient VI at different locations. The context-sensitive images have been composed of competing basis images, which are reconstructed with a very sharp (B80f) and a smooth quantitative (D20f) kernel. For one context-sensitive image, the transition width is chosen to be constant for every anatomical region. If no transition zone is used at all, i.e. the diameter is set to $d = 0$ mm, different artifacts appear at the boundary between adjacent anatomical regions. Figure 4.6 shows a bright overshoot that arises at the border between the lung and the soft tissue. The volume of the binary lung mask is slightly too large and therefore the voxels are incorrectly assigned to the lung mask at the boundaries of this organ. Voxels that should correctly be assigned to the soft tissue are therefore wrongly reconstructed with a sharp basis image. If the volume of the binary bone mask is slightly too large, a dark streak appears at the transition between bone and soft tissue, as it can be seen in Figure 4.7. Both artifacts are indicated with red arrows. On the other hand, a large transition zone width (e.g.

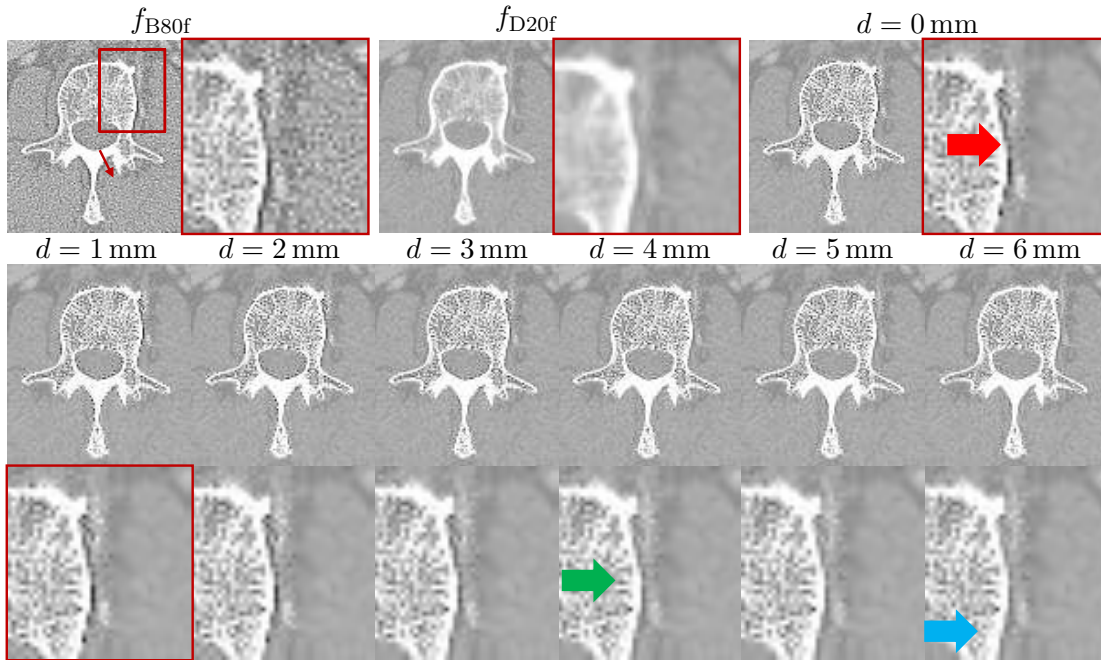


Figure 4.7: Influence of different transition widths in the context-sensitive image formation. From left to right ($C = -200 \text{ HU}/W = 1500 \text{ HU}$): In this case, if there is no transition zone ($d = 0 \text{ mm}$), the border between bone and soft tissue (muscle and fat) shows a dark streak (red arrow). The adjacent soft tissue is reconstructed with the kernel that is assigned to the bone because the volume of the binary bone mask is slightly too large. A large transition zone results in a smoothing of the sharp kernel reconstruction in the bone (blue arrow). A transition width $d = 4 \text{ mm}$ results in a good trade-off (green arrow). The line profile along the thin red arrow is illustrated in Figure 4.8b.

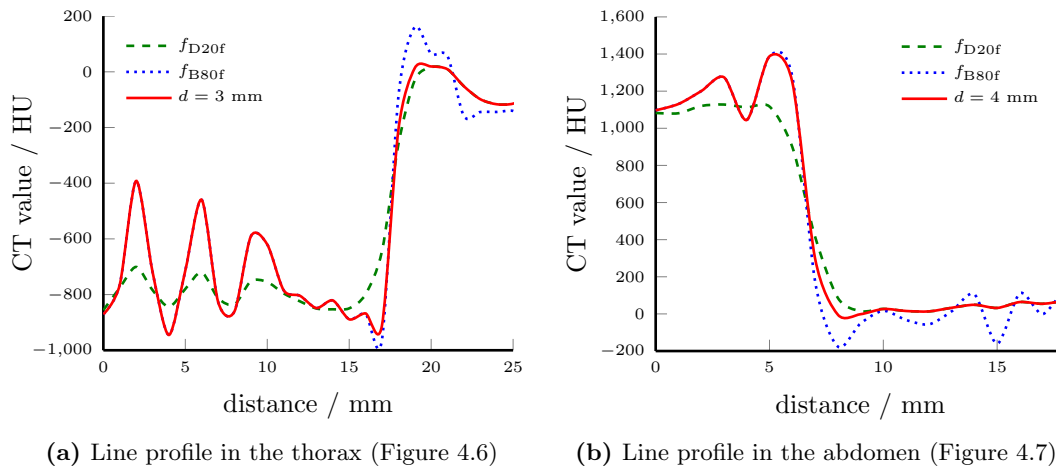


Figure 4.8: (a) Line profile traversing different anatomical regions in the thorax corresponding to Figure 4.6 (red arrow). (b) line profile traversing different anatomical regions in the abdomen corresponding to Figure 4.7 (red arrow). The strong overshoots at the tissue boundaries resulting from the sharp basis image are reduced by using a sufficient transition zone width, i.e. 3 mm in the thorax and 4 mm in the abdomen appears optimal.

$d = 6 \text{ mm}$) reduces the spatial resolution of the lung and bone, respectively. This is due to the fact that the sharp basis image and the smooth basis image of the surrounding

area are averaged in the transition zone. The green arrows indicate optimal transition widths: a transition width of $d = 3$ mm is optimal in the case of a lung–soft tissue transition and a transition width of $d = 4$ mm is optimal in the case of a bone–soft tissue transition in this specific patient. These optimum values result in a good trade–off between hard transitions and the loss of spatial resolution due to the averaging of adjacent basis image reconstructions. Line profiles that are drawn in the context–sensitive images with optimal transition width in comparison with the basis images are illustrated for both image sections in Figure 4.8. The position of the line profiles are highlighted in red in both f_{B80f} images (see Figure 4.6 and Figure 4.7). Figure 4.8a correspond to the lung–soft tissue case and Figure 4.8b correspond to the bone–soft tissue case. The overshoots resulting of the sharp basis image are reduced in both cases. However, it should be noted that the selection of d strongly depends on the segmentation accuracy and the kernel–to–organ assignment. If two adjacent anatomical structures are more similar than others, smaller transition zones can be used. Therefore, an adaptive selection of the transition width is expected to be superior.

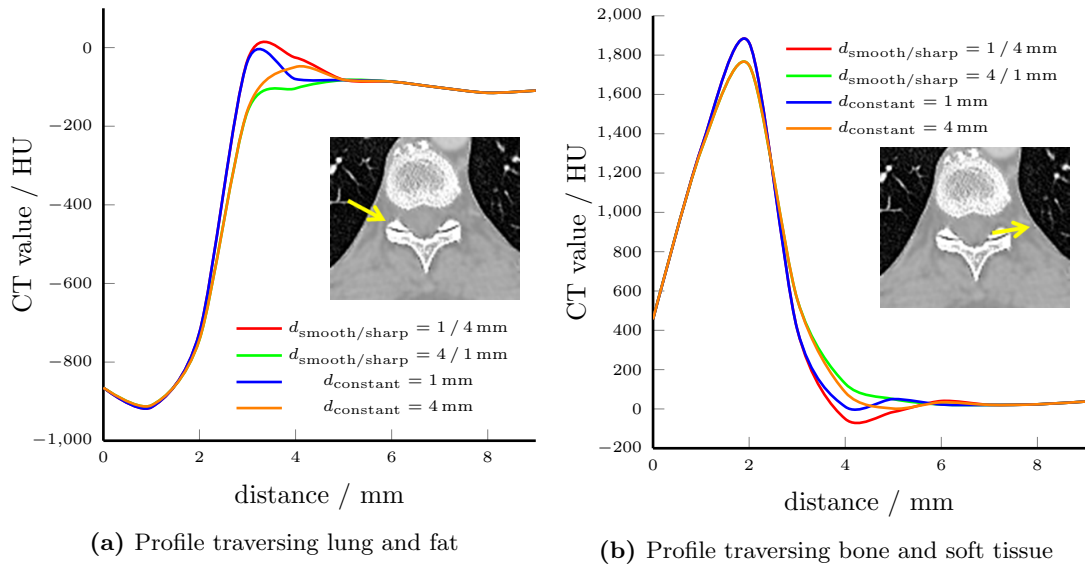


Figure 4.9: Organ–adaptive selection of the transition widths in comparison with constant transition widths for all adjacent organs. Please note that an organ–adaptive transition width is able to avoid overshoots.

Adaptive Transition Zone Widths

As mentioned above, there are some disadvantages using a constant transition zone. Particularly, there are different requirements depending on the type of adjacent tissues. The width of the transition zone between regions with very similar properties, e.g. kidney and spleen, or transitions between regions with competing properties, e.g. lung and fat, pose different challenges. A comparison of two constant transition widths and organ–adapted transition widths along two profiles is carried out in Figure 4.9. The constant transition widths are fixed to $d = 1$ mm and $d = 4$ mm, respectively. The adaptive width pair for the transition between a smooth and a sharp basis image is set as $d_{\text{smooth}} = 1$ mm

and $d_{\text{sharp}} = 4$ mm and vice versa. The green curve illustrates the profile corresponding to the setting $d_{\text{smooth}} = 1$ mm and $d_{\text{sharp}} = 4$ mm and results in the best transition between both basis images along the profile traversing lung and fat (Figure 4.9a) as well as along the profile traversing bone and soft tissue (Figure 4.9b). The vice versa case produces an overshoot resulting from the high contribution of the sharp basis image (red curve). If the transition zone is too small (constant case $d = 1$ mm), the overshoot of the sharp basis image is always present (blue curve). If the width of the constant transition zone is quite wide, the overshoot disappears by means of the weighted average of the basis images in the transition zone (orange curve). However, using large transition widths, there is always the risk of blurring which corrupts the visual image impression. In summary, small transition widths are superior for sharp basis images and larger transition zones might be beneficial in the case of smooth basis images. Overall, the more similar the required image properties are, the larger the transition zone can be. The transition zone between two competing anatomical structures (lung, soft tissue) needs to be smaller for the sharp basis images. The width of the transition zone that is assigned to the smooth basis images should be selected such that no artifacts appear at the border between two anatomical structures.

4.1.2 Context-Sensitive Image Display

In clinical practice, there are many predefined window level settings for different anatomical structures that are used for daily diagnosis. There is a variety of different organ-adapted settings that can be preset by default on a clinical CT device. However, within a single given gray level window, the full information that is contained in the context-sensitive image cannot be adequately visualized as shown in Figure 4.3. Each of these windows displays only one part of the anatomy with satisfactory contrast and image impression and therefore a switching between at least three different windows, in particular body, bone and lung window, is required during image reading. In the following section, the results of the organ-adaptive windowing and organ-adaptive sliding thin slab are shown and discussed.

Organ-Adaptive Windowing

Figure 4.10 demonstrates that the context-sensitive images with the use of the sophisticated organ-adapted windowing are able to present significantly more information to the reader compared to a conventional window, for instance the body window I. A selection of possible context-sensitive window level settings is shown in Table 4.1. Each of these windows differs by specific organ-related settings: The context-sensitive window I and II differ only by the gray window level settings that are selected for the lung and bone. However, both settings are very similar and may be adjusted to a desired visual perception. The vascular system, including the heart and the aorta, is windowed with an angiography window. It results in a wide window that maps high CT values due to a contrast enhancement induced by any contrast media uptake to a medium bright value. The liver window is a narrower window that improves the soft tissue contrast better than any other body window that is listed in Table 3.1. Liver vessels are therefore highlighted. The liver gray window level setting is used in all four context-sensitive

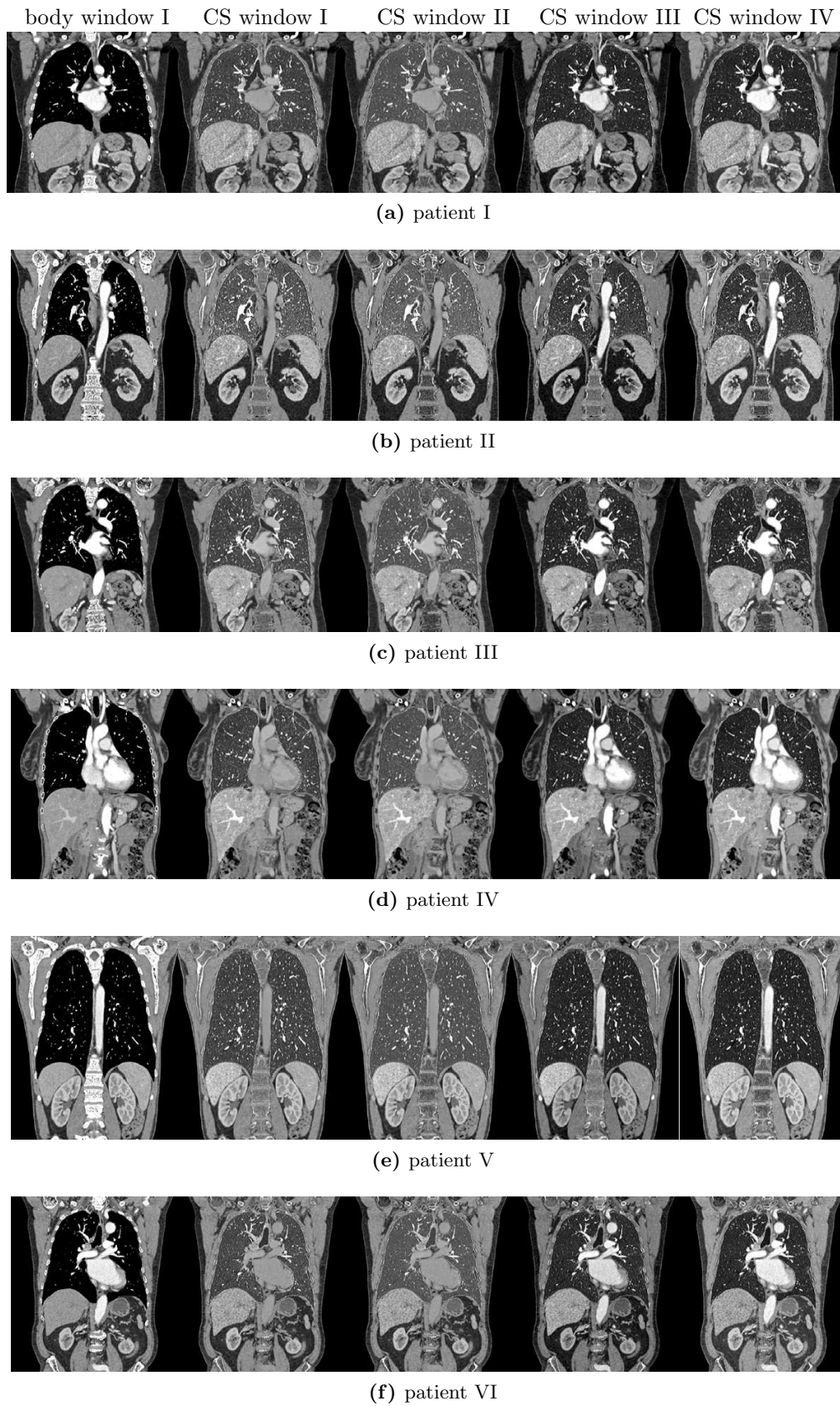


Figure 4.10: The context-sensitive images of six patients ((a)–(f)) are displayed in a conventional body window I (window level settings are listed in Table 3.1) and four different context-sensitive windows I–III that are listed in Table 4.1. Each of this context-sensitive windows locally adapts the window level settings depending on the organ.

Table 4.1: Exemplary CS window settings. The organ-related windows are listed in Table 3.1.

CS Window	Anatomy				
	Lung	Bone	Vasculature	Soft tissue	Liver
I	Lung I	Bone II	Angiography	Body I	Liver
II	Lung II	Bone I	Angiography	Body I	Liver
III	Lung III	Bone II	Body II	Body II	Body II
IV	Lung III	Bone I	Mediastinum	Abdomen	Liver

windows. The third context-sensitive window III favors a visual image impression that is very similar to a conventional image. It is achieved by using the lung window III. The contrast media uptake is not suppressed by applying the body window II to the entire soft tissue without any differentiation. The context-sensitive window IV again introduces a finer partitioning of the soft tissue into mediastinum, abdomen and liver but still remains very similar to the previous context-sensitive window setting.

Each of these CS windows have in common that the window level settings for each organ are adjustable individually depending on the specific demands. In addition to the overview of these context-sensitive window settings, Figure 4.11 depicts the context-sensitive windowing of patient V as well as selected magnifications at two distinct positions. The position of each box is highlighted in red in the coronal view. The coronal view as well as both magnifications are displayed in a conventional window (c.f. Table 3.1 body I) and the context-sensitive windows II, III, and IV. The first context-sensitive window is skipped due to the high similarity to the CS window II. In contrast to the conventional window, which only visualizes one part of the anatomy adequately, the adaptive windowing highlights each anatomical structure in a similar manner. Moreover, the combination of different window level settings in one image display is able to sufficiently highlight calcifications of larger vessels. The change between different window settings, i.e. switching between the CS window settings in the abdomen, reduces blooming effects of the calcifications and potentially enables a better delineation of the vessel lumen.

Influence of the Blending Zone

Similar to the influence of the transition width during the context-sensitive spatial resolution, the width of the blending diameter during the window blending is of great importance. Adjacent window level settings are smoothly blended in order to minimize artificial transition effects between competing window level settings. The width of the blending zone is determined by the parameter d , which is used in the calculation of the tissue-related weight. These recalculated organ-specific weight is then utilized in the context-sensitive windowing, in particular, in the organ-adapted window blending. Figure 4.12 illustrates the influence of different transition weights. It can be seen that a blending width of zero, i.e. no blending area is used at all, results in hard transitions between adjacent windows. On the contrary, if the blending width is too large, dark areas at the border of the lung emerge. The window settings used to display soft tissue contribute to the lung window level settings. Moreover, if the width of the blending zone

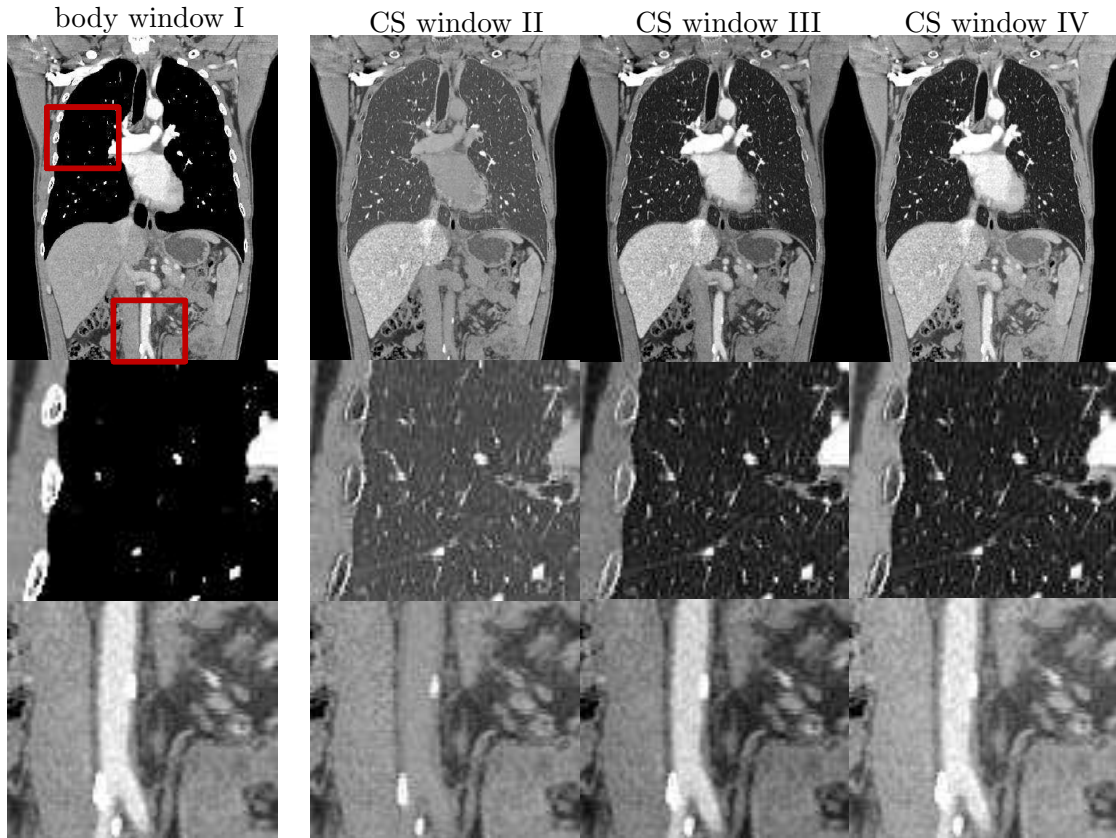


Figure 4.11: In addition to Figure 4.10, another representation of the context-sensitive windowing of patient V is shown. Magnifications are selected at two distinct positions which are highlighted with red boxes. The magnifications are displayed in a conventional window (body I) and the CS windows II, III, IV. The CS window I is omitted because of the high similarity to the CS window II. The magnifications highlights the benefit of the organ-adaptive windowing. In contrast to the conventional window, in which only one part of the anatomy is adequately visualized, the adaptive windowing highlights each anatomical structure in a similar manner.

is in the range of adjacent anatomical structures, they can disappear due to partial volume effects. For instance, a shrinking of small vessels can be observed in the transition zone between soft tissue and lung. CT values that need to be mapped to black in the soft tissue window are no longer mapped to black in the lung window. The dark areas around the lung can be misinterpreted as pneumothorax during diagnosis and therefore the width of the blending zone should be reduced as much as possible to achieve a superior image impression. The larger the blending width, the wider the hyper-dense areas become in the transition between lung and soft tissue. Therefore, the blending diameter must be assessed depending on the visual perception and freely specifiable by the user. Overall, a blending diameter of 2 mm provides a satisfactory trade-off for most of the patients.



Figure 4.12: Influence of different blending widths. If the blending width is set to zero, no blending is performed resulting in hard transitions between adjacent windows. However, because of an averaging of the center and the width of adjacent anatomical structures, e.g. lung and soft tissue, in the blending zone, artificial streaks may appear. CT values that are mapped to black in the soft tissue window are not mapped to black in the lung window. If the blending width around the lung is too large, dark areas arise, since the soft tissue window contributes to the lung window. The wider the blending zone, the darker appears the transition between lung and soft tissue. A blending width of 2 mm results in a satisfying trade-off (Patient II).

Organ-Adaptive Sliding Thin Slab

Figure 4.13 depicts the application of the organ-adaptive STS technique to the CS image (transition width is set to 4 mm) of all six patients. It provides a combined image display consisting of an organ-adaptive windowing in CS window III (blending width is set to 2 mm) and varying slab thicknesses and techniques depending on the organ. In order to reduce the noise in soft tissue, an STS Mean-IP is applied. The slab thickness of the Mean-IP is set to 5 mm for soft tissue, fat, kidneys, liver, spleen and vasculature. This selected value is able to reduce the noise level to a sufficient level and therefore to improve the soft tissue contrast particularly inside larger abdominal organs. The STS MIP is computed over 10 mm to highlight the parenchyma. In contrast to conventional STS techniques where the entire data set is processed, different STS displays are selected to corresponding relevant anatomical structures.

The comparison of one exemplary patient (IV) between a conventional CT image, the CS image with and without organ-adaptive windowing and the CS image with a sophisticated CS display (organ-adaptive windowing and STS) is shown Figure 4.14. The conventional CT image (Figure 4.14a) is a B31f kernel reconstruction displayed in

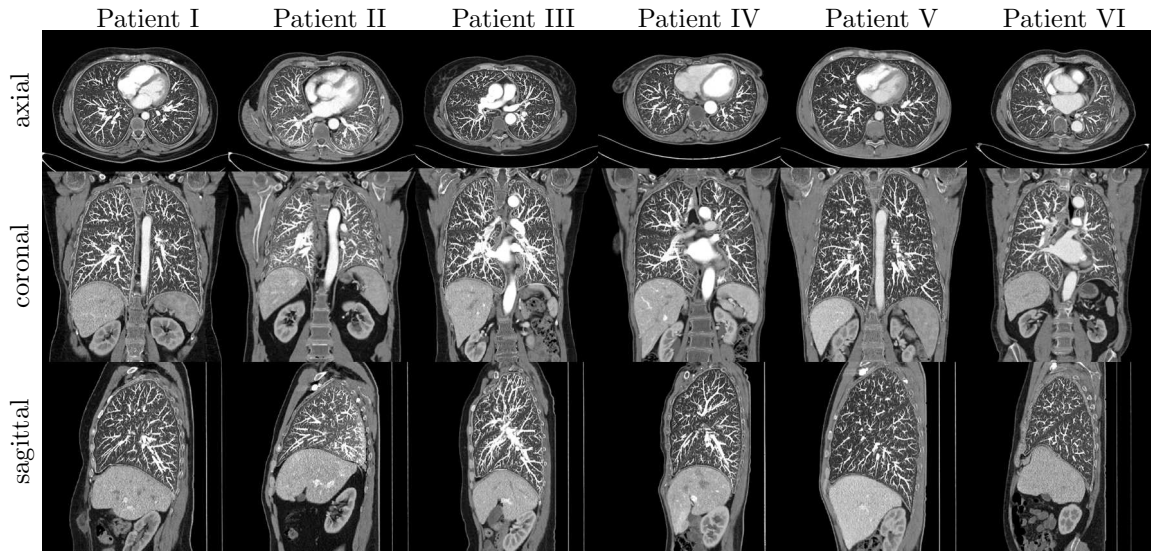
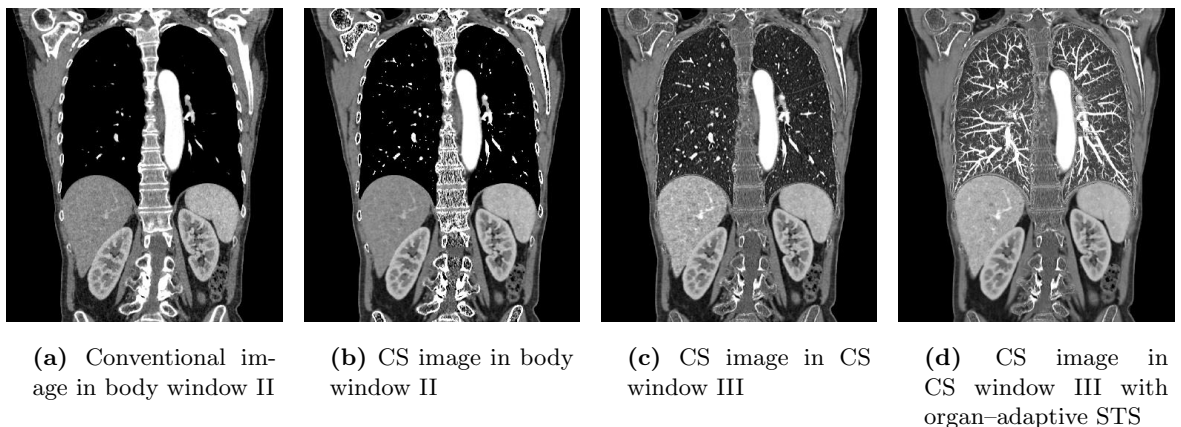


Figure 4.13: Organ-adaptive sliding thin slab (STS). The slab thicknesses and STS techniques, i.e. Mean-IP or MIP, vary between different anatomical structures. The STS Mean-IP slab thickness is set to 5 mm and the STS MIP slab thickness is set to 10 mm. All images are displayed using the CS window III.

body window II. The CS image is composed of a B10f kernel (soft tissue etc.) and a B80f kernel (lung and bone) reconstruction and is generated using a transition width of 4 mm. The image is then shown in body window II (Figure 4.14b) and in an organ-adaptive CS window III with a blending width of 2 mm (Figure 4.14c). The organ-adaptive STS settings used in Figure 4.14d are selected in a similar manner as in Figure 4.13. Using this approach, the advantages of varying window level settings and image display methods can be combined into a single viewing. It enables the simultaneous image reading of different anatomical structures.



(a) Conventional image in body window II

(b) CS image in body window II

(c) CS image in CS window III

(d) CS image in CS window III with organ-adaptive STS

Figure 4.14: Organ-adaptive sliding thin slab (STS). The slab thicknesses and STS technique varies between different anatomical structures. (CS window III).

4.2 Context-Sensitive Dual Energy

The principle of an organ-specific viewing is extended to perform an organ-adapted dual energy evaluation and analysis. In the following section, the results regarding the context-sensitive dual energy evaluation and analysis will be presented.

4.2.1 Organ-Specific DE Evaluation and Analysis

A organ-adapted dual energy evaluation is restricted to one specific anatomical region. For instance, the iodine quantification of the liver is only performed within the organ. The liver iodine quantification algorithm is automatically selected and applied to perform the DECT analysis. The final color-coded iodine uptake is only highlighted in the liver. Figure 4.15 illustrates a liver-specific iodine quantification that is performed in the arterial and portal venous phase for two different z -positions. It can be seen that the local iodine concentration changes over time and any perfusion defect can be observed. The principle of performing the DECT analysis in specific body parts is summarized in Figure 4.16. The figure provides an overview of the context-sensitive DECT evaluation scheme. Each application is automatically invoked and applied to the organ of interest.

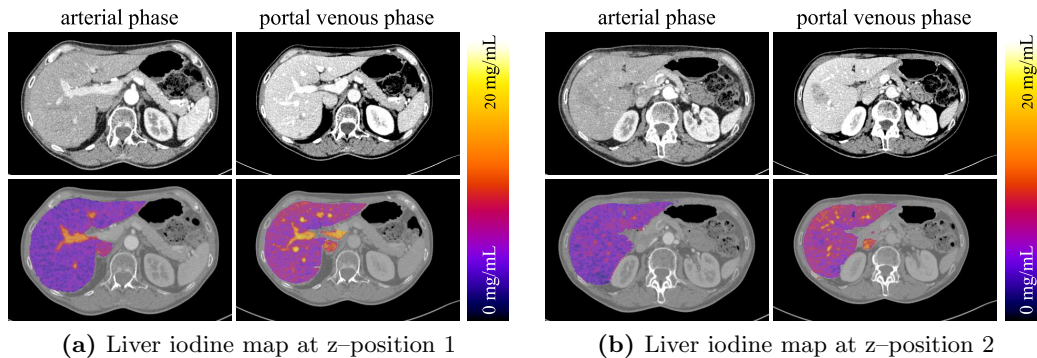


Figure 4.15: Organ-specific iodine quantification in the liver in the arterial and portal venous phase of patient IV at two different z -positions. Axial slices of the mixed image in the arterial and portal venous phase at two z -positions are shown in the upper row ($C = 40 \text{ HU}/W = 200 \text{ HU}$). These images are used as background for the organ-specific color overlay in the lower row. The color coding is restricted to the specific region of the liver.

As background for the various color overlays, the mixed image f_M is used. The scheme is applied to the arterial and portal venous phase. First, an iodine quantification of the perfused blood volume in the lung is performed. Then, the color overlay of the iodine uptake in the liver and the iodine uptake in the body, e.g. in the spleen, kidney and soft tissue, is added to the context-sensitive DECT. Each of these iodine maps is computed using the same algorithm but under different organ-specific calibrations. In particular, the liver and body iodine quantifications differ by their slope of the VNC line in the DECT space. Whereas the body VNC slope is equal to 1 and passes through the origin of the DECT coordinate system, the liver VNC slope is optimized for that specific organ. Voxels inside the liver are assumed to be a composition of fat and soft tissue, which are

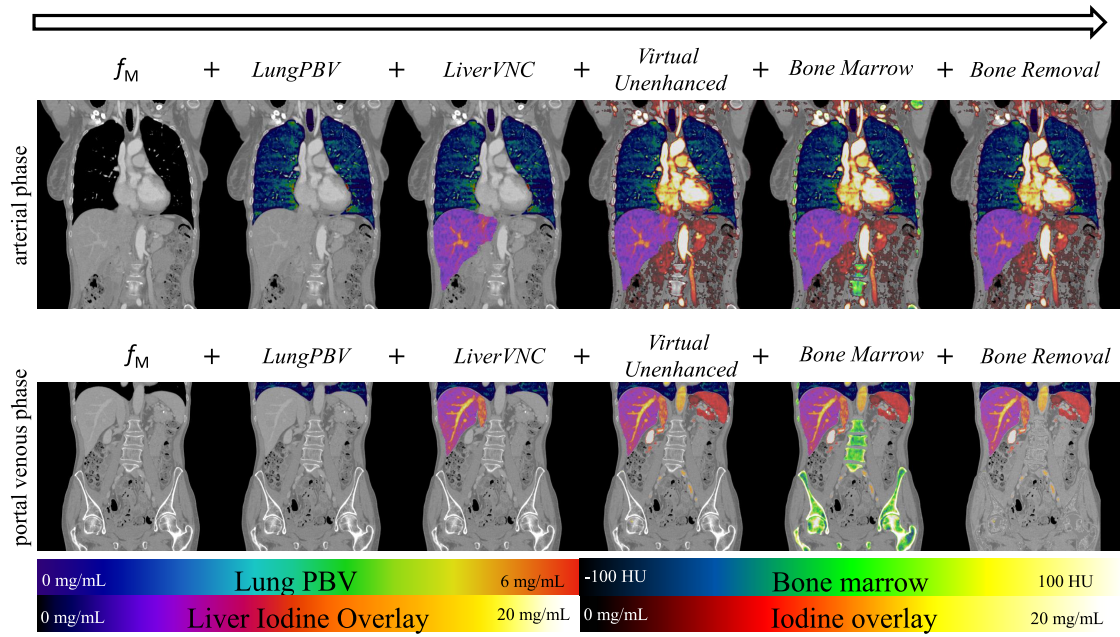


Figure 4.16: Context-sensitive DECT evaluation scheme. Each of these applications is invoked and applied to the organ of interest. Corresponding color codings are shown wherever appropriate.

therefore selected as reference points in the DECT space. The slope of the body iodine quantification is given by air and water resulting in a bisection of the DECT space. In addition to different iodine quantifications, a bone marrow analysis is performed. By virtually removing the calcium content from the bone, any CT value increase due to an infiltration or bone bruising is color-coded and visualized. Alternatively, the bone marrow analysis can be replaced by the bone removal application. The bone is virtually removed by classifying each voxel either as iodine or calcium voxel. Based on the classification, the calcium voxels are replaced by their water-equivalent attenuation value. The context-sensitive DECT scheme can be extended to include all possible DECT evaluations.

For instance, if there were some kidney stones, the presented evaluation scheme would be able to automatically detect and classify the stones. Each application is invoked only for the specific organ and the varying results are superimposed with different color codings. Within one single DECT image, different material decompositions and classification tasks are combined into one single evaluation tool. The corresponding color codings can be shown wherever appropriate.

4.2.2 Iodine Quantification Accuracy Study Using Default Parameters and Patient-Specific Calibrations

To evaluate the influence of default versus patient-specific calibrations of the relative contrast media ratio on the iodine quantification accuracy, a phantom study was conducted. Two anthropomorphic phantoms, i.e. liver and thorax shown in Figure 4.17 (QRM GmbH, Möhrendorf, Germany), equipped with vials of varying iodine concentration ranging from 2.5 and 30 mg/mL are measured with a dual source dual energy CT (SOMATOM Definition Flash, Siemens Healthineers, Forchheim, Germany). Three phantom sizes (small: 200×300 mm, medium: 250×350 mm, large: 300×400 mm) are realized by adding extension rings to the phantoms. The vial assembly in the liver



Figure 4.17: Anthropomorphic thorax phantom (a) and liver phantom (b) used in the iodine quantification accuracy study.

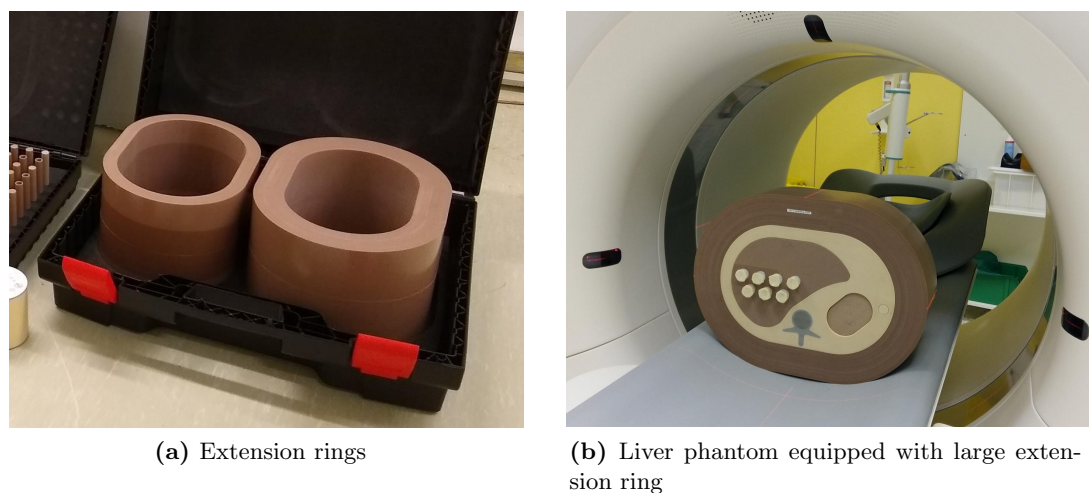
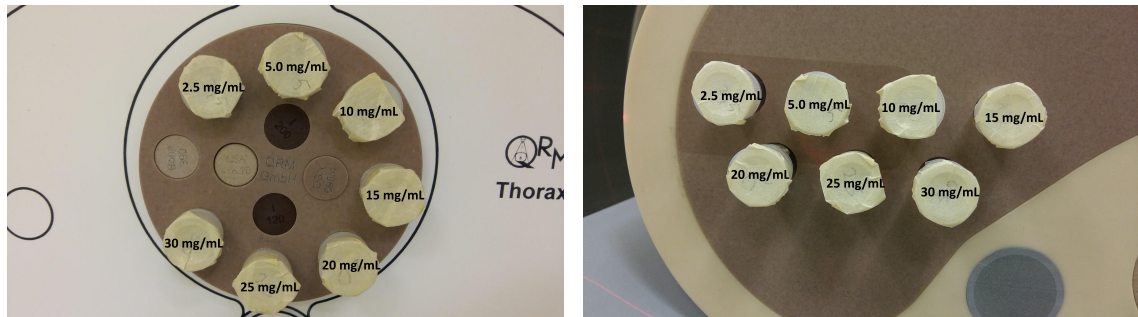


Figure 4.18: Phantom extension rings that are used to simulate three different patient sizes (a). The liver phantom equipped with the large extension ring mimicking an obese patient.

and thorax phantom is illustrated in Figure 4.19. Acquisitions are performed using two tube voltage combinations, in particular $80/140$ kV+Sn and $100/140$ kV+Sn at clinically relevant dose levels by activating CareDose. The default RelCM values, which are listed in Table 3.3 belonging to different tube voltage combinations, are used as preconfigured

by the vendor. The patient-specific RelCM R_{patient} is obtained by manually placing calibration ROIs inside the vials and calculating the RelCM value following Equation (3.19). The calibration ROIs are placed in the vial containing the lowest possible iodine concentration and highest possible concentration, respectively. The slope of the base line remains constant in order to ensure that the changes in iodine quantification accuracy are caused by the change in RelCM. The relative error for each vial is chosen as an



(a) Vials with varying iodine concentrations in the thorax phantom

(b) Vials with varying iodine concentration in the liver phantom

Figure 4.19: Arrangement of the seven vials with varying iodine concentrations in the thorax phantom (a) and in the liver phantom (b).

estimate of the deviation of the ground truth to the measured iodine concentration

$$\epsilon_v = \frac{|c_{\text{GT},v} - c_{\text{measured},v}|}{c_{\text{GT},v}}, \quad (4.1)$$

with $c_{\text{GT},v}$ being the ground truth (GT) iodine concentration as diluted in vial v and $c_{\text{measured},v}$ being the measured iodine concentration inside vial v in the material decomposed iodine overlay. The measured iodine concentration is calculated either using the default parameters or patient-specific calibrations. The iodine overlay is computed using the *LiverVNC* application at the clinical evaluation workstation. Averaging over all vials V yields the mean relative error obtained using different calibrations

$$\bar{\epsilon}_{\text{calib}} = \frac{1}{V} \sum_{v=1}^V \frac{|c_{\text{GT},v} - c_{\text{calib},v}|}{c_{\text{GT},v}}. \quad (4.2)$$

The mean relative error of the default parameter initialization $\bar{\epsilon}_{\text{default}}$ is compared against the mean relative error of patient-specific calibrations $\bar{\epsilon}_{\text{patient}}$ by analyzing the accuracy improvement factor

$$AIF = \frac{\bar{\epsilon}_{\text{default}} - \bar{\epsilon}_{\text{patient}}}{\bar{\epsilon}_{\text{default}}} \quad (4.3)$$

Figure 4.20 and Figure 4.21 depict the measured versus the true (GT) iodine concentrations for the default calibration as well as for patient-specific calibrations and the corresponding relative error for all three phantom sizes for the tube voltage combination of 80/140 kV+Sn. Since the plots for the tube voltage combination 100/140 kV+Sn shows comparable results, they are not shown here (see Appendix A).

Figures 4.20a–4.20c depict the measured and GT iodine concentration that are ob-

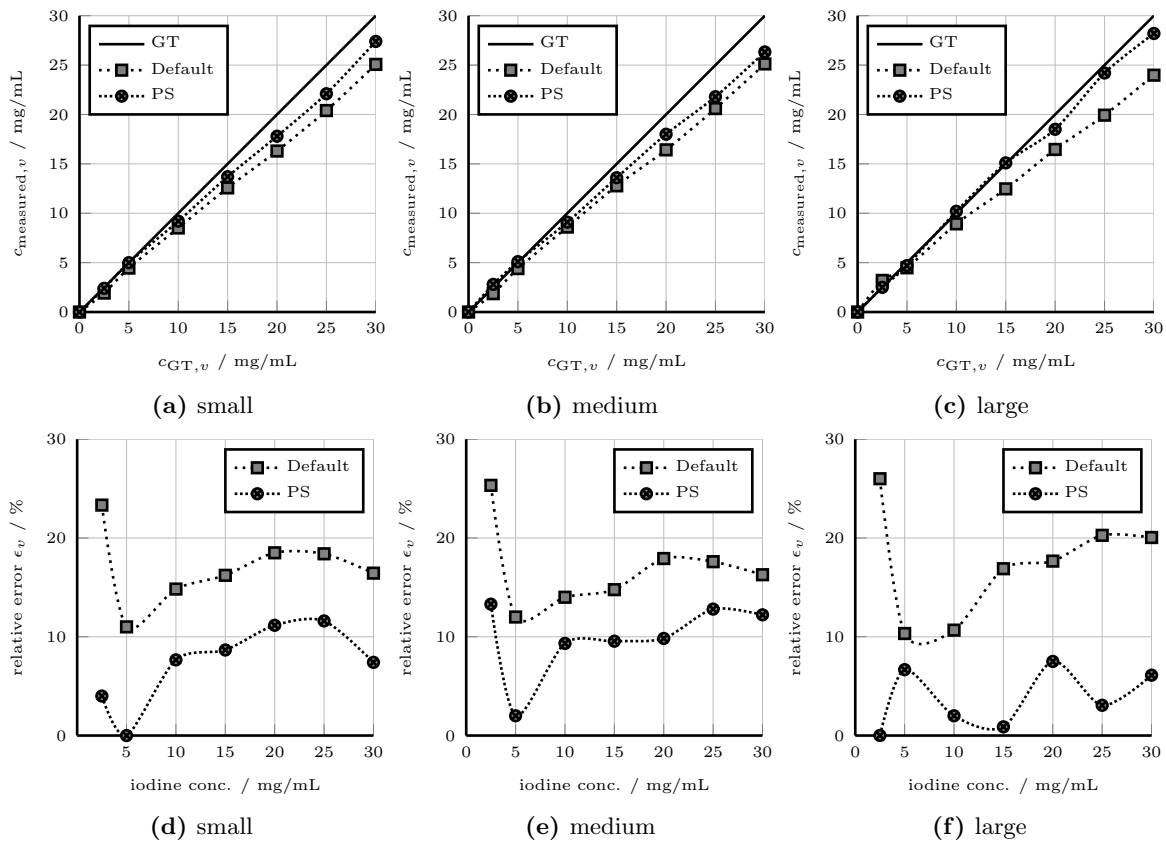


Figure 4.20: Liver phantom 80/140 kV+Sn. Figures 4.20a–4.20c show the measured iodine concentration $c_{\text{measured},v}$ and the true iodine concentration $c_{\text{GT},v}$ obtained using default and patient-specific (PS) calibration. Figures 4.20d–4.20f show the corresponding relative errors ϵ_v of the obtained iodine concentrations using default parameters and patient-specific calibrations. The calibration ROIs are evaluated in the vial containing the lowest and the highest iodine concentration, respectively.

tained using either default parameters or patient-specific calibrations evaluated in each vial for the liver phantom. In Figures 4.20d–4.20f, it can be seen that the relative error of the measured iodine concentration is significantly lower for the patient-specific calibration compared to the default parameter calibration for all three phantom sizes. For the large phantom size, the measured iodine concentration in the vial containing the lowest iodine concentration (2.5 mg/mL) is slightly overestimated using the default parameter calibration. The patient-specific calibration achieves an improvement of the iodine quantification by a factor of 2. Overall, it can be observed that the quantification accuracy is superior for high iodine concentrations and inferior for small iodine concentrations below 5 mg/mL.

Figures 4.21a–4.21c show the measured and true iodine concentration for the thorax phantom. The relative error obtained using patient-specific calibrations is significantly lower compared to default calibrations for all iodine concentrations and phantom sizes as plotted in Figures 4.21d–4.21f. Overall, the iodine quantification accuracy is higher for the thorax phantom than for the liver phantom. Due to lower attenuation of the x-ray beam through air equivalent tissue, the iodine quantification accuracy is less degraded by beam hardening and scatter. Since also the default calibration delivers a reasonable

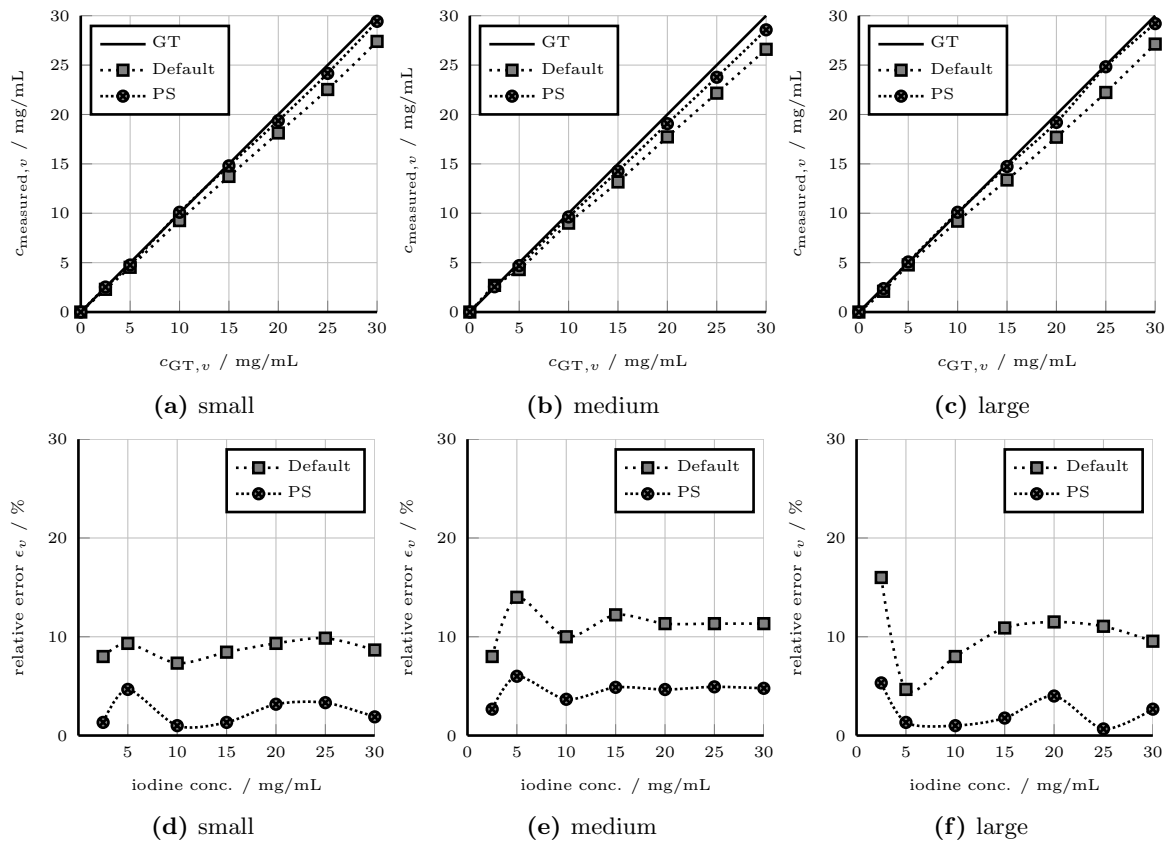


Figure 4.21: Thorax phantom 80/140 kV+Sn. Figures 4.21a–4.21c show the measured iodine concentration $c_{\text{measured},v}$ and the true iodine concentration $c_{\text{GT},v}$ obtained using default and patient-specific (PS) calibration. Figures 4.21d–4.21f show the corresponding relative errors ϵ_v of the obtained iodine concentrations using default parameters and patient-specific calibrations. The calibration ROIs are evaluated in the vial containing the lowest and in the highest iodine concentration, respectively.

iodine quantification accuracy, it might be suspected that the default RelCM has been calibrated with a phantom of similar density. The values of R_{patient} are listed in Table 4.2.

The patient-specific calibration of the relative iodine contrast ratio yields a reduction of the RelCM value for both tube voltage combinations and all phantom sizes. For both phantoms, the patient-specific RelCM R_{patient} is on average 5.9% (small), 5.0% (medium) and 9.8% (large) lower than R_{default} for the tube voltage combination 80/140 kV+Sn and on average 5.6% (small), 6.47% (medium), 4.24% (large) smaller for the tube voltage combination 100/140 kV+Sn. The mean relative error using default parameters or patient-specific calibrations as well as the corresponding accuracy improvement factor AIF is presented in Table 4.3. The observed RelCM reduction results in an improvement of the iodine quantification accuracy by 49.1% for the liver phantom and by 52.8% for the thorax phantom.

Using R_{patient} and tube voltage combination 80/140 kV+Sn, the relative error of measured to true iodine concentrations is decreased from 16.9% to 7.4% (small), 16.8% to 9.9% (medium) and 13.7% to 7.6% (large) for the liver phantom. The relative error for the thorax phantom is also reduced from 7.0% to 2.4% (small), 6.7% to 4.5% (medium) and 8.3% to 2.4% (large).

Table 4.2: Patient-specific calibrations of the relative iodine contrast ratio. The patient-specific calibrations yields a reduction of the RelCM value for both tube voltage combinations and all phantom sizes.

	Liver phantom				Thorax phantom			
	80/140 kV+Sn		100/140 kV+Sn		80/140 kV+Sn		100/140 kV+Sn	
	$R_{\text{default}} = 2.24$		$R_{\text{default}} = 3.01$		$R_{\text{default}} = 2.24$		$R_{\text{default}} = 3.01$	
	R	reduction	R	reduction	R	reduction	R	reduction
small	2.86	4.98 %	2.14	4.46 %	2.80	6.98 %	2.09	6.69 %
medium	2.91	3.32 %	2.10	6.25 %	2.81	6.65 %	2.23	0.44 %
large	2.67	11.30 %	2.14	4.46 %	2.76	8.31 %	2.15	4.02 %

Table 4.3: Iodine quantification accuracy improvement using patient-specific calibrations. A reduction of the RelCM value resulting from the patient-specific calibrations yields an improvement in iodine quantification accuracy.

phantom size	Liver phantom					
	80/140 kV+Sn			100/140 kV+Sn		
	\bar{c}_{default}	\bar{c}_{patient}	AIF	\bar{c}_{default}	\bar{c}_{patient}	AIF
small	16.96 %	7.41 %	56.31 %	14.00 %	6.23 %	55.5 %
medium	16.84 %	9.87 %	41.39 %	14.05 %	7.18 %	48.89 %
large	13.70 %	7.56 %	44.82 %	10.72 %	5.58 %	47.95 %
phantom size	Thorax phantom					
	80/140 kV+Sn			100/140 kV+Sn		
	\bar{c}_{default}	\bar{c}_{patient}	AIF	\bar{c}_{default}	\bar{c}_{patient}	AIF
small	8.71 %	2.36 %	72.90 %	9.23 %	5.43 %	69.98 %
medium	11.17 %	4.51 %	59.62 %	5.61 %	5.45 %	2.85 %
large	10.24 %	2.40 %	76.56 %	4.72 %	3.06 %	35.17 %

Using R_{patient} and tube voltage combination 100/140 kV+Sn, the relative error of measured to true iodine concentrations is decreased from 14.0 % to 6.2 % (small), 14.1 % to 7.2, % (medium) and 10.7 % to 5.6 % (large) for the liver phantom. The relative error for the thorax phantom is also reduced from 9.2 % to 5.4 % (small), 5.6 % to 5.5 % (medium) and 4.7 % to 3.1 % (large).

Overall, an iodine quantification accuracy improvement of 64.6 % (small), 50.4 % (medium) and 60.6 % (large) compared to the default value on average across all concentrations for the tube voltage combination 80/140 kV+Sn and an iodine quantification accuracy improvement of 62.7 % (small), 25.8, % (medium) and 41.56 % (large) for the tube voltage combination 100/140 kV+Sn is achieved. The phantom study suggests that a patient-specific calibration might also improve the iodine quantification accuracy in patient data.

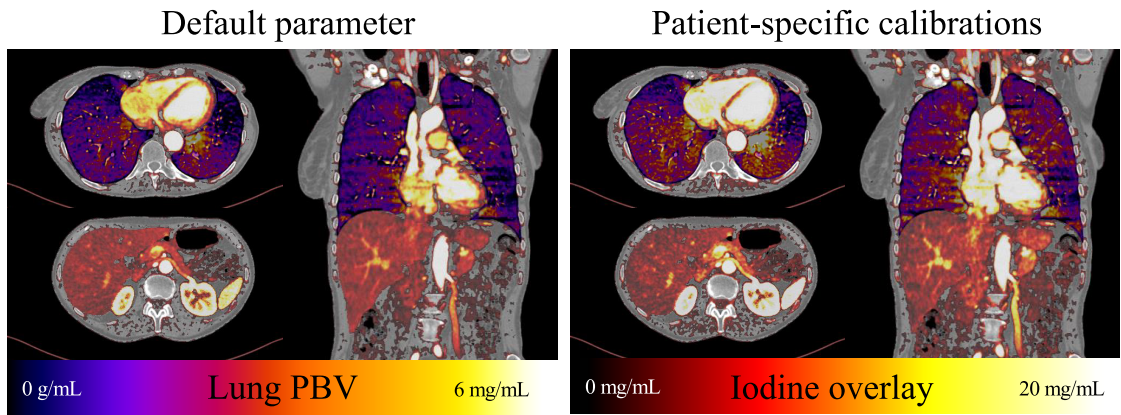


Figure 4.22: Qualitative evaluation of iodine overlays obtained using default parameter or patient-specific calibrations.

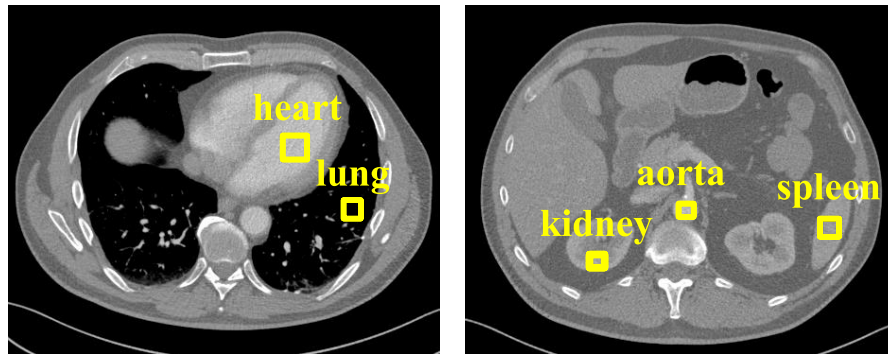


Figure 4.23: ROI positions used to analyze the iodine quantification accuracy depending on default parameters and patient-specific calibrations. The ROIs are evaluated at similar positions for all patient data sets.

4.2.3 Patient-Specific RelCM Calibration

After having considered the results of the phantom study, the influence of patient-specific calibrations on the iodine quantification accuracy on patient data will be examined. An estimate of the overall deviation between the iodine concentrations resulting from the default calibration c_{default} and the iodine concentration resulting from the patient-specific calibration c_{patient} is given by the mean relative error per patient

$$\epsilon_{\text{patient}} = \frac{1}{N} \sum_{n=1}^N \frac{|c_{\text{default},n} - c_{\text{patient},n}|}{c_{\text{default},n}}, \quad (4.4)$$

with N being the total number of evaluated ROIs. Furthermore, the root mean square error per patient is evaluated

$$\text{RMSE}_{\text{patient}} = \sqrt{\frac{1}{N} \sum_{n=1}^N (c_{\text{default},n} - c_{\text{patient},n})^2}. \quad (4.5)$$

Since the value of the true iodine concentration cannot be assessed, it is assumed that the default calibration provides a satisfactory trade-off and delivers accurate iodine con-

centrations. The iodine concentrations obtained with the default parameter are selected as reference iodine concentrations in order to evaluate the influence of patient-specific calibrations.

A qualitative comparison between the default parameter RelCM R_{default} and a patient-specific calibrated R_{patient} is shown in Figure 4.22 for Patient IV. The calibration ROIs are drawn in anatomical structures containing low (e.g. liver vessel) and high iodine concentrations (aorta). Nearly identical iodine distributions are indicated in the color overlays for default parameters and the patient-specific calibration. A quantitative evaluation of the iodine content in five ROIs results in a root mean square error of 0.079 mg/mL for this patient. In order to evaluate the iodine quantification accuracy for all six patients depending on default parameters and patient-specific calibrations, the mean values of the iodine content in five ROIs is analyzed. The ROIs are placed in different anatomical structures, i.e. in the aorta, lung, spleen, kidney, and liver and the positions of the ROIs are shown in Figure 4.23. The ROIs are placed with similar size and positions in each of the evaluated patients I to VI. Table 4.4 lists the mean values of measured iodine concentrations using default and patient-specific calibrations. The patient-specific calibration yields iodine concentrations which are in accordance to the iodine concentrations obtained with the default calibration.

The adapted relative iodine media ratio R per patient is summarized in Table 4.5. Moreover, the table lists the patient-specific mean relative error and the root mean squared error per patient, where the last row of the table highlights the mean and standard deviation of the overall relative iodine contrast ratio R , the relative error e and the RMSE over all patients. In summary, a mean relative error of $3.04 \pm 1.26\%$ that corresponds to an RMSE of 0.16 ± 0.08 mg/mL is obtained using the patient-specific calibration. These deviations result from the adaptation of the relative contrast media ratio R_{patient} to the actual patient size. The patient-specific calibration, which delivered values ranging from 2.132 to 2.227 depending on the patient, therefore compensates for beam hardening and scatter.

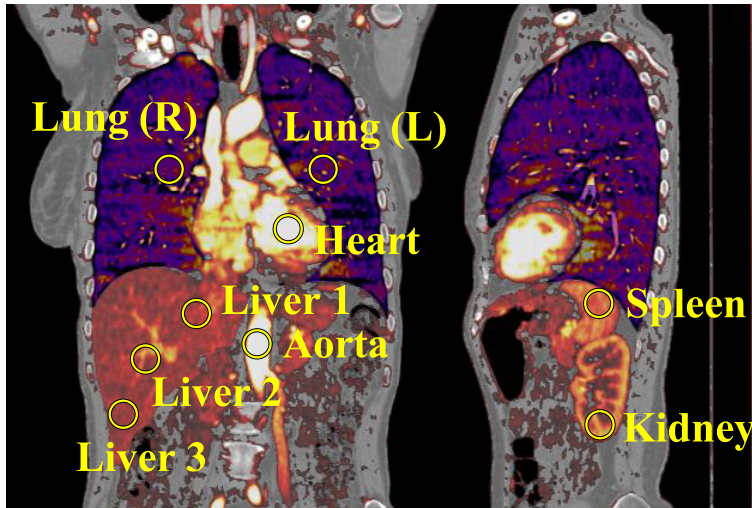
In order to minimize the calibration bias introduced by the user who manually places the ROIs in the patient data set, the patient-specific calibration has been repeated 9 times by different users. The resulting iodine quantification is evaluated in $N = 9$ different anatomical structures, i.e. in the aorta, heart, spleen, kidney, left and right lung, and three different positions in the liver. The corresponding positions of the evaluation ROIs are highlighted in Figure 4.24a. Figure 4.24b illustrates the measured iodine concentration using the default parameter and patient-specific calibrations including the 95% confidence interval of the repeated evaluations. Overall, the patient-specific calibration results in higher iodine concentrations compared to the default parameter. The higher the iodine concentration in different anatomical structures, the larger the bias introduced by the different patient-specific calibrations and thus the higher the variance of obtained iodine concentrations. However, this trial supports the findings of the phantom study. The default RelCM tends to underestimate the true iodine concentration and is therefore a trade-off between iodine quantification accuracy and patient-size dependent beam hardening and scatter effects.

Table 4.4: Evaluation of the mean iodine concentration c_{default} and c_{patient} in different anatomical structures for six example patients. The corresponding ROIs of example patient I are shown in Figure 4.23. Please note that comparable ROIs are evaluated with similar size and positions in all patients.

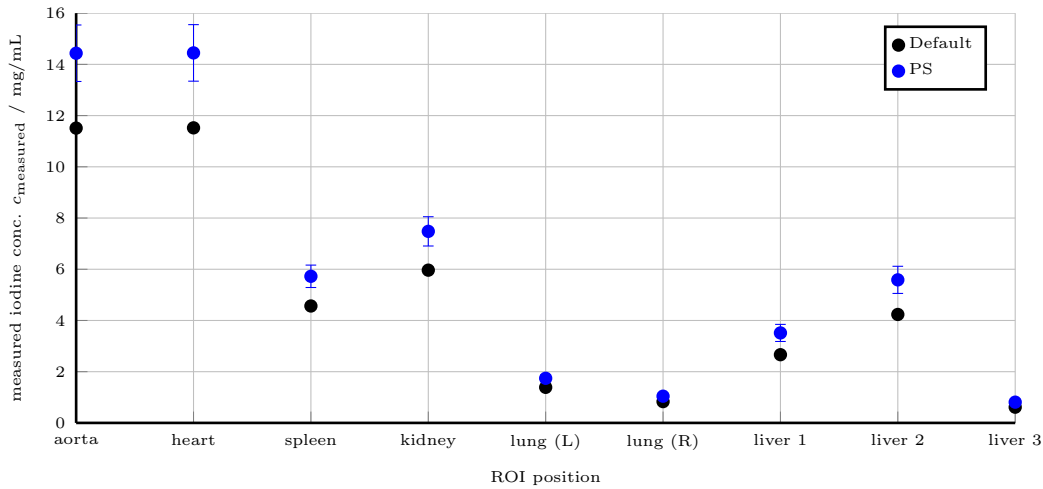
	Patient I		Patient II	
	c_{default}	c_{patient}	c_{default}	c_{patient}
aorta	9.92 mg/mL	9.97 mg/mL	13.43 mg/mL	13.12 mg/mL
heart	9.23 mg/mL	9.33 mg/mL	11.52 mg/mL	11.27 mg/mL
spleen	2.61 mg/mL	2.67 mg/mL	4.57 mg/mL	4.47 mg/mL
kidney	4.85 mg/mL	4.90 mg/mL	5.97 mg/mL	5.84 mg/mL
lung	1.81 mg/mL	1.65 mg/mL	1.39 mg/mL	1.27 mg/mL
	Patient III		Patient IV	
	c_{default}	c_{patient}	c_{default}	c_{patient}
aorta	8.63 mg/mL	9.14 mg/mL	9.31 mg/mL	9.38 mg/mL
heart	7.27 mg/mL	7.70 mg/mL	9.51 mg/mL	9.58 mg/mL
spleen	2.12 mg/mL	2.24 mg/mL	3.20 mg/mL	3.22 mg/mL
kidney	3.84 mg/mL	4.06 mg/mL	4.79 mg/mL	4.83 mg/mL
lung	1.52 mg/mL	1.59 mg/mL	2.11 mg/mL	1.97 mg/mL
	Patient V		Patient VI	
	c_{default}	c_{patient}	c_{default}	c_{patient}
aorta	9.51 mg/mL	9.74 mg/mL	9.08 mg/mL	9.23 mg/mL
heart	8.92 mg/mL	9.13 mg/mL	11.44 mg/mL	11.63 mg/mL
spleen	2.32 mg/mL	2.38 mg/mL	2.84 mg/mL	2.89 mg/mL
kidney	5.74 mg/mL	5.87 mg/mL	4.97 mg/mL	5.05 mg/mL
lung	2.06 mg/mL	2.15 mg/mL	2.00 mg/mL	2.04 mg/mL

Table 4.5: Patient-specific relative iodine contrast, corresponding mean relative error and root mean square error between measured iodine concentrations resulting from default vs. patient-specific calibration of the six example patients. Please note that the last row represents the mean and standard deviation of the overall patient-specific relative iodine contrast R_{patient} , the overall e_{patient} and overall $\text{RMSE}_{\text{patient}}$.

Patient	R_{patient}	e_{patient}	$\text{RMSE}_{\text{patient}}$
I	2.226	2.79 %	0.095 mg/mL
II	2.227	3.50 %	0.20 mg/mL
III	2.132	5.54 %	0.32 mg/mL
IV	2.145	1.92 %	0.079 mg/mL
V	2.194	2.76 %	0.16 mg/mL
VI	2.206	1.74 %	0.12 mg/mL
overall $\mu \pm \sigma$	2.188 ± 0.037	$3.04 \pm 1.26 \%$	$0.16 \pm 0.08 \text{ mg/mL}$



(a) Color-coded iodine uptake and positions of 9 ROIs that are used to evaluate the iodine concentration depending on the calibration method: default vs. patient-specific.



(b) Iodine concentration obtained using default and patient-specific calibrations. The results of the repeated PS calibration are within within the 95 % confidence interval.

Figure 4.24: Evaluation of the patient-specific calibration vs. default parameters for patient data. Since there is no ground truth available, the obtained iodine concentrations are compared against the concentrations obtained using the default parameters. All results are within the 95 % confidence interval. The calibration ROIs are evaluated $N = 9$ times in anatomical structures containing low (e.g. liver vessel) and high iodine concentrations (e.g. aorta) by different experienced users.

4.3 Quantitative Pseudo Multi Material Decomposition

As described in Section 3.4, organ-adapted three material decompositions are performed in order to achieve a quantitative pseudo multi material decomposition of DECT data. First, the thorax phantom as shown in Figure 4.17a with three different phantom sizes (see Figure 4.18a) is examined to evaluate the material quantification performance depending on different calibrations by means of the volume fraction accuracy, which will be defined in the following. Secondly, the results of the material decomposition into seven basis materials is shown for patient data. The section concludes with an novel

data presentation of the material images in order to give a short outlook what could be employed during diagnosis.

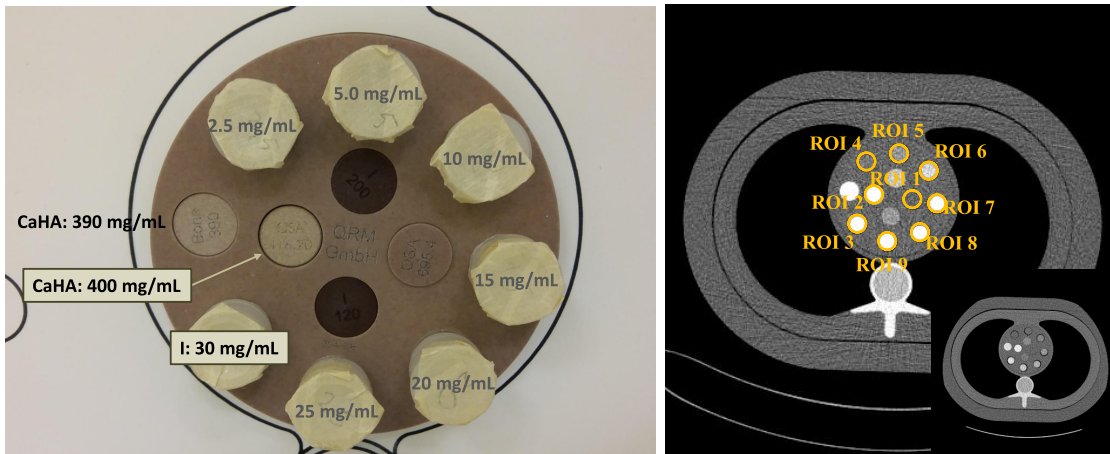
4.3.1 Simulation-Based and Patient-Specific Basis Material Calibration

The thorax phantom was reused to analyze the material decomposition accuracy of the organ-adapted three material decompositions with regard to different calibrations of the basis materials. Therefore, the cylindrical insert, which is equipped with different iodine filled vials and CaHA rods, is decomposed into the three basis materials water, iodine and CaHA. A magnification of the insert is illustrated in Figure 4.25a. The basis materials are either calibrated using simulations of the linear attenuation coefficients of CaHA and iodine at the effective energies of both spectra or using the evaluation of user-defined ROIs. The calibration is performed such that a iodine concentration of 30 mg/mL corresponds to a volume fraction of 1 for CM and a CaHA concentration of 400 mg/mL corresponds to a volume fraction of 1 for bone. For the patient-specific calibration, two rods with these basis material concentrations are available in the phantom. For the evaluation of the material quantification performance, the volume fraction accuracy is used. The *VFA* according to Xue et al. (2017) is defined as follows

$$VFA = \left(1 - \frac{1}{N} \sum_{l=1}^N \frac{\|x_n^{\text{GT}} - \bar{x}_n\|_2}{x_n^{\text{GT}}} \right), \quad (4.6)$$

with N being the total number of evaluated material-specific ROIs, x_n^{GT} being the ground truth value of the n -th material and \bar{x}_n being the mean value within the corresponding ROI. The iodine concentrations in the vials are converted to volume fractions in order to get the GT values. The GT values of the volume fractions inside the vials are generated by reorganizing Equation (3.39) to $f_{\text{vial}} = \frac{\gamma_{\text{vial}}}{\rho_{\text{CM}}}$ with $\rho_{\text{CM}} = 30$ mg/mL. The GT values of the three basis materials and the basis material volume fractions of three generic iodine dilutions are also listed in Table 4.6. The ROI positions and numbers are highlighted in the low energy image of the thorax phantom in Figure 4.25b. In the lower right, the high energy image is also illustrated. The ROI to calibrate the basis material “bone” is evaluated inside the bone insert consisting of 400 mg/mL CaHA (ROI 2). The ROI to calibrate the basis material “iodine” is evaluated inside the iodinated vial with the mixed concentration of 30 mg/mL iodine (ROI 3).

In addition to the GT values the obtained volume fractions depending on the performed calibration as well as the corresponding relative errors for the tube voltage combination 80/140 kV+Sn are listed in Table 4.6 and Table 4.7. Both tables present the material decomposition results for three different phantom sizes S, M and L for the simulation-based (Sim) and patient-specific (PS) calibration. All ROIs have been evaluated and the results of ROI 1, 2 and 3 (pure basis materials) are listed in Table 4.6. The volume fractions corresponding to the ROIs containing different predefined iodine mixtures are listed in Table 4.7, where the last column of this table illustrates the mean relative error of the measured volume fractions over all ROIs. Since the CT values within the ROIs 4 to 9 linearly increase with the iodine concentration, the relative error



(a) Inserts used for basis material calibration. The insert consisting of 400 mg/mL CaHA is used to calibrate bone and the vial containing a 30 mg/mL iodinated solution is used to calibrate for iodine.

(b) Low energy image of the thorax phantom with highlighted ROI positions and numbering. In the lower right, the high energy image is illustrated. ($C = 100$ HU/ $W = 700$ HU)

Figure 4.25: For calibration purposes, the ROI to calibrate the basis material “bone” is evaluated inside the bone insert consisting of 400 mg/mL CaHA (ROI 2). The ROI to calibrate the basis material “iodine” is evaluated inside the iodinated vial with the mixed concentration of 30 mg/mL iodine (ROI 3). The composition of the ROIs 4–9 is given by varying iodine solutions between 2.5 and 25 mg/mL iodine.

of the volume fractions is approximately within the same range for all ROIs. Moreover, it should be noted that the calibration ROIs are placed at different z -positions and are averaged over all positions in order to avoid overfitting. Overall, the PS calibration yields more accurate volume fractions. In particular, the relative errors of the iodine fractions of the PS calibration are significantly lower compared to the relative errors obtained with the Sim calibration. However, the PS calibration performs slightly worse for the determination of the volume fractions of CaHA. If the Sim calibration performs well, i.e. the achieved relative error is between 0.15 % and 1.32 % (highlighted in green), the PS calibration does not improve the results significantly. The corresponding VFA depending on different calibrations in ROI 1–3 are shown in Figure 4.26a. It plots the obtained VFA values for different phantom sizes and tube voltage combinations. Figure 4.26b shows the material images of the decomposition into its three basis materials. Although the material images show visually no significant difference between the Sim and PS calibration, a higher VFA is achieved using PS calibrations of the basis materials. Moreover, the smaller the patient, the higher the VFA becomes.

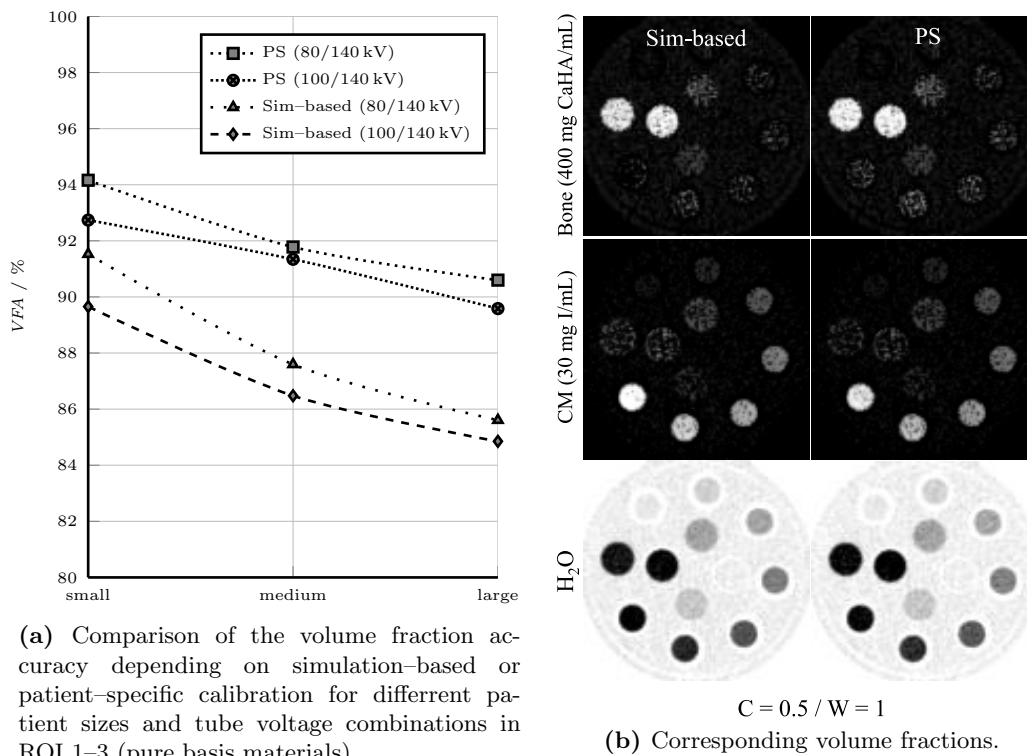


Figure 4.26: Evaluation of the decomposition accuracy by means of the volume fraction accuracy VFA defined in Equation (4.6) depending on different calibrations in ROI 1–3 (pure basis materials). The basis materials are either calibrated by simulation or by organ-specific ROIs. (a) illustrates the obtained VFA values for different patient sizes and tube voltage combinations. The insert in the thorax phantom is decomposed into water, CM (30 mg/mL iodine) and bone (400 mg/mL CaHA). (b) shows the volume fraction images of the three basis materials. Although the material images show visually no significant difference between the simulation-based and patient-specific calibration, a higher VFA is achieved using patient-specific calibrations of the basis materials.

Table 4.6: Resulting volume fraction depending on different calibrations and corresponding relative errors within ROI 1, 2 and 3. Each of these ROIs contains one of the three pure basis materials. The most accurate volume fractions and corresponding relative errors are written in bold.

	ROI 1	ROI 2	ROI 3	ROI 1	ROI 2	ROI 3
	f_{H_2O}	f_{CaHA}	f_I	e_{H_2O}	e_{CaHA}	e_I
		400 mg/mL	30 mg/mL			
GT	1.000	1.000	1.000	–	–	–
S						
Sim	0.961	0.927	0.858	3.94 %	7.28 %	14.21 %
PS	0.957	0.886	0.982	4.32 %	11.40 %	2.47 %
M						
Sim	0.964	0.883	0.781	3.65 %	11.65 %	21.91 %
PS	0.956	0.822	0.975	4.36 %	17.78 %	2.47 %
L						
Sim	0.971	0.822	0.775	2.88 %	17.78 %	22.52 %
PS	0.963	0.790	0.965	3.71 %	20.95 %	3.54 %

Table 4.7: Resulting volume fraction depending on different calibrations within ROI 4, 5, 6, 7, 8 and 9. Each of these ROIs contains an iodine mixture. The corresponding relative errors provides a measure for the iodine quantification accuracy using the proposed organ-adapted three material decomposition. The most accurate volume fractions and corresponding relative errors are written in bold.

ROI 4		ROI 5		ROI 6		ROI 7		ROI 8		ROI 9		
H ₂ O	I	H ₂ O	I	H ₂ O	I	H ₂ O	I	H ₂ O	I	H ₂ O	I	
2.5 mg/mL		5 mg/mL		10 mg/mL		15 mg/mL		20 mg/mL		25 mg/mL		
f_i												
GT	0.917	0.083	0.833	0.167	0.667	0.333	0.500	0.500	0.333	0.667	0.167	0.833
S												
Sim	0.914	0.046	0.828	0.113	0.658	0.261	0.497	0.399	0.345	0.555	0.182	0.681
PS	0.915	0.065	0.831	0.153	0.658	0.327	0.493	0.489	0.329	0.656	0.166	0.813
M												
Sim	0.914	0.046	0.835	0.104	0.658	0.226	0.513	0.362	0.315	0.497	0.194	0.624
PS	0.910	0.068	0.831	0.151	0.651	0.324	0.493	0.486	0.344	0.660	0.155	0.820
L												
Sim	0.919	0.046	0.845	0.106	0.662	0.222	0.525	0.336	0.317	0.426	0.233	0.598
PS	0.910	0.070	0.831	0.144	0.645	0.322	0.493	0.467	0.349	0.622	0.166	0.786
ϵ												$\bar{\epsilon}$
S												
Sim	0.29 %	45.10 %	0.68 %	32.40 %	1.27 %	21.64 %	0.55 %	20.28 %	3.51 %	16.81 %	9.22 %	18.33 %
PS	0.23 %	22.06 %	0.22 %	8.26 %	1.33 %	1.91 %	1.42 %	2.18 %	1.21 %	1.62 %	0.50 %	4.41 %
M												
Sim	0.29 %	48.34 %	0.15 %	37.42 %	1.32 %	32.08 %	2.60 %	27.52 %	5.48 %	25.48 %	16.12 %	25.16 %
PS	0.71 %	8.08 %	0.30 %	9.57 %	2.34 %	2.80 %	1.39 %	2.82 %	3.29 %	1.03 %	7.20 %	1.64 %
L												
Sim	0.25 %	44.98 %	1.40 %	36.50 %	0.66 %	33.27 %	4.93 %	32.80 %	4.89 %	36.03 %	39.66 %	28.28 %
PS	0.71 %	16.41 %	0.24 %	13.53 %	3.30 %	3.36 %	1.34 %	6.61 %	4.57 %	4.89 %	0.51 %	5.73 %

Table 4.8: Volume fraction accuracy corresponding to the basis materials H₂O and iodine within the iodinated vials. The *VFA* is calculated for the vials containing 2.5, 5, 10, 15, 20, 25 mg/mL. The highest *VFA* are written in bold.

<i>VFA</i>	80/140 kV+Sn				100/140 kV+Sn			
	Iodine		H ₂ O		Iodine		H ₂ O	
	Sim	PS	Sim	PS	Sim	PS	Sim	PS
S	74.24 %	93.58 %	97.41 %	99.18 %	69.22 %	91.45 %	97.89 %	99.32 %
M	67.33 %	94.01 %	96.04 %	97.10 %	58.10 %	86.04 %	95.66 %	99.32 %
L	64.69 %	91.28 %	91.42 %	98.17 %	58.48 %	87.08 %	90.14 %	98.27 %

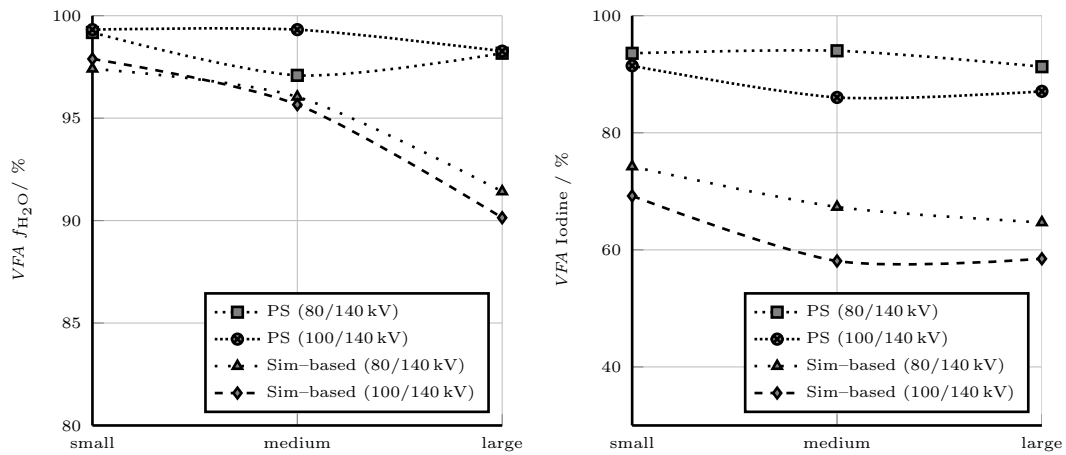
In order to assess the iodine quantification accuracy, the iodine and water fraction are evaluated in more detail. For this purpose, the *VFA* is determined for the vials containing 2.5, 5, 10, 15, 20, 25 mg/mL (Table 4.8). For all phantom thicknesses and tube voltage combinations, the *VFA* is significantly improved for the PS calibration. The obtained *VFA* for iodine is plotted in Figure 4.27b and the obtained *VFA* for water is plotted in Figure 4.27a. In the basis material simulation, the detected spectrum is not adapted to the actual phantom size and therefore the decomposition accuracy might be degraded. However, even if the phantom is small and there is no large discrepancy between simulation and truth, the PS calibration yields better results. With increasing patient sizes, it becomes more important to adapt the basis materials to the actual size of the patient. The phantom study suggests that on the one hand the adaptation of the basis materials on the patient size might be beneficial and on the other hand that the simultaneous measurement of a calibration phantom for different tissues, e.g. bone with preset CaHA content, might improve the decomposition results in patient data.

4.3.2 Material Decomposition Results

After having considered the results of the phantom study, the multi material decomposition of patient data will be presented. Since the patient data sets have been retrospectively selected for the evaluation of the multi material decomposition, no calibration phantom could be added during acquisition. The patient data was acquired using a third-generation dual source DECT system (SOMATOM Definition Force, Siemens Healthineers, Forchheim, Germany), where the tube voltage combination 70/150 kV+Sn (c.f. Table 3.3) was chosen. Ultravist[®] 370 (Bayer Vital, Leverkusen, Germany) was administered as contrast agent. Therefore, only the results obtained using a Sim calibration are shown in the following. The basis materials water and air are treated as fix points and set to 0 HU and -1000 HU, respectively. Since it is unknown how the CM distributes in the patient, the basis material of pure CM is selected. For this patient data, the administered pure CM consists of 370 mg/mL iodine. The basis material cortical bone is set to a predefined value of 500 mg/mL CaHA as it is typical for cortical bone in a young healthy adult.

Figure 4.28 shows the low and the high energy image of an abdominal DECT data which are used as input to the algorithm, as well as the seven obtained material frac-

4.3. QUANTITATIVE PSEUDO MULTI MATERIAL DECOMPOSITION



(a) Comparison of the iodine volume fraction accuracy depending on simulation-based or patient-specific calibration for different patient sizes and tube voltage combinations.

(b) Comparison of the water volume fraction accuracy depending on simulation-based or patient-specific calibration for different patient sizes and tube voltage combinations.

Figure 4.27: Evaluation of the decomposition accuracy by means of the volume fraction accuracy VFA (4.6) depending on different calibrations for three phantom sizes and two tube voltage combinations. The basis materials are either calibrated by simulation or by organ-specific ROIs. (a) illustrates the obtained VFA values for water. (b) shows the obtained VFA values for the iodine fraction.

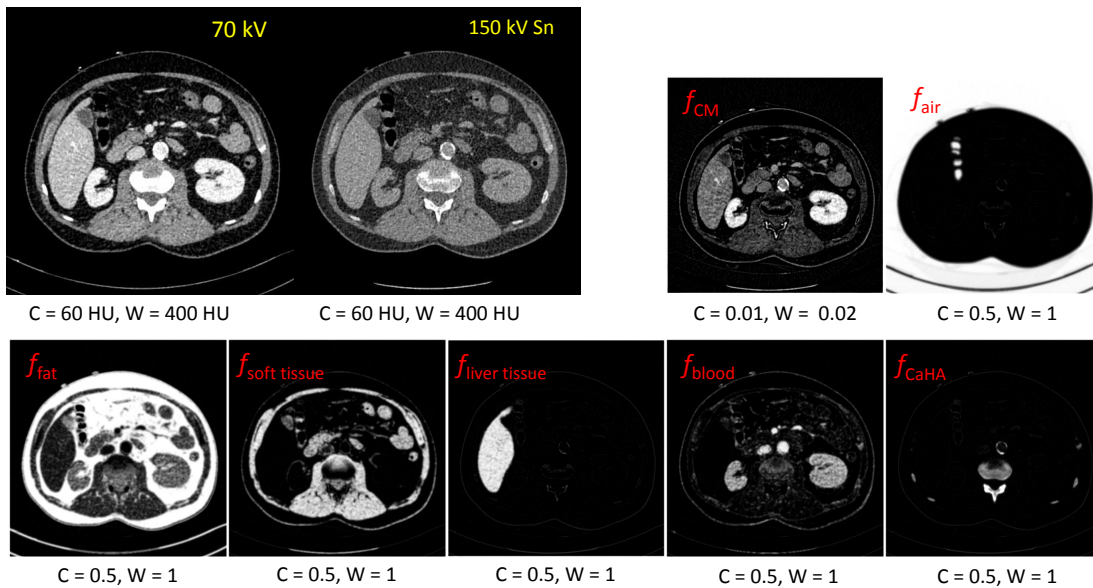


Figure 4.28: Decomposition of an abdominal DECT data set into its seven constituent materials. The low and the high energy images that are used as input are shown in the upper left (yellow annotations). The volume fraction of CM, air, fat, soft tissue, liver tissue, blood and bone are shown (red annotations). The bone is decomposed using the material triplet fat, blood and cortical bone. Except for CM, the volume fractions are displayed in the range between 0 and 1. In order to visualize the iodine distribution, a smaller range from 0 to 0.02 is chosen.

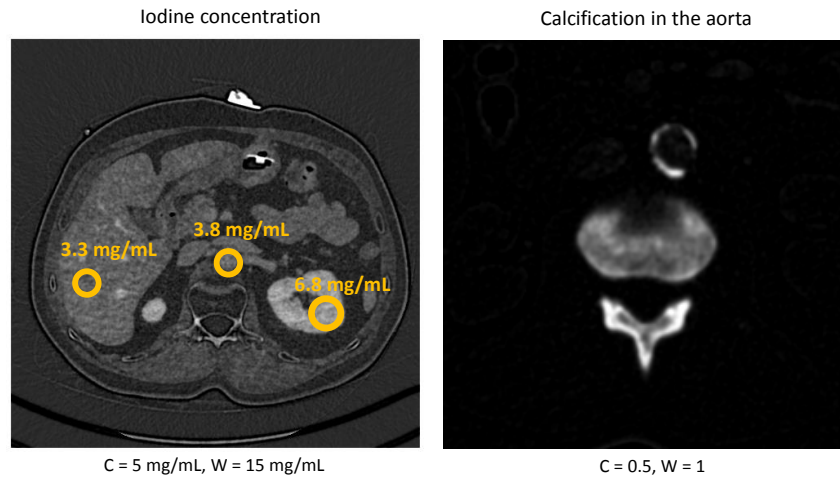


Figure 4.29: Quantitative and qualitative evaluation of the patient's composition using the pseudo multi material decomposition. The CM fraction can easily be converted to an iodine concentration. By evaluating small ROIs within the iodine map, the user obtains quantitative measurements of the local iodine distribution. The material triplet selection for the vascular system allows the qualitative detection of calcifications.

tion images. The basis material triplets are assigned according to Table 3.4. For the decomposition of bone, the material triplet fat, blood and cortical bone is selected. The volume fraction of CM is significantly lower than the other volume fractions, since the basis material CM itself is a dilution of iodine and water, which is further extremely diluted in the patient. Therefore, the CM fraction is presented using a different window level setting. According to Equation (3.39), the volume fraction is converted to a mass concentration of iodine in each voxel using $\gamma_{\text{iodine}} = f_{\text{CM}} \cdot 370 \text{ mg/mL}$. To make a quantitative statement of the local iodine distribution, ROIs can be evaluated by averaging the iodine uptake. Figure 4.29 illustrates the iodine map with the mass concentration in each voxel.

The value of the bone mineral density, i.e. the concentration of pure CaHA cannot be converted as easily, since the real concentration in the human body is unknown. Furthermore, the basis material triplet blood, CM and cortical bone, which is selected for the decomposition of the vascular system, enables the detection and visualization of calcifications. An example is shown in Figure 4.29. Moreover, the bone can alternatively be decomposed using the basis material triplet fat, CM and cortical bone as illustrated in Figure 4.30. This basis material selection also accounts for small iodine uptakes inside the bone and could provide an additional statement to the radiologists. Since the composition of the human body is not known exactly, the assumption that each voxel consists of three material components does not reflect the truth. However, both results could be presented in order to solve remaining ambiguities. The interpretation of the results remains to the radiologists.

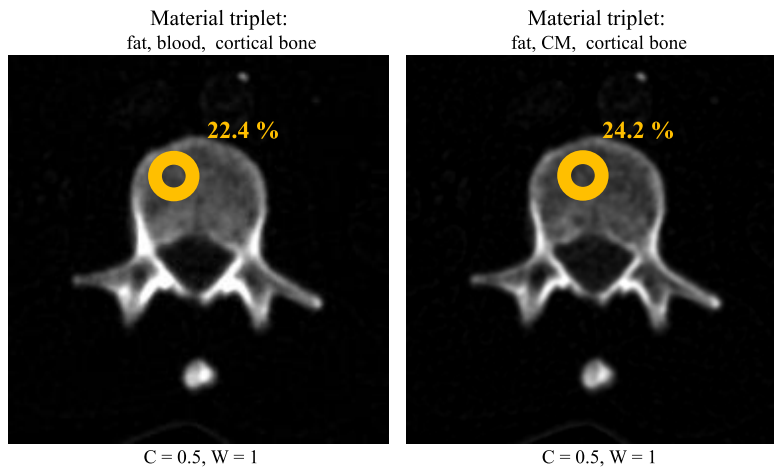


Figure 4.30: The left bone fraction is obtained using the material triplet fat, blood and cortical bone for decomposition. The right bone fraction is obtained using the material triplet fat, CM and cortical bone for decomposition. There is no significant difference in the volume fraction depending on the used material triplet.

4.3.3 Pie Charts and Material Scores

Since the number of basis images is significantly increased in the proposed method compared to two or three material decomposition for DECT data, the volume fractions can be presented to the radiologists in an alternative manner in order to improve diagnosis. Instead of presenting evermore material images to the radiologists, the material composition is visualized as a pie chart. As a first option, additionally to the conventional colored iodine or material maps, small ROIs and the corresponding material decomposition into its three basis materials are displayed (see Figure 4.31). The basis materials are selected depending on the location in the DECT data set. The volume fractions for each ROI are then visualized using organ-specific pie charts and coloring. The additional information yields material scores, for instance, the fat content in the liver (ROI 2) or bone (ROI 3). The fat content in the liver or bone or the soft tissue content in the lung might serve as an indicator and might be correlated with different diagnoses or might be used for treatment monitoring in clinical routine.

Alternatively, the user might be allowed to draw an arbitrary shaped ROI into the patient data instead of performing an exact delineation of a tumor boundary for example. Based on the anatomical priors, the ROIs might be separated into their tissue classes and decomposed into its related three basis materials. The results are presented as a selection of pie charts: for each tissue class, there is one chart highlighting its material composition. This data presentation is illustrated in Figure 4.32. In addition, the actual iodine concentration in the ROI is displayed for each tissue class in order to describe the local iodine distribution. In a repeated evaluation at different time points in a long term study, the same pie charts and values will be presented, since only the initial ROI shape and position needs to be stored.

Furthermore, it might be possible to provide a color overlay of the relative fat content in the liver comparable to the iodine overlay. In the case of different material triplets for one specific anatomical regions, the ambiguities might be solved by providing competing pie charts for one organ. The final decision on how the pie charts and volume fractions

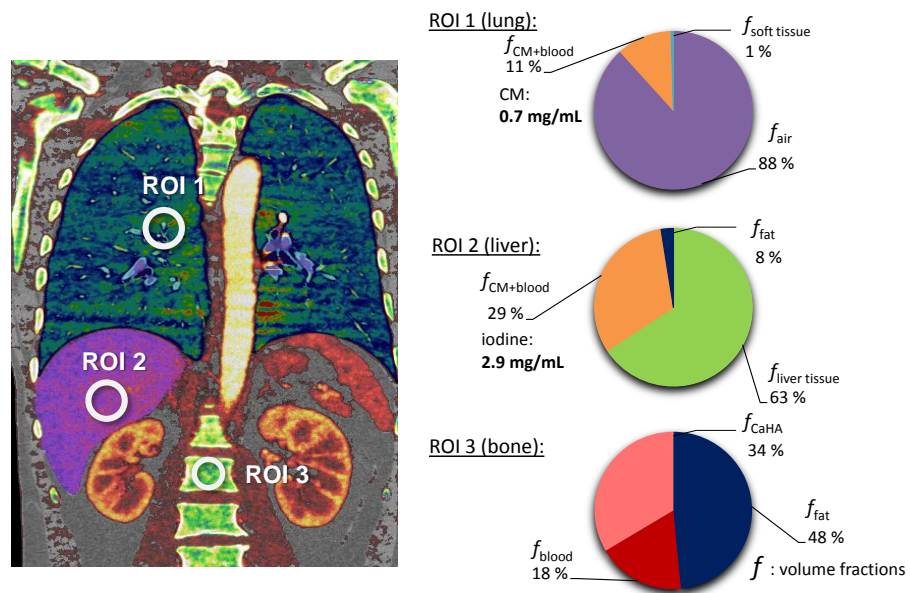


Figure 4.31: Pie chart visualization (option I) of the decomposition results. In addition to the conventional colored iodine or material maps, small ROIs are decomposed into its three basis materials. The basis materials are selected depending on the location in the DECT data set. The resulting volume fractions are visualized via a pie chart for each evaluated ROI.

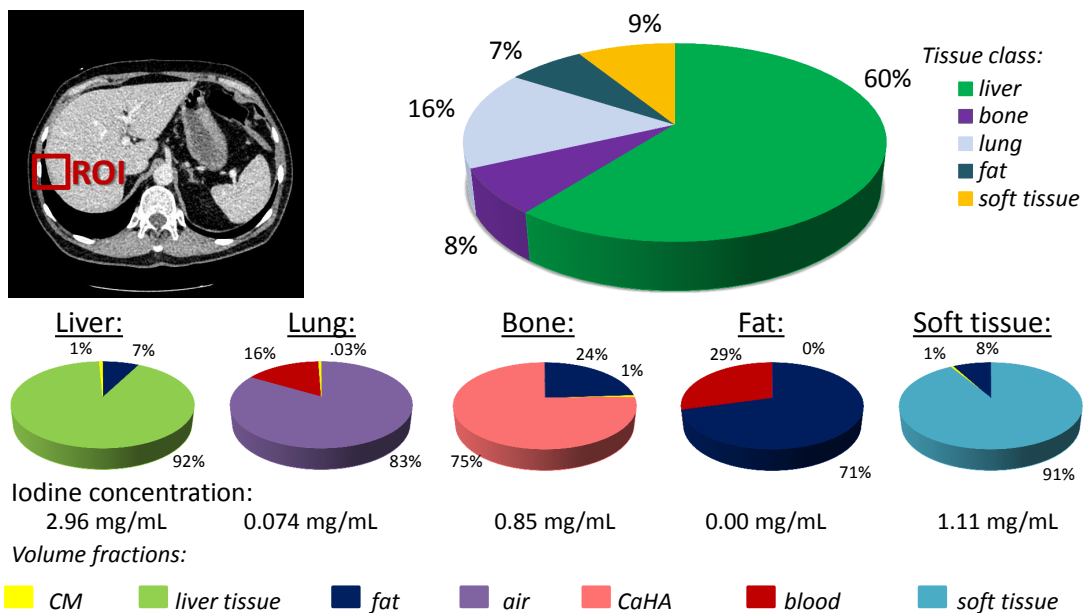


Figure 4.32: Pie chart visualization (option II) of the decomposition results. An arbitrary shaped ROI is evaluated and decomposed into its material components. The exact delineation of one specific anatomical structure is no longer necessary.

will be interpreted, will still rely on the radiologists.

CHAPTER 5

Discussion

The topic of this thesis is to examine the potential benefit of anatomical prior knowledge in the field of single, dual or even multi energy CT image formation, display and analysis. Therefore, an innovative imaging paradigm has been established in order to create novel opportunities that might improve today's clinical workflow. The proposed end-to-end pipeline consists of three main components:

- A context-sensitive CT image formation approach is presented, which combines competing image properties resulting from different reconstruction algorithms and display settings into a single context-sensitive imaging by exploiting anatomical prior information. Various desired image characteristics are fused into one image reconstruction and presentation. The principle of using prior knowledge to select specific organ-related reconstruction and display parameters is then extended to the evaluation of dual energy data.
- Numerous organ-specific DECT applications are integrated into one single analysis tool. A variety of conventional tools is automatically selected and invoked to different organs simultaneously by means of the CS information. Therefore, the proposed DECT scheme applies every feasible method at once instead of having to manually choose one DECT evaluation. Moreover, the prior knowledge is used to calibrate the patient- or organ-specific parameters directly from the patient data themselves in order to keep necessary user interactions at a minimum.
- A pseudo multi material decomposition in image domain is proposed that is able to decompose dual energy data into more than two or three material components. By exploiting the prior knowledge, the basis materials of organ-specific three material decompositions are selected in an organ-adaptive manner. The resulting volume fractions are converted to material scores and presented in a more sophisticated visualization in order to assist the radiologists during diagnosis.

All these methods and results have been validated by comparing them against established algorithms and results from the literature. In addition, potential clinical ap-

plications and limitations of the context-sensitive CT imaging for single, dual or multi energy data are illustrated.

5.1 Anatomical Prior Information

The anatomical prior knowledge enables the context-sensitive CT imaging. As a prerequisite, it is assumed that an automatic and accurate labeling of different anatomical regions in CT data is given by a reliable multi-organ segmentation. A figure of merit that is usually applied to quantify the accuracy of a segmentation is the Dice coefficient (Dice, 1945), which compares the similarity between the binary GT and the achieved segmentation by quantify the amount of overlap. A Dice coefficient of 100.0 % corresponds to an ideal match of the GT with the obtained segmentation and would be optimal. The best average Dice coefficients, which are obtained using the CNN approach proposed by Chen et al. (2018c), are 98 % for the right lung, 98 % for the left lung, 92 % for the liver, 90 % for the spleen, 94 % for the right kidney, 92 % for the left kidney, respectively. Compared to state-of-the-art multi-organ segmentations (Lavdas et al., 2017; Roth et al., 2017; Chen et al., 2017; Park et al., 2004; Okada et al., 2008; Wolz et al., 2013), the method provides reliable results.

However, the accuracy of the automatic segmentation approach is still limited by several factors. The segmentation can only be as good as the GT, which is delineated by clinical experts. If there are some errors in the GT, the automatic segmentation is not able to outperform this because it is a supervised learning technique. The robustness of the CNN output might be limited by the diversity of cases shown during training. For instance, if there are abnormalities or pathologies in the patient data which have not been presented to the network during training, the network will most likely fail to recognize them. Image noise or varying acquisition protocols might influence the accuracy of the trained network. Without any modification or retraining of the network, the correct organ boundaries might not be detected. The training of a CNN may be computational complex and is limited by the memory of current available GPUs. Moreover, the current CNN, as it has been used, is restricted to the automatic segmentation of six organs, i.e. the left and the right lung, the left and the right kidney, the spleen and the liver. More organs need to be delineated manually by medical experts to generate the associated GTs, which are required for the retraining of the network, in order to extend the segmentation to other anatomical regions. The more anatomical organs could be differentiated, the better. It should be noted that the automatic multi-organ segmentation will constantly be improved, since it is still a work in progress.

In this thesis, as mentioned above, an accurate and automatic multi-organ segmentation is assumed to be ready for use. This method reliably labels the CT data into different organs. The primary focus is therefore the presentation of the novel paradigm of the context-sensitive CT image formation, display and analysis and how CT imaging in general might benefit from an ideal segmentation. Therefore, the proposed context-sensitive imaging is not limited to this specific CNN approach. With the advent of more reliable methods in the future, the segmentation can obviously be substituted by more robust algorithms. Within the presented context-sensitive CT imaging pipeline, smooth

tissue-related weights are introduced in order to account for small inaccuracies of the current segmentation, since it is highly sensitive to the segmentation accuracy. In the case of an ideal segmentation, the tissue-related weights will no longer be necessary and can be replaced by the probabilistic output of the CNN.

5.2 Context-Sensitive CT Image Formation

Anatomical prior information offers considerable potential for novel improvements in CT imaging. By exploiting these priors, indication specific advantages of different settings are transferred into a context-sensitive image. It is possible to display each anatomical region with the clinically most appropriate reconstruction algorithm. In this thesis, different kernels are examined. The resulting adaptation of the spatial resolution and corresponding noise level depending on the anatomical region yields images with superior image impression. On a per-voxel basis, the most fitting basis image is selected for image composition. It combines therefore the advantages of competing reconstructions. It should be noted that each basis image is a quantitative CT image itself and therefore the combination of them does not degrade the CT values in any case. The resulting context-sensitive CT image is consequently also a quantitative CT image. Furthermore, within the context-sensitive, display the advantages of different window level settings are fused into one adaptive windowing. The remaining noise level in different anatomical structures can be further reduced by viewing specific organs in thicker slabs using an organ-adapted STS-Mean-IP. Moreover, an adaptive STS-MIP, e.g. of the lung with adapted slab thickness, can be simultaneously applied. Therefore, the number of images to display can be reduced to one context-sensitive image. As shown in the result section, the proposed organ-adaptive display method outperforms the conventional image presentation. The amount of simultaneously visible information is significantly increased, since it locally favors each anatomical structure by applying the best organ-adapted display settings. The proposed context-sensitive CT image formation and display yields high quality images achieving an improved image impression.

However, there is a notable parameter issue. In the context-sensitive image formation, there are two types of parametric choices that are to be considered. Conventional parameters have a significant influence on the CS image, its display and analysis. There are for instance the kernel, organ-related window level settings or slab thicknesses. Moreover, there are newly introduced parameters, which are required to actually perform the context-sensitive CT imaging. In order to calculate a context-sensitive resolution (CSR) image, an appropriate selection of the type or number of basis images and a corresponding organ assignment needs to be identified. The basis image can be reconstructed either analytically or iteratively. For instance, in analytic reconstruction, each possible convolution kernel results in varying image properties regarding the noise level and spatial resolution. Regarding the number of basis images, two kernels represent the absolute minimum number. However, it may happen that different users prefer to employ significantly more than two kernels. In a sophisticated implementation, only one single reconstruction is required to generate the basis images. By applying the shift invariant parts of the kernel to a single master image, another image can be calculated. Thus,

processing time is not an issue.

In particular, the width of the tissue-related has a strong impact on the resulting image. By adjusting the width, the size of the overlapping area between adjacent anatomical structures can be modified. A suitable selection of the transition width provides a qualitative superior image impression. Depending on the similarity of adjacent anatomical regions and the kernel to organ assignment, the width of the transition zone can dynamically be adapted. Furthermore, the window level settings for each organ, the blending width of adjacent windows, the organ-specific sliding thin slab (STS) techniques as well as the corresponding slab thicknesses for each anatomical region have to be determined. Besides the presented context-sensitive display approaches, the principle could also be extended to any other display technique. Furthermore, since some organ-specific window level settings are more similar to adjacent windows than others, the weights could also be varied across different anatomical structures using adaptive transition zone widths. The default parameter selection, which has been proposed in this thesis, could be considered as a recommendation. Starting from this parameter set, the CT image can be displayed to the radiologists. At any point, the parameters are freely adjustable.

In summary, the proposed CS image formation and display delivers an alternative to the common presentation of multiple different CT images.

5.3 Context-Sensitive Dual Energy

An important step to perform a case-adapted DECT diagnosis is to identify useful applications which add functional or material information to the conventional quantitative CT image. Therefore, the radiologists need to decide which DECT evaluation method should be applied to which organ. For some anatomical regions, e.g. bone, more than one DECT evaluation (*Bone Marrow* vs. *Bone Removal*) is reasonable and therefore a decision needs to be made. In consultations with radiologists and medical experts as well as by comprehensively reviewing state-of-the-art literature on dual energy evaluation methods, e.g. McCollough et al. (2015); Johnson et al. (2007); Johnson (2012), reasonable DECT analyses have been identified. In a clinical environment, each possible application is invoked to the corresponding specific anatomical region in order to identify possible pathologies. In this thesis, the selected evaluation scheme may serve as a proposal on specific applications. In clinical routine, the choice can be adapted on the clinical indication.

In phantom measurements, it could be shown that the adaptation of the contrast media ratio significantly improves the iodine quantification accuracy towards the ground truth values. The default parameter setting tends to underestimate the true iodine concentration, since it neglects beam hardening and scatter. However, since the actual iodine concentration in patient measurements is unknown, there is no absolute statement on the behavior of the RelCM value on the quantification accuracy of the iodine content. Nevertheless, an evaluation of a patient-specific calibration in patient data indicates that the obtained iodine concentrations increases significantly compared to default parameters. It can therefore be concluded that a patient-specific calibration improves

the quantification accuracy by taking beam hardening and scatter effects into account. In conclusion, the iodine quantification accuracy showed a conceivable improvement by performing a patient-specific calibration of the relative iodine contrast, since the actual patient size has been taken into account adequately. The default calibration neglects the actual patient size. Therefore, the automatic prior-based DE calibration yields more accurate material decompositions and classifications.

A simultaneous evaluation and analysis scheme for various DECT applications is proposed that combines the advantages of available DECT applications by means of prior knowledge. The novel context-sensitive DECT tool is able to perform a comprehensive evaluation of many different anatomical regions simultaneously without the need of any user-interaction. Exploiting the available anatomical information enables to automatically calibrate, select and apply an organ-dependent DECT evaluation method to patient data. The resulting context-sensitive DECT image assigns the spectral information as an additional dimension by highlighting each single contribution of different material decompositions and classifications. The various material maps may be displayed as color overlay onto a conventional CT image or onto a CS image.

5.4 Quantitative Pseudo Multi Material Decomposition

The proposed quantitative pseudo multi material decomposition is able to decompose phantom and patient data into more than three basis materials. By means of anatomical prior knowledge, the basis materials are adapted to the anatomical region. Each organ or tissue type is exactly assigned to one decomposition triangle. The materials are therefore decomposed into their material compounds according to the anatomical structure they belong to. Compared to the tessellation approach proposed by Mendonça et al. (2014), the proposed pseudo multi material decomposition shows robust decomposition results. The prior work results in ambiguities in the decomposition due to an erroneous basis material selection. Mendonça et al. (2014) proposed to assign the voxel to be decomposed to one basis material triplet based on the location of the voxel in the DE space. Due to noise, the voxel might be assigned to adjacent triangles resulting in misleading basis material contributions. First attempts to overcome the reported limitations are proposed by Kuchenbecker et al. (2015). The authors included a naive segmentation step prior to decomposition in order to improve the material decomposition into more than three basis materials. The data set is segmented in five tissue types, i.e. air, fatty tissue, soft tissue, (dense and) enhanced tissue, bone and dense bone, based on their CT values using a simple thresholding approach. Although the initial segmentation step reduced the ambiguities in the material decomposition, there are still inaccurate tissue classifications, since different tissues might show similar CT values.

In the proposed method, the assignment of the basis materials based on anatomical priors assures a physical appropriate basis material selection such that crosstalks in the material images are minimized. In order to further reduce material crosstalks, each anatomical region is evaluated independently from each other. The achieved volume fractions are then combined to compose seven basis material images. Overall, the proposed multi material decomposition performs all three material decompositions at once.

The number of basis materials and predefined triplets is not limited to a specific number and can be extended on demand. If further anatomical structures may be distinguished in the future, associated basis material triplets can be defined for the multi material decomposition.

Furthermore, the proposed approach enables the quantification of the iodine content in each voxel and potentially facilitates the detection of calcifications in the vascular system. For instance, a calcification of the aorta is also apparent in the volume fraction of the basis material image of cortical bone, since the aorta is decomposed using the basis material triplet blood–cortical bone–iodine. A quantitative evaluation of the material compound, particularly for the quantification of the bone mineral density (BMD), is not as straightforward, since the real concentration of pure CaHA in the human body remains unknown and no calibration measurement is available for the patient data. In clinical routine, bone mineral density measurements as well as the quantification of the iodine concentration are performed routinely. However, *Acu et al. (2014)*; *Pompe et al. (2015)* showed that the presence of contrast media has a significant influence on the bone mineral density assessment. There is a considerable increase in the measured bone mineral density due to the increase of the CT values resulting from the CM injection. In this work, the proposed pseudo multi material decomposition yields a simultaneous decomposition into the volume fractions iodine and cortical bone and is therefore able to reduce the shifts in the bone mineral density measurement. As illustrated in *Figure 4.30*, two different basis material selections for the decomposition of bone both result in robust volume fractions for cortical bone. Even if there is contrast media assumed to be inside the bone, the resulting volume fractions are accurately determined. The conversion to a virtual bone mineral density by multiplying with the known basis material density yields similar bone mineral density values. In conventional DECT approaches, the fat quantification of liver tissue requires a native scan, since the contrast media uptake degrades the fat content quantification. The proposed pseudo material decomposition is able to determine a quantitative value of the fat also in the presence of CM. The novel algorithm allows therefore the quantification of liver fat content as well as the iodine quantification simultaneously.

The evaluation of different strategies to calibrate the basis materials, i.e. simulation–based versus patient–specific, showed that the volume fraction accuracy increased by applying a patient–specific basis material calibration by 33% for CM and by 4% for water on average. However, the number of possible basis materials is reduced, since it is not feasible to differentiate between liver tissue, soft tissue and blood in a contrast–enhanced scan. In order to improve the volume fraction accuracy independently of the basis material calibration, a denoising technique might be integrated into the decomposition process (*Long and Fessler, 2014*; *Xue et al., 2017*). However, the inclusion of this will increase the complexity of the decomposition algorithm. In this thesis, a direct inversion of the linear system of equations is applied to solve for the volume fractions. This simple yet effective approach proves the feasibility and benefit of the proposed application of organ–adapted three material decompositions.

The pseudo multi material decomposition yields volume fractions that bear the potential to improve the material quantification for diagnosis, particularly to evaluate the

vascularization of tumors. In order to assist the radiologist, the volume fractions can be visualized using pie charts. This visualization can facilitate the interpretation of the volume fractions and might improve diagnosis. Moreover, it might be beneficial to show the segmentation and the assigned basis material triplets to the radiologist. The additional “tissue map” will indicate which basis material triplet has been selected for each anatomical organ to assist in the interpretation of the results. Furthermore, the information might support the radiologist to identify areas of non-negative basis material fractions since the space of resulting volume fractions is sparse by definition.

5.5 Outlook

In this thesis, a proof of concept is provided in order to point out the feasibility of the novel imaging paradigm and potential advantage of CS imaging in general. At this time, the veritable diagnostic reliability of the CS images has not yet been clinically evaluated and therefore the technology has not been installed in clinical routine yet. Consequently, the radiologists are not aware of them. A graphical user interface (GUI), i.e. an interactive image viewer, is therefore needed in order to provide and install the novel imaging paradigm in the hospitals to pave the way for an extensive clinical study. The image viewer should contain the novel methodology as well as the variety of the most popular functionalities. For each organ individually, the parameter settings of the CS imaging can be customized via the GUI. The window level settings for one specific organ can thus be selected separately by the user, while the window level settings for the other organs remain unchanged. The GUI will permit the radiologists to experience the CS imaging and enable to interactively modify various parameters as needed. A comprehensive clinical evaluation study in order to investigate the diagnostic potential of the proposed CS imaging method will be conducted in future work. If the benefit of the novel imaging paradigm has been proven to be superior compared to conventional CT imaging, the presented methodology might be integrated into clinical routine. Besides the conventional CT imaging, the novel CS imaging could be employed to gain additional value for diagnostic imaging. This might be the first step to simplify and accelerate diagnoses in order to improve the clinical workflow and provide a faster and more precise diagnosis for the patient.

The method offers potential to be used for multi energy CT data or other modalities by transferring the imaging paradigm. In case of multi energy data, the different images resulting from different energy bins show different image characteristics. For instance, the high energy image contains less soft tissue contrast but also less beam hardening artifacts or metal artifacts. The bin image associated with a lower energy shows a high soft tissue contrast but image artifacts instead. Moreover, the SOMATOM Definition CounT using the sharp mode acquires multi energy data with a varying spatial resolution for different energies. Depending on the anatomical structure, these images can therefore be blended such that an optimal organ-specific multi energy mixed image is obtained. In case of MRI imaging, there is a large amount of different imaging sequences required which enforces different tissue contrasts. These competing image sequences can be merged comparable to the blending of different CT image reconstructions.

In multi modality imaging, i.e. PET/MRI or PET/CT imaging, an automatic detection and localization of metastasis and tumors could be performed. PET imaging is a functional imaging modality, where no anatomical information is visible. Based on the automatic segmentation of the MRI or CT data, regions of high activity could be located within specific anatomical regions to detect abnormalities. By means of the automatic segmentation, the anatomy can be transferred from one imaging modality to another. Instead of simply fusing both images and display a color coded heat map of the activity, the tumors and pathologies could be located and potentially classified by means of the multi-organ segmentation. Therefore, an automatic localization and classification of pathologies could be used to assist during treatment planning, for instance.

With the advent of more powerful GPUs and more sophisticated machine learning algorithms, e.g. CNNs, in the future, it will be only a matter of time until a reliable, robust and fast segmentation method will be available. As soon as such a fast and ideal segmentation is available, any kind of data can be processed in a context-sensitive manner.

CHAPTER 6

Summary

In clinical routine, a case-adapted CT examination is usually conducted for each medical indication in order to allow for a comprehensive high-quality diagnosis of a patient. Therefore, image reading requires the transition between various image stacks, since each medical question implicitly requires organ-dependent reconstructions, display settings, multiplanar reformations and image analysis tools. In particular, if dual or multi energy CT data are available, various spectral evaluation methods yield material-specific or functional information. However, the interpretation of this large amount of data is a time-consuming and tedious task. Hence, the purpose of this thesis is to evaluate the potential benefit of the incorporation of patient-specific anatomical priors, which are gained from an automatic multi-organ segmentation, in order to discover novel opportunities to improve the clinical workflow.

In this thesis, a new paradigm is proposed which combines competing image properties resulting from different reconstruction algorithms and display settings into a context-sensitive CT imaging by means of anatomical prior information. With the incorporation of anatomical prior knowledge, which is obtained using an automatic multi-organ segmentation approach, various desired image characteristics are combined into a single context-sensitive CT image formation and presentation. The comparison with conventional CT images reveals an improved spatial resolution in highly attenuating materials as well as in air-filled body regions. Simultaneously, the compound image maintains a low noise level in soft tissue resulting in a superior soft tissue contrast compared to conventional images. Furthermore, the novel CT imaging framework allows for the combination of mutually exclusive display settings for the presentation of context-sensitive images to the radiologists. By exploiting anatomical prior information, numerous DECT applications can be integrated into one single DE analysis tool. Moreover, the tools can be chosen and applied to different organs simultaneously without any user interaction. The prior-based DE scheme performs all organ-specific feasible methods instantaneously without the need of a manual selection. Exploiting the anatomical priors, DECT analysis and evaluations are automated and standardized. The iodine quantification accuracy is significantly improved using patient-specific calibrations. The evaluation method and

the presentation of the data to the radiologist can be realized via color overlays, pop up menus, volume rendering etc. Furthermore, the method can readily be generalized to the cases of multi energy CT data as it is not limited to the processing of DECT data.

The principle of incorporation anatomical prior knowledge is then extended to provide a novel pseudo material decomposition that decomposes dual energy data into more than three basis materials. The method consists of multiple three-material decompositions, where the basis materials are automatically adjusted to the organ of interest based on the automatic segmentation. Moreover, a patient-specific calibration is introduced to improve the volume fraction and material quantification accuracy. An organ-adapted basis material triplet is automatically assigned to each anatomical region resulting in overlapping triangles in the dual energy space. The basis materials are calibrated by evaluating ROIs to improve the volume fraction accuracy. Besides presenting evermore increasing material images to the radiologists, the volume fractions are rescaled to organ-dependent material scores and visualized via pie charts to be later correlated with different diagnoses. The prior-based pseudo multi material decomposition is evaluated using phantom and patient data. The materials are quantified according to the anatomical structure they belong to. Overall, the proposed method provides physically plausible volume fractions that bear the potential to improve the material quantification for diagnosis and e.g. tumor treatment monitoring.

In addition, the iodine quantification accuracy and the volume fraction accuracy are evaluated depending on different material calibration methods in conventional DECT applications as well as in the novel pseudo multi material decomposition. The accuracy using default parameters or simulation-based calibrations is compared against the accuracy obtained using patient-specific ROIs. All patient-specific calibrations can be performed directly from the patient data themselves, such that almost no user interaction is required. It turns out that a patient-specific calibration is superior compared to a default or simulation based calibration.

The new paradigm offers the possibility to display evermore complex information in CT imaging in order to significantly improve the workflow of radiologists. In the clinical routine, e.g. during case presentations and discussions, the fast switching between different image stacks is time-consuming and can be avoided in the future since the CS images merge advantageous image properties resulting from various reconstructions and display settings. The results of the DE evaluation can be dynamically superimposed by color overlays. This superposition provides a comprehensive quantitative analysis of the patient data that can be interpreted as an additional image dimension. By means of the combined DECT evaluation scheme, the radiologists might be assisted in finding a precise diagnosis. In summary, diagnostic accuracy could be increased with the CS imaging by improving the sensitivity for incidental findings: e.g. small nodules can be diagnosed in the lung parenchyma, even if the radiologist is mainly focused on assessing soft tissue. The possibility to robustly decompose DECT data into more than three basis materials opens up for novel clinical evaluation to quantify e.g. fat content and iodine content in the liver simultaneously and to assess long term material scores using pie chart visualizations.

Zusammenfassung

Kontextsensitive CT–Bildgebung

Im klinischen Alltag gibt es eine Vielzahl von verschiedenen Rekonstruktionsverfahren zur Bildentstehung sowie viele konkurrierende Bilddarstellungen und Analysewerkzeuge, die zur Befundung von CT–Daten genutzt werden. In der Regel wird für jede medizinische Indikation eine fallspezifische CT–Untersuchung durchgeführt, um eine umfassende und qualitativ hochwertige Diagnose für den Patienten sicherzustellen. Daher ist in der radiologischen Diagnostik der Wechsel zwischen verschiedenen CT–Volumina und Darstellungsarten unumgänglich. In dieser Arbeit wird nun ein neues Paradigma vorgeschlagen, welches konkurrierende Bildeigenschaften und Darstellungsmethoden in eine kontextsensitive CT–Bildgebung kombiniert. Die Ausnutzung anatomischer Vorinformation, die durch eine automatische Multiorgan–Segmentierung gewonnen wurde, ermöglicht die Kombination von gewünschten Bildmerkmalen in eine neuartige kontextsensitive CT–Bildentstehung und Präsentation. Der Vergleich mit herkömmlichen CT–Bildern zeigt eine verbesserte räumliche Auflösung sowohl bei stark schwächenden Materialien als auch innerhalb der Lunge sowie ein niedriges Bildrauschen im Weichgewebe. Die neuartige kontextsensitive CT–Bildgebung ermöglicht zudem die Kombination verschiedener Darstellungsarten wie beispielsweise organspezifische Fensterungen, die Darstellung dickerer Schichten im Gewebe oder die Anwendung von organabhängigen „MIP“s. Das neue Paradigma ist ein möglicher Schritt, immer komplexere Informationen in der CT–Bildgebung zu präsentieren und damit den Arbeitsablauf der Radiologen deutlich zu verbessern. Bei Falldiskussionen kann das Umschalten zwischen verschiedenen Bildstapeln entfallen, da das kontextsensitive Bild die Vorteile unterschiedlicher Rekonstruktionen und Darstellungseinstellungen kombiniert. Das neue Paradigma könnte daher zukünftig die diagnostische Genauigkeit erhöhen, indem es die Sensitivität für zufällige Befunde verbessert: z.B. könnten kleine Knoten im Lungenparenchym diagnostiziert werden, auch wenn das Augenmerk des Radiologen auf der Beurteilung des Gewebes liegt.

Kontextsensitive Zweispektren-CT-Anwendung

Um die diagnostische Aussagekraft gegenüber herkömmlichen CT-Messungen weiter erheblich zu verbessern, haben sich in den letzten Jahren dedizierte Zweispektren-CT Systeme im klinischen Alltag etabliert. Ein zukunftssträchtiges Anwendungsgebiet der Zweispektren-CT ist beispielsweise die Therapieüberwachung bei Tumorpatienten. Mithilfe der Jodaufnahme eines Tumors als Surrogatparameter für die Durchblutung kann das Ansprechen der Therapie genauer und frühzeitiger als mit rein morphologischen Verfahren bestimmt werden. Jedoch beschränken sich die Auswertungen auf einen bestimmten Körperbereich und die Anwendungen sind auf organspezifische Parametrierung ausgelegt. Ziel der vorliegenden Dissertation ist es, durch anatomisches Vorwissen diese Verfahren zu automatisieren und damit zu standardisieren. Derzeitige Verfahren nutzen keine anatomische Vorinformation und beschränken sich lediglich auf grobe Voreinstellungen von Parametern in Form von Schwellwerten oder Kontrastunterschieden. Mithilfe von anatomischer Vorinformation werden nun zahlreiche Zweispektrenanwendungen zu einem einzigen Werkzeug kombiniert. Kontextsensitive Materialzerlegungen und Materialklassifizierungen werden automatisch ausgewählt und gleichzeitig auf die verschiedenen Organe angewendet. Anstatt nur eine einzelne manuell ausgewählte Auswertung zu haben, führt das vorgestellte Auswertungsschema alle organspezifischen, realisierbaren Methoden auf einmal durch. Weiterhin wird die Genauigkeit der Jodquantifizierung durch eine patientenbezogene Kalibrierung deutlich verbessert. Ergebnisse der Auswertungen können dem Radiologen nun in Form von Farbüberlagerungen, Popup-Menüs, etc. zur Verfügung gestellt werden. Die Kombination verschiedener Applikationen kann den Radiologen unterstützen, eine genaue Diagnose zu finden. Das Verfahren ist nicht auf Zweispektrendaten beschränkt und kann leicht auf Mehrspektren-CT-Daten verallgemeinert werden.

Kontextsensitive Mehrmaterialzerlegung

Unter der Annahme, dass jeder Voxel aus drei Materialien besteht und sich die Volumenanteile dieser drei Materialien zu eins addieren, erhält man eine dritte Gleichung und kann die Anteile dieser drei Materialien berechnen und im CT-Bild darstellen. Als Beispiel für eine Dreimaterialzerlegung ist die virtuelle Nativbildgebung zu nennen, bei der der Jodanteil innerhalb eines kontrastierten Gefäßes oder Organ rechnerisch entfernt wird. Damit kann auf eine zusätzliche Untersuchung ohne Kontrastmittel verzichtet und damit die Patientendosis signifikant reduziert werden. Jedoch repräsentieren die drei vordefinierte Basismaterialien nicht alle anatomischen Strukturen. Beispielsweise kann Knochen nicht mit den Basismaterialien Fett, Blut und Iod adäquat dargestellt werden. In dieser Arbeit wird eine Erweiterung des Verfahrens vorgestellt, welche die Basismaterialien der Zerlegung abhängig vom Ort so wählt, dass zum Beispiel im Knochen andere Basismaterialien gewählt werden als in der Leber. Durch die Ausnutzung von Vorwissen aus der automatischen Mehrorgansegmentierung werden existierende Mehrdeutigkeiten in herkömmlichen Materialzerlegungen reduziert und eine robustere Zerlegung in mehr als drei Basismaterialien erzielt. Der im Rahmen der Dissertation entwickelte Materialzerlegungsalgorithmus wird aufgrund des diagnostischen Wertes in geeigneter Form

dem Radiologen zur Verfügung gestellt. Innerhalb einer manuell platzierten ROI wird die selektive Auswertung der Materialien automatisch durchgeführt und die einzelnen Basismaterialanteile in einem Tortendiagramm visualisiert. Diese Visualisierungsart der Volumenanteile der Basismaterialien ermöglicht dem Radiologen die Quantifizierung einzelner Bestandteile innerhalb der ROI. Die Mehrinformation kann genutzt werden, um den Verlauf einer Tumorthherapie zu beobachten, indem man in die Materialien Luft, Weichteil/Wasser, Knochen/Kalzium und Fett trennt. Ein Anstieg des Luftkompartiments würde dann zum Beispiel das Auftreten einer Entzündung anzeigen, wohingegen der Anstieg des Wasseranteils auf eine Nekrose hinweisen würde.

Bibliography

- Achenbach, S., Ropers, D., Kuettner, A., Flohr, T., Ohnesorge, B., Bruder, H., Theessen, H., Karakaya, M., Daniel, W. G., Bautz, W., Kalender, W. A., and Anders, K. Contrast-enhanced coronary artery visualization by dual-source computed tomography — initial experience. *European Journal of Radiology*, 57(3):331–335, 2006.
- Acu, K., Scheel, M., and Issever, A. S. Time dependency of bone density estimation from computed tomography with intravenous contrast agent administration. *Osteoporosis International*, 25:535–542, February 2014. ISSN 1433-2965. doi: 10.1007/s00198-013-2440-4.
- Almeida, I. P., Schyns, L. E. J. R., Öllers, M. C., van Elmpt, W., Parodi, K., Landry, G., and Verhaegen, F. Dual-energy CT quantitative imaging: a comparison study between twin-beam and dual-source CT scanners. *Med. Phys.*, 44:171–179, January 2017. ISSN 2473-4209. doi: 10.1002/mp.12000.
- Alvarez, R. E. and Macovski, A. Energy-selective reconstructions in x-ray computerized tomography. *Phys. Med. Biol.*, 21:733–744, September 1976. ISSN 0031-9155.
- Attix, F. H. *Introduction to Radiological Physics and Radiation Dosimetry*. Wiley, 1987.
- Boll, D. T., Patil, N. A., Paulson, E. K., Merkle, E. M., Simmons, W. N., Pierre, S. A., and Preminger, G. M. Renal stone assessment with dual-energy multidetector CT and advanced postprocessing techniques: Improved characterization of renal stone composition — pilot study. *Radiology*, 250(3):813–820, 2009. doi: 10.1148/radiol.2503080545. PMID: 19244048.
- Brooks, R. A. A quantitative theory of the Hounsfield unit and its application to dual energy scanning. *Journal of Computer Assisted Tomography*, 1:487–493, October 1977. ISSN 0363-8715.
- Buzug, T. M. *Fundamentals of X-ray Physics*, pages 15–73. Springer Berlin Heidelberg, Berlin, Heidelberg, 2008. ISBN 978-3-540-39408-2. doi: 10.1007/978-3-540-39408-2_2.
- Chandra, N. and Langan, D. A. Gemstone detector: Dual energy imaging via fast kVp switching. In Johnson, T. R., Fink, C., Schönberg, S., and Reiser, M. F., editors, *Dual Energy CT in Clinical Practice*, pages 34–41. Springer-Verlag Berlin Heidelberg, 2011.
- Chen, S., Endres, J., Dorn, S., Maier, J., Lell, M., Kachelrieß, M., and Maier, A. *A Feasibility Study of Automatic Multi-Organ Segmentation Using Probabilistic Atlas*,

- pages 218–223. Springer Berlin Heidelberg, Berlin, Heidelberg, 2017. ISBN 978-3-662-54345-0. doi: 10.1007/978-3-662-54345-0_50.
- Chen, S., Roth, H., Dorn, S., May, M., Cavallaro, A., Lell, M., Kachelrieß, M., Oda, H., Mori, K., and Maier, A. Towards automatic abdominal multi-organ segmentation in dual energy CT using cascaded 3D fully convolutional network. In *Proceedings of the Fifth International Conference on Image Formation in X-Ray Computed Tomography*, pages 395–398, 2018a.
- Chen, S., Zhong, X., Hu, S., Dorn, S., Kachelrieß, M., Lell, M., and Maier, A. Automatic multi-organ segmentation in dual energy CT using 3D fully convolutional network. In *1st Conference on Medical Imaging with Deep Learning (MIDL 2018)*, 2018b.
- Chen, S., Zhong, X., Hu, S., Dorn, S., Kachelrieß, M., Lell, M., and Maier, A. Automatic multi-organ segmentation in dual energy CT (DECT) with dedicated 3D fully convolutional DECT networks. *Med. Phys. Submission*, 2018c.
- Choi, H. K., Al-Arfaj, A. M., Eftekhari, A., Munk, P. L., Shojania, K., Reid, G., and Nicolaou, S. Dual energy computed tomography in tophaceous gout. *Annals of the Rheumatic Diseases*, 68(10):1609–1612, 2009. ISSN 0003-4967. doi: 10.1136/ard.2008.099713.
- Çiçek, Ö., Abdulkadir, A., Lienkamp, S. S., Brox, T., and Ronneberger, O. 3D U-net: learning dense volumetric segmentation from sparse annotation. In Ourselin, S., Joskowicz, L., Sabuncu, M. R., Unal, G., and Wells, W., editors, *Medical Image Computing and Computer-Assisted Intervention – MICCAI 2016*, pages 424–432, Cham, 2016. Springer International Publishing. ISBN 978-3-319-46723-8.
- Cierniak, R. *X-ray Computed Tomography in Biomedical Engineering*. Springer, London, 2011. doi: 10.1007/978-0-85729-027-4.
- Coleman, A. J. and Sinclair, M. A beam-hardening correction using dual-energy computed tomography. *Phys. Med. Biol.*, 30:1251–1256, November 1985. ISSN 0031-9155.
- Cormack, A. M. Representation of a function by its line integrals, with some radiological applications. *Journal of Applied Physics*, 34(9):2722–2727, 1963.
- Cormack, A. M. Representation of a function by its line integrals, with some radiological applications II. *Journal of Applied Physics*, 35(10):2908–2913, 1964.
- Cullen, D. E., Perkins, S., and Rathkopf, J. The 1989 Livermore evaluated photon data library (EPDL). Technical report, March 1990.
- Cullen, D. E., Hubbell, J. H., and Kissel, L. EPDL97: the evaluated photon data library. In *UCRL-50400*, volume 6.5, pages 1–28, March 1997.
- Davis, K. R., New, P. F., Solis, O. J., and Roberson, G. H. Theoretical considerations in the use of contrast media for computed cranial tomography. *Revista Interamericana de Radiologia*, 1:9–12, October 1976. ISSN 0034-9704.

- Dice, L. R. Measures of the amount of ecologic association between species. *Ecology*, 26 (3):297–302, 1945. doi: <https://doi.org/10.2307/1932409>.
- Dorn, S., Chen, S., Sawall, S., Maier, J., Knaup, M., Maier, A., Lell, M., and Kachelrieß, M. Prior-based multi material decomposition (PBMMD) for dual energy CT. In *Proceedings of the Fifth International Conference on Image Formation in X-Ray Computed Tomography*, pages 106–109, 2018a.
- Dorn, S., Chen, S., Sawall, S., Maier, J., Knaup, M., Uhrig, M., Schlemmer, H.-P., Maier, A., Lell, M., and Kachelrieß, M. Towards context-sensitive CT imaging — organ-specific image formation for single (SECT) and dual energy computed tomography (DECT). *Med. Phys.*, 45:4541–4557, October 2018b. ISSN 2473-4209. doi: 10.1002/mp.13127.
- Dorn, S., Chen, S., Sawall, S., Simons, D., May, M., Maier, J., Knaup, M., Schlemmer, H.-P., Maier, A., Lell, M., and Kachelrieß, M. Organ-specific context-sensitive CT image reconstruction and display. In *Proc. SPIE 10573, Medical Imaging 2018: Physics of Medical Imaging*, 2018c. doi: 10.1117/12.2291897.
- Ertl-Wagner, B., Bruening, R., Blume, J., Hoffmann, R.-T., Mueller-Schunk, S., Snyder, B., and Reiser, M. Relative value of sliding-thin-slab multiplanar reformations and sliding-thin-slab maximum intensity projections as reformatting techniques in multisection CT angiography of the cervicocranial vessels. *American Journal of Neuroradiology*, 27(1):107–113, 2006. ISSN 0195-6108.
- Euler, A., Parakh, A., Falkowski, A. L., Manneck, S., Dashti, D., Krauss, B., Szucs-Farkas, Z., and Schindera, S. T. Initial results of a single-source dual-energy computed tomography technique using a split-filter: Assessment of image quality, radiation dose, and accuracy of dual-energy applications in an in vitro and in vivo study. *Investigative Radiology*, 51:491–498, August 2016. ISSN 1536-0210. doi: 10.1097/RLI.0000000000000257.
- Evans, R. D. and Evans, R. The atomic nucleus. 1955.
- Faby, S., Kuchenbecker, S., Sawall, S., Simons, D., Schlemmer, H.-P., Lell, M., and Kachelrieß, M. Performance of today’s dual energy CT and future multi energy CT in virtual non-contrast imaging and in iodine quantification: A simulation study. *Med. Phys.*, 42(7):4349–4366, 2015.
- Fahmi, R., Eck, B. L., Levi, J., Fares, A., Dhanantwari, A., Vembar, M., Bezerra, H. G., and Wilson, D. L. Quantitative myocardial perfusion imaging in a porcine ischemia model using a prototype spectral detector CT system. *Phys. Med. Biol.*, 61:2407–2431, March 2016. ISSN 1361-6560. doi: 10.1088/0031-9155/61/6/2407.
- Feldkamp, L., Davis, L., and Kress, J. Practical cone-beam algorithm. *Journal of Optical Society of America A*, 1(6):612–619, 1984.
- Felzenszwalb, P. F. and Huttenlocher, D. P. Distance transforms of sampled functions. *Theory of Computing*, 8(19):415–428, 2012. doi: 10.4086/toc.2012.v008a019.

- Flohr, T. G., McCollough, C. H., Bruder, H., Petersilka, M., Gruber, K., Süß, C., Grasruck, M., Stierstorfer, K., Krauss, B., Raupach, R., Primak, A. N., Küttner, A., Achenbach, S., Becker, C., Kopp, A., and Ohnesorge, B. M. First performance evaluation of a dual-source CT (DSCT) system. *European Radiology*, 16(2):256–268, Feb 2006. ISSN 1432-1084. doi: 10.1007/s00330-005-2919-2.
- Gibson, E., Giganti, F., Hu, Y., Bonmati, E., Bandula, S., Gurusamy, K., Davidson, B., Pereira, S. P., Clarkson, M. J., and Barratt, D. C. Automatic multi-organ segmentation on abdominal CT with dense V-networks. *IEEE Transactions on Medical Imaging*, 37:1822–1834, August 2018. ISSN 1558-254X. doi: 10.1109/TMI.2018.2806309.
- Goodsitt, M. M., Rosenthal, D. I., Reinus, W. R., and Coumas, J. Two postprocessing CT techniques for determining the composition of trabecular bone. *Investigative Radiology*, 22:209–215, March 1987. ISSN 0020-9996.
- Graser, A., Johnson, T. R. C., Bader, M., Staehler, M., Haseke, N., Nikolaou, K., Reiser, M. F., Stief, C. G., and Becker, C. R. Dual energy CT characterization of urinary calculi: Initial in vitro and clinical experience. *Investigative Radiology*, 43(2):112 – 119, 2008. ISSN 0020–9996. doi: 10.1097/RLI.0b013e318157a144.
- Grasruck, M., Kappler, S., Reinwand, M., and Stierstorfer, K. Dual energy with dual source CT and kVp switching with single source CT: a comparison of dual energy performance. In *SPIE Medical Imaging 2009: Physics of Medical Imaging*, volume 7258, page 72583R. International Society for Optics and Photonics, 2009.
- Harris, K. M., Adam, H., Lloyd, D. C. F., and Harvey, D. J. The effect on apparent size of simulated pulmonary nodules of using three standard CT window settings. *Clinical Radiology*, 47:241–244, 1993.
- Henzler, T., Fink, C., Schoenberg, S. O., and Schoepf, U. J. Dual-energy CT: radiation dose aspects. *American Journal of Roentgenology*, 199(5_supplement):S16–S25, 2012.
- Hidas, G., Eliahou, R., Duvdevani, M., Coulon, P., Lemaitre, L., Gofrit, O. N., Pode, D., and Sosna, J. Determination of renal stone composition with dual-energy CT: In vivo analysis and comparison with x-ray diffraction. *Radiology*, 257(2):394–401, 2010. doi: 10.1148/radiol.10100249. PMID: 20807846.
- Hofmann, C., Sawall, S., Knaup, M., and Kachelrieß, M. Alpha image reconstruction (AIR): A new iterative CT image reconstruction approach using voxel-wise alpha blending. *Med. Phys.*, 41(6):061914–1–14, 2014.
- Hounsfield, G. N. Computerized transverse axial scanning (tomography). part 1: Description of the system. *The British Journal of Radiology*, 46:1016–1022, December 1973. ISSN 0007-1285. doi: 10.1259/0007-1285-46-552-1016.
- Hounsfield, G. N. Picture quality of computed tomography. *American Journal of Roentgenology*, 127:3–9, July 1976. ISSN 0361-803X. doi: 10.2214/ajr.127.1.3.
- Hounsfield, G. N. Computed medical imaging. *Science (New York, N.Y.)*, 210:22–28, October 1980. ISSN 0036-8075.

- Huesman, R., Gullberg, G., Greenberg, W., and Budinger, T. Users manual: Donner algorithms for reconstruction tomography. *Berkeley Laboratory, University of California*, 1977.
- Hyodo, T., Hori, M., Lamb, P., Sasaki, K., Wakayama, T., Chiba, Y., Mochizuki, T., and Murakami, T. Multimaterial decomposition algorithm for the quantification of liver fat content by using fast-kilovolt-peak switching dual-energy CT: Experimental validation. *Radiology*, 282:381–389, February 2017. ISSN 1527-1315. doi: 10.1148/radiol.2016160129.
- Johnson, T. R. C. Dual-energy CT: General principle. *American Journal of Roentgenology*, 199(5 supplement):S3–S8, 2012. doi: 10.2214/AJR.12.9116.
- Johnson, T. R. C., Krauß, B., Sedlmair, M., Grasruck, M., Bruder, H., Morhard, D., Fink, C., Weckbach, S., Lenhard, M., Schmidt, B., Flohr, T., Reiser, M. F., and Becker, C. R. Material differentiation by dual energy CT: initial experience. *European Radiology*, 17(6):1510–1517, Jun 2007. ISSN 1432-1084. doi: 10.1007/s00330-006-0517-6.
- Kachelrieß, M. *Clinical X-Ray Computed Tomography*, pages 41–80. Springer Berlin Heidelberg, Berlin, Heidelberg, 2006. ISBN 978-3-540-29999-8. doi: 10.1007/3-540-29999-8_7.
- Kachelrieß, M., Schaller, S., and Kalender, W. A. Advanced single-slice rebinning in cone-beam spiral CT. *Med. Phys.*, 27(4):754–772, 2000.
- Kachelrieß, M., Knaup, M., and Kalender, W. A. Extended parallel backprojection for standard three-dimensional and phase-correlated four-dimensional axial and spiral cone-beam CT with arbitrary pitch, arbitrary cone-angle, and 100% dose usage. *Med. Phys.*, 31(6):1623–1641, 2004.
- Kachelrieß, M., Sourbelle, K., and Kalender, W. A. Empirical cupping correction: a first-order raw data precorrection for cone-beam computed tomography. *Med. Phys.*, 33:1269–1274, May 2006. ISSN 0094-2405. doi: 10.1118/1.2188076.
- Kalender, W. A., Klotz, E., and Suess, C. Vertebral bone mineral analysis: an integrated approach with CT. *Radiology*, 164:419–423, August 1987. ISSN 0033-8419. doi: 10.1148/radiology.164.2.3602380.
- Kalender, W. A. *Computertomographie: Grundlagen, Gerätetechnologie, Bildqualität, Anwendungen*. Erlangen; München: Publicis-MCD-Verl., 2000.
- Kappler, S., Glasser, F., Janssen, S., Kraft, E., and Reinwand, M. A research prototype system for quantum-counting clinical CT. In *SPIE Medical Imaging 2010: Physics of Medical Imaging*, volume 7622, page 76221Z. International Society for Optics and Photonics, 2010.
- Kappler, S., Hannemann, T., Kraft, E., Kreisler, B., Niederloehner, D., Stierstorfer, K., and Flohr, T. First results from a hybrid prototype CT scanner for exploring benefits of quantum-counting in clinical CT. In *SPIE Medical Imaging 2012: Physics*

- of Medical Imaging*, volume 8313, page 83130X. International Society for Optics and Photonics, 2012.
- Kappler, S., Henning, A., Krauss, B., Schoeck, F., Stierstorfer, K., Weidinger, T., and Flohr, T. Multi-energy performance of a research prototype CT scanner with small-pixel counting detector. In *SPIE Medical Imaging 2013: Physics of Medical Imaging*, volume 8668, page 86680O. International Society for Optics and Photonics, 2013.
- Kappler, S., Henning, A., Kreisler, B., Schoeck, F., Stierstorfer, K., and Flohr, T. Photon counting CT at elevated x-ray tube currents: contrast stability, image noise and multi-energy performance. In *SPIE Medical Imaging 2014: Physics of Medical Imaging*, volume 9033, page 90331C. International Society for Optics and Photonics, 2014.
- Katsevich, A. A general scheme for constructing inversion algorithms for cone beam CT. *International Journal of Mathematics and Mathematical Science*, 21:1305–1321, 2003.
- Kelcz, F., Joseph, P. M., and Hilal, S. K. Noise considerations in dual energy CT scanning. *Med. Phys.*, 6(5):418–425, 1979.
- Kimpe, T. and Tuytschaever, T. Increasing the number of gray shades in medical display systems—how much is enough? *Journal of Digital Imaging*, 20:422–432, December 2007. ISSN 0897-1889. doi: 10.1007/s10278-006-1052-3.
- Knoll, G. F. *Radiation Detection and Measurement*. New York, NY : Wiley, 2010. - 830 p., 4 edition, 2010. ISBN 9780470131480.
- Krauss, B., Schmidt, B., and Flohr, T. G. Dual source CT. In Johnson, T. R., Fink, C., Schönberg, S., and Reiser, M. F., editors, *Dual Energy CT in Clinical Practice*, pages 11–20. Springer-Verlag Berlin Heidelberg, 2011. doi: 10.1007/978-3-642-01740-7.
- Krauss, B., Grant, K. L., Schmidt, B. T., and Flohr, T. G. The importance of spectral separation: an assessment of dual-energy spectral separation for quantitative ability and dose efficiency. *Investigative Radiology*, 50(2):114–118, 2015.
- Krieger, H. *Grundlagen der Strahlungsphysik und des Strahlungsschutzes*. Vieweg+Teubner Verlag, Springer, 2009.
- Kuchenbecker, S., Faby, S., Simons, D., Knaup, M., Schlemmer, H.-P., and Kachelrieß, M. Segmentation-assisted material decomposition in dual energy computed tomography (DECT). In *101st Scientific Assembly and Annual Meeting of the Radiological Society of North America (RSNA), November 2015*, 2015.
- Lavdas, I., Glocker, B., Kamnitsas, K., Rueckert, D., Mair, H., Sandhu, A., Taylor, S. A., Aboagye, E. O., and Rockall, A. G. Fully automatic, multi-organ segmentation in normal whole body magnetic resonance imaging (MRI), using classification forests (CFs), convolutional neural networks (CNNs) and a multi-atlas (MA) approach. *Med. Phys.*, 2017.

- Lebedev, S., Sawall, S., Knaup, M., and Kachelrieß, M. Optimization of the alpha image reconstruction – an iterative CT-image reconstruction with well-defined image quality metrics. *Zeitschrift für Medizinische Physik*, 27(3), September 2017. doi: 10.1016/j.zemedi.2017.04.004.
- Leng, S., Gutjahr, R., Ferrero, A., Kappler, S., Henning, A., Halaweish, A., Zhou, W., Montoya, J., and McCollough, C. Ultra-high spatial resolution multi-energy CT using photon counting detector technology. In *SPIE Medical Imaging 2017: Physics of Medical Imaging*, volume 978312. International Society for Optics and Photonics, 2017.
- Li, B. Dual-energy CT with fast-kVp switching and its applications in orthopedics. *OMICS Journal of Radiology*, 2(6):137–143, 2013. doi: 10.4172/2167-7964.1000137.
- Lifeng, Y., Zhoubo, L. S., Li, and McCollough, C. H. Dual-source multi-energy CT with triplet or quadruple x-ray beams. In *SPIE Medical Imaging 2016: Physics of Medical Imaging*, volume 10132, pages 9783 – 9783 – 6. International Society for Optics and Photonics, 2016. doi: 10.1117/12.2217446.
- Liu, X., Yu, L., Primak, A. N., and McCollough, C. H. Quantitative imaging of element composition and mass fraction using dual-energy CT: Three-material decomposition. *Med. Phys.*, 36(5):1602–1609, 2009. ISSN 2473-4209. doi: 10.1118/1.3097632.
- Long, J., Shelhamer, E., and Darrell, T. Fully convolutional networks for semantic segmentation. In *Proceedings of the IEEE Conference of Computer Vision and Pattern Recognition*, pages 3431–3440, 2015.
- Long, Y. and Fessler, A., Jeffrey. Multi-material decomposition using statistical image reconstruction for spectral CT. *IEEE Transactions on Medical Imaging*, 33(8):1614–1626, 2014.
- Maaß, C., Baer, M., and Kachelrieß, M. Image-based dual energy CT using optimized precorrection functions: a practical new approach of material decomposition in image domain. *Med. Phys.*, 36:3818–3829, August 2009. ISSN 0094-2405. doi: 10.1118/1.3157235.
- Maaß, C., Meyer, E., and Kachelrieß, M. Exact dual energy material decomposition from inconsistent rays (MDIR). *Med. Phys.*, 38:691–700, February 2011a. ISSN 0094-2405. doi: 10.1118/1.3533686.
- Maaß, N., Sawall, S., Knaup, M., and Kachelrieß, M. Dose minimization for material-selective CT with energy-selective detectors. In *Nuclear Science Symposium and Medical Imaging Conference (NSS/MIC), 2011 IEEE*, pages 4447–4452. IEEE, 2011b.
- Mandell, J. C., Wortman, J. R., Rocha, T. C., Folio, L. R., Andriole, K. P., and Khurana, B. Computed tomography window blending: Feasibility in thoracic trauma. *Academic Radiology*, 25:1190–1200, September 2018. ISSN 1878-4046. doi: 10.1016/j.acra.2017.12.029.

- Manger, B., Lell, M., Wacker, J., Schett, G., and Rech, J. Detection of periarticular urate deposits with dual energy CT in patients with acute gouty arthritis. *Annals of the Rheumatic Diseases*, 71(3):470–472, 2012. ISSN 0003-4967. doi: 10.1136/ard.2011.154054.
- McCollough, C., Leng, S., Yu, L., and Fletcher, J. G. Dual- and multi-energy CT: Principles, technical approaches, and clinical applications. *Radiology*, 276(3):637–653, 2015.
- Mendonça, P. R. S., Lamb, P., and Sahani, D. V. A flexible method for multi-material decomposition of dual-energy CT images. *IEEE Transactions on Medical Imaging*, 33(1):99–116, 2014.
- Millner, M. R., McDavid, W. D., Waggener, R. G., Dennis, M. J., Payne, W. H., and Sank, V. J. Extraction of information from CT scans at different energies. *Med. Phys.*, 6:70–71, 1979. ISSN 0094-2405. doi: 10.1118/1.594555.
- Napel, S., Rubin, G. D., and Jeffrey, R. B. J. STS-MIP: A new reconstruction technique for CT of the chest. *Journal of Computer Assisted Tomography*, 17(5):832–838, 1993.
- Nicolaou, S., Yong-Hing, C. J., Galea-Soler, S., Hou, D. J., Louis, L., and Munk, P. Dual energy CT as a potential new diagnostic tool in the management of gout in the acute setting. *American Journal of Roentgenology*, 194(4):1072 – 1078, April 2010.
- O’Donnell, T. P., Cormode, D. P., Halaweish, A., Cheheltani, R., Fayad, Z., and Mani, V. Material decomposition in an arbitrary number of dimensions using noise compensating projection. *Biomedical Physics and Engineering Express*, 2017. doi: 10.1088/2057-1976/aa907d.
- Okada, T., Yokota, K., Hori, M., Nakamoto, M., Nakamura, H., and Sato, Y. Construction of hierarchical multi-organ statistical atlases and their application to multi-organ segmentation from CT images. In Metaxas, D., Axel, L., Fichtinger, G., and Székely, G., editors, *Medical Image Computing and Computer-Assisted Intervention – MIC-CAI 2008: 11th International Conference, New York, NY, USA, September 6-10, 2008, Proceedings, Part I*, pages 502–509, Berlin, Heidelberg, 2008. Springer Berlin Heidelberg. ISBN 978-3-540-85988-8. doi: 10.1007/978-3-540-85988-8_60.
- Pache, G., Krauss, B., Strohm, P., Saueressig, U., Blanke, P., Bulla, S., Schäfer, O., Helwig, P., Kotter, E., Langer, M., and Baumann, T. Dual-energy CT virtual noncalcium technique: Detecting posttraumatic bone marrow lesions feasibility study. *Radiology*, 256(2):617–624, 2010. doi: 10.1148/radiol.10091230. PMID: 20551186.
- Park, H., Bland, P. H., and Meyer, C. R. Construction of an abdominal probabilistic atlas and its application in segmentation. *IEEE Transactions on Medical Imaging*, 22(4):483–492, 2004.
- Polster, C., Gutjahr, R., Schöck, F., Kappler, S., Dietrich, O., and Flohr, T. Improving material decomposition by spectral optimization of photon counting computed tomography. In *SPIE Medical Imaging 2016: Physics of Medical Imaging*, volume 978310. International Society for Optics and Photonics, 2016.

- Pomerantz, S. M., White, C. S., Krebs, T. L., Daly, B., Sukumar, S. A., Hooper, F., and Siegel, E. L. Liver and bone window settings for soft-copy interpretation of chest and abdominal CT. *American Journal of Radiology*, 174(2):311–314, 2000.
- Pompe, E., Willemink, M. J., Dijkhuis, G. R., Verhaar, H. J. J., Mohamed Hoesin, F. A. A., and de Jong, P. A. Intravenous contrast injection significantly affects bone mineral density measured on CT. *European Radiology*, 25:283–289, February 2015. ISSN 1432-1084. doi: 10.1007/s00330-014-3408-2.
- Primak, A., Ramirez Giraldo, J., Liu, X., Yu, L., and McCollough, C. Improved dual-energy material discrimination for dual-source CT by means of additional spectral filtration. *Med. Phys.*, 36(4):1359–1369, 2009.
- Primak, A. N., Giraldo, J. C. R., Eusemann, C. D., Schmidt, B., Kantor, B., Fletcher, J. G., and McCollough, C. H. Dual-source dual-energy CT with additional tin filtration: Dose and image quality evaluation in phantoms and in vivo. *American Journal of Roentgenology*, 195:1164–1174, November 2010. ISSN 1546-3141. doi: 10.2214/AJR.09.3956.
- Radon, J. On the determination of functions from their integrals along certain manifolds. *Ber. Verh. Sachs Akad Wiss.*, 69:262–277, 1917.
- Ramachandran, G. and Lakshminarayanan, A. Three-dimensional reconstruction from radiographs and electron micrographs: application of convolutions instead of fourier transforms. *Proceedings of the National Academy of Sciences*, 68(9):2236–2240, 1971.
- Rodet, T., Noo, F., and Defrise, M. The cone-beam algorithm of feldkamp, davis, and kress preserves oblique line integrals. *Med. Phys.*, 31(7):1972–1975, 2004.
- Ronneberger, O., Fischer, P., and Brox, T. U-Net: Convolutional networks for biomedical image segmentation. In Ourselin, S., Joskowicz, L., Sabuncu, M. R., Unal, G., and Wells, W., editors, *Medical Image Computing and Computer-Assisted Intervention – MICCAI 2015*, volume abs/1505.04597 of *LNCS*, pages 234–241. Springer International Publishing, 2015. available on arXiv:1505.04597 [cs.CV].
- Röntgen, W. C. Über eine neue Art von Strahlen. Würzburg, Sitzgs. *Ber. Physik.-Med. Ges*, 132, 1895.
- Roth, H. R., Oda, H., Hayashi, Y., Oda, M., Shimizu, N., Fujiwara, M., Misawa, K., and Mori, K. Hierarchical 3D fully convolutional networks for multi-organ segmentation. In *CoRR*, volume abs/1704.06382, 2017. available on arXiv:1704.06382 [cs.CV].
- Schaller, S., Stierstorfer, K., Bruder, H., Kachelrieß, M., and Flohr, T. Novel approximate approach for high-quality image reconstruction in helical cone-beam CT at arbitrary pitch. In *SPIE Medical Imaging 2001: Image Processing*, volume 4322, pages 113–128. International Society for Optics and Photonics, 2001.
- Scheegerer, A. A., Nagel, H.-D., Stamm, G., Adam, G., and Brix, G. Current CT practice in Germany: Results and implications of a nationwide survey. *European Journal of Radiology*, 90:114–128, May 2017. ISSN 1872-7727. doi: 10.1016/j.ejrad.2017.02.021.

- Shepp, L. A. and Logan, B. F. The Fourier reconstruction of a head section. *IEEE Transactions on Nuclear Science*, 21(3):21–43, 1974.
- Slavic, S., Madhav, P., Profio, M., Crotty, D., Nett, E., Hsieh, J., and Liu, E. GSI Xtream on Revolution™ CT. Technology White Paper, 2017. GE Healthcare.
- Stierstorfer, K., Flohr, T., and Bruder, H. Segmented multiple plane reconstruction: a novel approximate reconstruction scheme for multi-slice spiral CT. *Phys. Med. Biol.*, 47(15):2571, 2002.
- Stierstorfer, K., Rauscher, A., Boese, J., Bruder, H., Schaller, S., and Flohr, T. Weighted FBP – a simple approximate 3D FBP algorithm for multislice spiral CT with good dose usage for arbitrary pitch. *Phys. Med. Biol.*, 49(11):2209–2218, 2004. doi: 10.1088/0031-9155/49/11/007.
- Stolzmann, P., Leschka, S., Scheffel, H., Rentsch, K., Baumüller, S., Desbiolles, L., Schmidt, B., Marincek, B., and Alkadhi, H. Characterization of urinary stones with dual-energy CT: Improved differentiation using a tin filter. *Investigative Radiology*, 45(1):1–6, 2010.
- Sutton, D., Reznick, R., and Murfitt, J. *Textbook of Radiology and Imaging*. Elsevier Health Science, 7 edition, 2002.
- Tang, M., Zhang, Z. V., Cobzas, D., Jägersand, M., and Jaremko, J. L. Segmentation-by-detection: A cascade network for volumetric medical image segmentation. *2018 IEEE 15th International Symposium on Biomedical Imaging (ISBI 2018)*, pages 1356–1359, 2018.
- Thieme, S. F., Johnson, T. R. C., Lee, J., Christopher McWilliams, Becker, C. R., Reiser, M. F., and Nikolaou, K. Dual-energy CT for the assessment of contrast material distribution in the pulmonary parenchyma. *American Journal of Roentgenology*, 193: 144–149, 2009.
- Tong, N., Gou, S., Yang, S., Ruan, D., and Sheng, K. Fully automatic multi-organ segmentation for head and neck cancer radiotherapy using shape representation model constrained fully convolutional neural networks. *Med. Phys.*, 45:4558–4567, October 2018. ISSN 2473-4209. doi: 10.1002/mp.13147.
- Vetter, J. R., Perman, W. H., Kalender, W. A., Mazess, R. B., and Holden, J. E. Evaluation of a prototype dual-energy computed tomographic apparatus. II. Determination of vertebral bone mineral content. *Med. Phys.*, 13:340–343, 1986. ISSN 0094-2405. doi: 10.1118/1.595951.
- Vlassenbroek, A. Dual layer CT. In Johnson, T. R., Fink, C., Schönberg, S., and Reiser, M. F., editors, *Dual Energy CT in Clinical Practice*, pages 21–34. Springer-Verlag Berlin Heidelberg, 2011.
- Vlassenbroek, A., Vembar, M., and Grass, M. *Innovations in Cardiac CTA*, pages 5–30. Springer International Publishing, Cham, 2018. ISBN 978-3-319-66988-5. doi: 10.1007/978-3-319-66988-5_2.

- von Falck, C., Galanski, M., and Shin, H.-O. Informatics in radiology: sliding–thin–slab averaging for improved depiction of low–contrast lesions with radiation dose savings at thin–section CT. *Radiographics*, 30:317–326, March 2010. ISSN 1527-1323. doi: 10.1148/rg.302096007.
- Wolz, R., Chu, C., Misawa, K., Fujiwara, M., Mori, K., and Rueckert, D. Automated abdominal multi–organ segmentation with subject–specific atlas generation. *IEEE Transactions on Medical Imaging*, 32(9):1723–1730, 2013.
- Xue, Y., Ruan, R., Hu, X., Kuang, Y., Wang, J., Long, Y., and Niu, T. Statistical image–domain multimaterial decomposition for dual–energy CT. *Med. Phys.*, 44(3): 886–901, 2017.
- Yu, L., Liu, X., and McCollough, C. H. Pre–reconstruction three–material decomposition in dual–energy CT. In *SPIE Medical Imaging 2009: Physics of Medical Imaging*, volume 7258, pages 7258 – 7258 – 8, 2009. doi: 10.1117/12.813686.
- Yu, L., Leng, S., and McCollough, C. H. Dual–source multi–energy CT with triple or quadruple x–ray beams. *Proceedings of SPIE–the International Society for Optical Engineering*, 9783, February 2016. ISSN 0277-786X. doi: 10.1117/12.2217446.
- Yu, L., Ren, L., Li, Z., Leng, S., and McCollough, C. H. Dual–source multienergy CT with triple or quadruple x–ray beams. *Journal of Medical Imaging*, 5(3):033502, 2018.
- Zhang, D., Li, X., and Liu, B. Objective characterization of GE discovery CT750 HD scanner: Gemstone spectral imaging mode. *Med. Phys.*, 38(3):1178–1188, 2011.

APPENDIX A

Additional Results

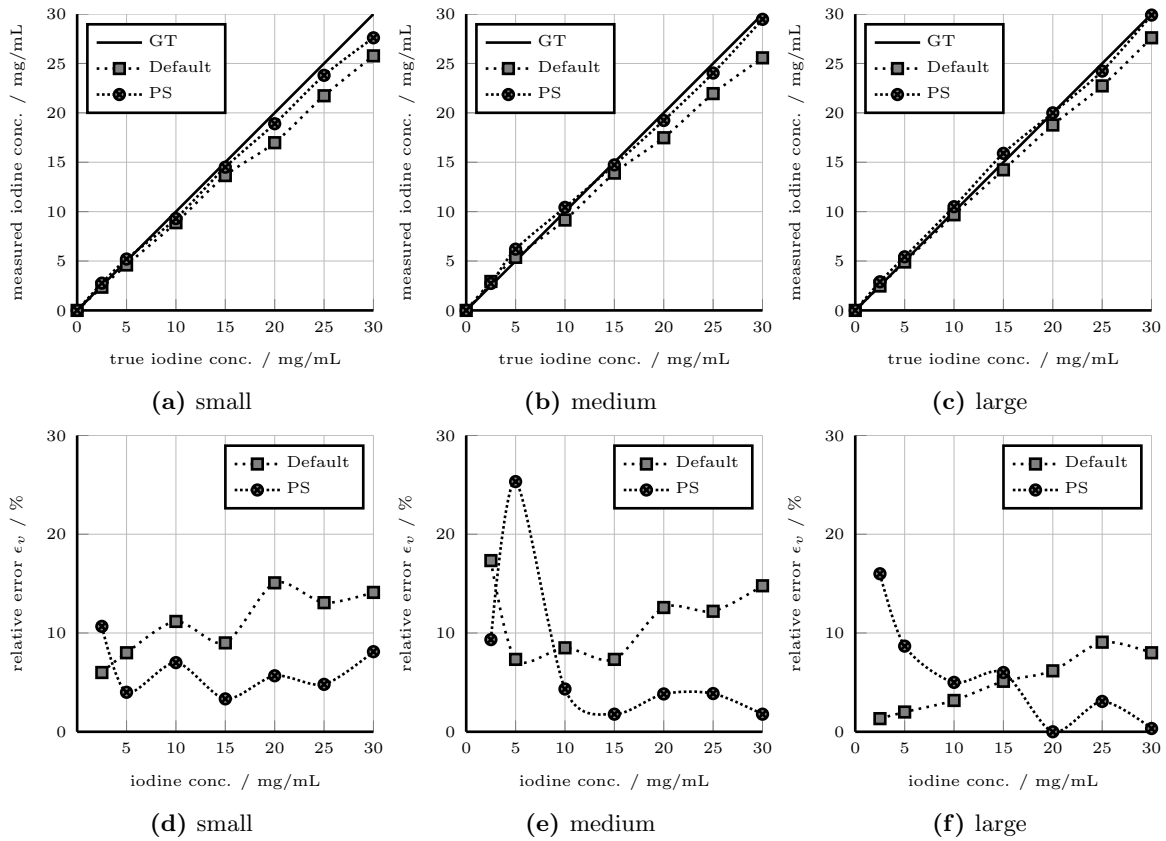


Figure A.1: Liver phantom 100/140 kV+Sn. Figure A.1a–A.1c show the measured iodine concentration $c_{\text{measured},v}$ and the true iodine concentration $c_{\text{GT},v}$ obtained using default and patient-specific (PS) calibration. Figure A.1d–A.1f show the corresponding relative errors ϵ_v of the obtained iodine concentrations using default parameters and patient-specific calibrations. The calibration ROIs are evaluated in the lowest and in the highest iodine concentration, respectively.

Figure A.1 and Figure A.2 depict the measured versus the true iodine concentrations for the default calibration as well as for patient-specific calibrations and the corresponding relative error for all three phantom sizes for the tube voltage combination of 100/140 kV+Sn.

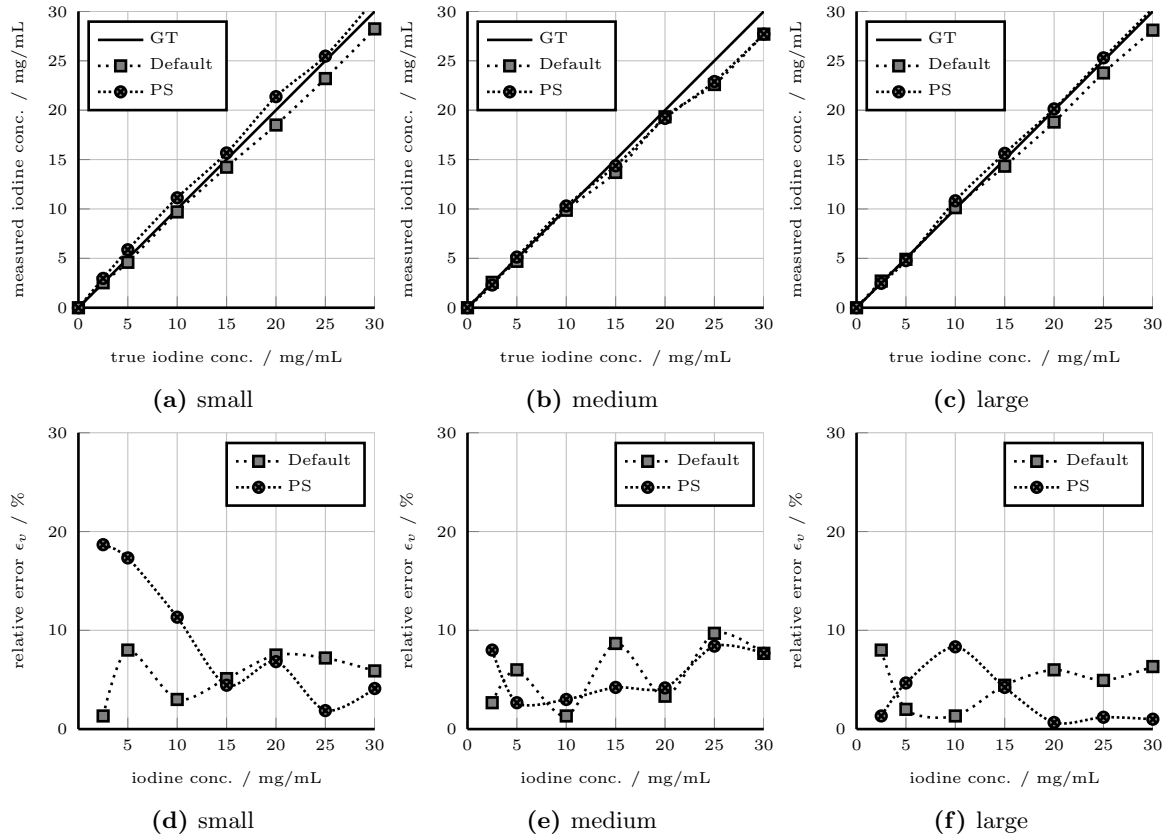


Figure A.2: Thorax phantom 100/140 kV+Sn. Figure A.2a–A.2c show the measured iodine concentration $c_{\text{measured},v}$ and the true iodine concentration $c_{\text{GT},v}$ obtained using default and patient-specific (PS) calibration. Figure A.2d–A.2f show the corresponding relative errors ϵ_v of the obtained iodine concentrations using default parameters and patient-specific calibrations. The calibration ROIs are evaluated in the lowest and in the highest iodine concentration, respectively.

APPENDIX B

Publications

Parts of this thesis have been published in the following journal article and conference contributions:

Journal Articles

Dorn, S., Chen, S., Sawall, S., Maier, J., Knaup, M., Uhrig, M., Schlemmer, H.-P., Maier, A., Lell, M., Kachelrieß, M. Towards context-sensitive CT imaging — Organ-specific image formation for single (SECT) and dual energy computed tomography (DECT). *Med. Phys.*, 45(10), 4541–4557.

Chen, S., Zhong, X., Hu, S., **Dorn, S.**, Kachelrieß, M., Lell, M., Maier, A. Automatic multi-organ segmentation in dual energy CT (DECT) with dedicated 3D fully convolutional DECT networks. *Med. Phys.*, (submitted, currently under review)

Grob, D., Oostveen, L., Rühaak, J., Heldmann, S., Mohr, B., Michielsen, K., **Dorn, S.**, Kachelrieß, M., Prokop, M., Brink, M., Sechopoulos, I. Accuracy of registration algorithms in subtraction CT of the lungs: a digital phantom study. *Med. Phys.*, (submitted, currently under review)

Conference Contributions

Dorn, S., Chen, S., Pisana, F., Maier, J., Knaup, M., Sawall, S., Maier, A., Lell, M., Kachelrieß, M. Organ-specific context-sensitive single and dual energy CT (DECT) image reconstruction, display and analysis. *103rd Scientific Assembly and Annual Meeting of the Radiological Society of North America*, 2017.

Dorn, S., Chen, S., Sawall, S., Simons, D., May, M., Maier, J., Knaup, M., Schlemmer, H.-P., Maier, A., Lell, M., Kachelrieß, M. Organ-specific context-sensitive CT image reconstruction and display. *Proceedings of the SPIE Medical Imaging Conference 2018, 10573*, 1057326, February 2018, doi: 10.1117/12.2291897.

- Dorn, S.**, Chen, S., Pisana, F., Özdemir, M., Maier, J., Sawall, S., Knaup, M., Maier, A., Lell, M., Kachelrieß, M. Context-sensitive organ-specific evaluation and analysis of dual energy computed tomography (DECT). *Proceedings of the 2018 European Congress of Radiology (ECR)*, 28.02.-04.03.2018.
- Dorn, S.**, Chen, S., Sawall, S., Maier, J., Knaup, M., Maier, A., Lell, M., Kachelrieß, M. Prior-based multi material decomposition (PBMMD) for dual energy CT. *Proceedings of the Fifth International Conference on Image Formation in X-Ray Computed Tomography*, 106–109, May 2018.
- Dorn, S.**, Sawall, S., Maier, J., Kachelrieß, M. Iodine quantification accuracy in dual source dual energy CT using default parameters and patient-specific calibrations. *Proceedings of the 2019 European Congress of Radiology (ECR)*, 27.02.-03.03.2019.
- Dorn, S.**, Sawall, S., Maier, J., Polster, C., Faby, S., Uhrig, M., Schlemmer, H.-P., Kachelrieß, M. Patient size-dependent ultra low dose data completion scan in a whole body photon-counting CT prototype. *Proceedings of the 2019 European Congress of Radiology (ECR)*, 27.02.-03.03.2019.
- Chen, S., Endreß, J., **Dorn, S.**, Maier, J., Lell, M., Kachelrieß, M., Maier, A. A feasibility study of automatic multi-organ segmentation using probabilistic atlas. *Bildverarbeitung für die Medizin: Algorithmen-Systeme-Anwendungen*, Heidelberg, 2017, 218–223.
- Chen, S., **Dorn, S.**, Lell, M., Kachelrieß, M., Maier, A. Manifold learning-based data sampling for model training. *Bildverarbeitung für die Medizin: Algorithmen-Systeme-Anwendungen*, Erlangen, 2018, 269–274.
- Chen, S., Roth, H., **Dorn, S.**, May, M., Cavallaro, A., Lell, M., Kachelrieß, M., Oda, H., Mori, K., Maier, A. Towards automatic abdominal multi-organ segmentation in dual energy CT using cascaded 3D fully convolutional network. *Proceedings of the Fifth International Conference on Image Formation in X-Ray Computed Tomography*, 395–398, May 2018.
- Chen, S., Zhong, X., Hu, S., **Dorn, S.**, Kachelrieß, M., Lell, M., Maier, M. Automatic multi-organ segmentation in dual energy CT using 3D fully convolutional network. *International Conference on Medical Imaging with Deep Learning (MIDL)*, Amsterdam 2018.
- Maier, J., Eulig, E., **Dorn, S.**, Sawall, S., Kachelrieß, M. Real-time patient-specific CT dose estimation using a deep convolutional neural network. *2018 IEEE Nuclear Science Symposium and Medical Imaging Conference Nuclear Science Symposium Conference Record (NSS/MIC)*, October/November 2018.
- Özdemir, M., **Dorn, S.**, Pisana, F., Schlemmer, H.-P., Kachelrieß, M. Image-based noise reduction for material decomposition in dual and multi energy computed tomography. *Proceedings of the SPIE Medical Imaging Conference 2019*, February 2019.
- Sawall, S., **Dorn, S.**, Maier, J., Faby, S., Uhrig, M., Schlemmer, H.-P., Kachelrieß, M. Optimal iodine CNR in a whole body photon-counting CT scanner. *Proceedings of the 2019 European Congress of Radiology (ECR)*, 27.02.-03.03.2019.

-
- Sawall, S., **Dorn, S.**, Maier, J., Faby, S., Uhrig, M., Schlemmer, H.-P., Kachelrieß, M.
Does iodine CNR improve when switching from today's energy integrating CT to tomorrow's photon-counting CT? *Proceedings of the 2019 European Congress of Radiology (ECR)*, 27.02.-03.03.2019
- Maier, J., Eulig, E., **Dorn, S.**, Sawall, S., Kachelrieß, M. Real-time patient-specific CT dose estimation for single- and dual-source CT using deep convolutional neural network. *Proceedings of the 2019 European Congress of Radiology (ECR)*, 27.02.-03.03.2019.
- Uhrig, M., Delorme, S., Bickelhaupt, S., Faby, S., **Dorn, S.**, Kachelrieß, M., Schlemmer, H.-P., Sawall, S. Hochauflösende Darstellung von Knochenläsionen und Trabekelstruktur mit einem photonenzählenden Ganzkörper-CT. *RöKo 2019*
- Sawall, S., **Dorn, S.**, Maier, J., Klein, L., Faby, S., Uhrig, M., Schlemmer, H.-P. Patienten-adaptierte Schwellwertstellungen für optimalen Iodkontrast in einem photonenzählenden Ganzkörper-CT. *RöKo 2019*

APPENDIX C

Curriculum Vitae

Personal Information

NAME: Sabrina Dorn
DATE OF BIRTH: November 9th, 1987
PLACE OF BIRTH: Nürnberg, Germany
NATIONALITY: German

School

SEP 1994–AUG 2000	Grundschule im Knoblauchsland, Nürnberg
SEP 2000–AUG 2005	Veit-Stoß Realschule, Nürnberg
SEP 2005–JUL 2009	Peter-Vischer-Schule, Gymnasium, Nürnberg
JUL 2009	University-Entrance Qualification (German „Abitur“)

University

OCT 2009–JUL 2013	Bachelor of Science (B. Sc.) in MEDICAL ENGINEERING Friedrich–Alexander–University Erlangen–Nürnberg , Erlangen Thesis title: “Energy Expenditure Estimation for Multiple Sclerosis Patients from Inertial Sensor Data”
JUL 2013–NOV 2015	Master of Science (M. Sc.) in MEDICAL ENGINEERING Friedrich–Alexander–University Erlangen–Nürnberg , Erlangen Thesis title: “Automatic Kidney Volume Estimation from MRI Data”
AS OF JAN 2016	PhD Candidate, German Cancer Research Center (DKFZ) , Devision of X–ray Imaging and CT, Heidelberg and Ruprecht–Karls–University Heidelberg , Heidelberg Thesis title: “Context–Sensitive Imaging for Single, Dual and Multi Energy Computed Tomography”

APPENDIX D

Acknowledgements

An dieser Stelle möchte ich mich herzlich bei allen bedanken, die zum erfolgreichen Gelingen meiner Doktorarbeit beigetragen haben:

Prof. Dr. Marc Kachelrieß für die Überlassung des Themas und für die ausgezeichneten Möglichkeiten, es zu bearbeiten. Vielen Dank für die Übernahme des Erstgutachtens und die wissenschaftliche Betreuung der vorliegenden Arbeit. Vielen Dank Marc für die herzliche Aufnahme in die Arbeitsgruppe, die vielen Einblicke in dieses interessante Themengebiet und die zahlreichen Denkanstöße!

Prof. Dr. Michael Lell, Prof. Dr. Andreas Maier und Shuqing Chen für die erfolgreiche Zusammenarbeit während des DFG Projekts „Quantitative DECT mit Atlasvorwissen“, für die Bereitstellung der DECT-Daten und der Segmentierung. Herzlichen Dank auch für die zahlreichen hilfreichen Diskussionen.

Weiterhin gilt mein Dank auch der Deutschen Forschungsgemeinschaft, die durch ihre finanzielle Förderung des Forschungsprojekts, die Arbeit erst ermöglicht hat.

Dr. David Simons und Dr. Monika Uhrig danke ich für die Betreuung im Rahmen der Graduiertenschule sowie die medizinische Expertise bei klinischen Fragestellungen. Außerdem danke ich auch Martina für die großzügige und hilfsbereite Bereitstellung der Daten am DKFZ.

Ganz besonderer Dank gilt allen Mitarbeitern und ehemaligen Mitarbeitern der Arbeitsgruppe „Röntgenbildgebung und Computertomographie“ für die kollegiale Hilfsbereitschaft und stets angenehme und freundschaftliche Arbeitsatmosphäre. Insbesondere vielen Dank an das große Büro N110 in allen Konstellationen mit Stefan, Nadine, Carsten, Markus, Philip und Elias und an das neue REZ-Büro mit Stefan, Jan und Joscha. Danke für die großartige Zusammenarbeit, den guten Kaffee und Tee und die unterhaltsamen und lustigen Gespräche zwischendurch.

Zu guter Letzt möchte ich mich bei meiner Familie, insbesondere meinen Eltern und Matthias, bedanken. Danke für die bedingungslose Unterstützung und Rückendeckung während der gesamten Promotionszeit in jeglicher Hinsicht.

Eidesstattliche Erklärung

1. Bei der eingereichten Dissertation zu dem Thema “ Context–Sensitive Imaging for Single, Dual and Multi Energy Computed Tomography ” handelt es sich um meine eigenständig erbrachte Leistung.
2. Ich habe nur die angegebenen Quellen und Hilfsmittel benutzt und mich keiner unzulässigen Hilfe Dritter bedient. Insbesondere habe ich wörtlich oder sinngemäß aus anderen Werken übernommene Inhalte als solche kenntlich gemacht.
3. Die Arbeit oder Teile davon habe ich bislang nicht an einer Hochschule des In- oder Auslands als Bestandteil einer Prüfungs- oder Qualifikationsleistung vorgelegt.
4. Die Richtigkeit der vorstehenden Erklärung bestätige ich.
5. Die Bedeutung der eidesstattlichen Versicherung und die strafrechtlichen Folgen einer unrichtigen oder unvollständigen eidesstattlichen Versicherung sind mir bekannt. Ich versichere an Eides statt, dass ich nach bestem Wissen die reine Wahrheit erklärt und nichts verschwiegen habe.

Heidelberg, October 18, 2019

(Sabrina Dorn)